Technische Universität München
Physik-Department
Lehrstuhl für Biophysik E22

Novel Ultrathin Polymer Films as Biomimetic Interfaces

Florian Rehfeldt

Vollständiger Abdruck der von der Fakultät für Physik
der Technischen Universität München zur Erlangung des akademischen Grades eines
Doktors der Naturwissenschaften (Dr. rer. nat.)
genehmigten Dissertation.

Vorsitzender:		Univ.-Prof. Dr. H. Friedrich
Prüfer der Dissertation:	1.	Univ.-Prof. Dr. E. Sackmann, em.
	2.	Univ.-Prof. Dr. J. O. Rädler, Ludwig-Maximilians-Universität München

Die Dissertation wurde am 1.12.2004 bei der Technischen Universität München eingereicht
und durch die Fakultät für Physik am 17.12.2004 angenommen.

Meinen Eltern

Bernhild und Dr. Klaus Rehfeldt

und meiner Oma

Berta Zimprich

Table of Contents

Summary

The general aim of this study was the design of ultrathin polymer coatings (with thicknesses ranging from several nanometers to hundreds of nanometers) which can serve as interfaces between solid surfaces (e.g. silicon) and living matter and allow the control of the interfacial forces between these two different states of matter. The fabrication of such biocompatible interlayers is a key step towards the control of cell proliferation and immobilization of cells or proteins in their native state onto planar substrates which are fundamental problems in tissue engineering.

In this study, a new type of diblock copolymer (DMAEMA-*b*-MMA) was chosen as the "tunable" polymer interlayer. It consists of a hydrophobic MMA block and a weakly cationic DMAEMA block, whose degree of ionization can be adjusted in a subtle way by pH titration ($pK_a = 7.3$). With a sufficiently high hydrophobic fraction (50 % MMA, DB 50), DB 50 forms an insoluble monolayer at the air/water interface. This monolayer can be transferred onto a hydrophobic substrate with the Langmuir-Schaefer technique, which allows the precise control of the lateral polymer density.

In Chapter 4, the chemical switching of the chain conformation of DB 50 was studied at the air/water interface. The Langmuir isotherms measured at different pH conditions indicated that the adsorption and desorption of the DMAEMA chains to the interface can be manipulated by charging and de-charging. Careful optimization of the preparation protocols based on contact angle measurements, ellipsometry, and x-ray reflectivity resulted in reproducible, stable, and homogeneous films of DB 50 on hydrophobized substrates.

Consequently, in Chapter 5, the chemical switching of these DB 50 films at the solid/liquid interface could be studied quantitatively by neutron reflectivity measurements in D_2O. The global shape of the reflectivity curves exhibited a distinct difference between pH = 8.5 and 5.5, indicating a clear change in thickness, scattering length density (corresponding to the degree of hydration), and roughness of the DB 50 layer. The reflectivity data were perfectly reproducible after several pH cycles, which

verified the stability and reversibility of chemical switching.

To study the interaction between DB 50 films and biofunctional molecules, two series of experiments were performed which are described in Chapter 5.2 and 5.3: one series addressed the problem of nonspecific physisorption of water soluble proteins (bovine serum albumin, BSA), while the second dealt with the spreading of model cell membranes. Although the difference in protein adsorption between pH = 8.5 and 5.5 could hardly be distinguished, for the first time a clear switching of the separation distance between a model cell membrane and the DB 50 film was observed.

The results demonstrate that the system established in this study has great potential as a soft, compatible interlayer between hard solids and soft biological material. It is expected that the fine-tuning of generic interactions between cell membrane models and planar substrates opens new possibilities for scientific and practical applications. The new type of biomimetic interface established in this work provides an ideal platform for future studies of proteins in their native state, which is an important issue in the field of biosensors.

Introduction

The understanding of physical interactions at biological interfaces is a challenging task for interdisciplinary scientific research. In nature, interactions between cells and tissues are mediated by complex interplays of short-range and long-range forces (e.g. van der Waals (dispersion) forces, electrostatic forces, steric (entropic) forces, and hydration forces [1, 2]) across hydrated layers of biopolymers, such as the extracellular matrix (ECM)[3] and the glycocalix [4]. They are necessary to keep a certain distance between neighboring cells as well as to create hydrating pathways for material transport. However, if one considers even a "single" plasma membrane that consists of peripheral and integral proteins, cell surface glycocalix, and cytoskeleton (see Figure 1), the molecular constructs therein are already too complex to be directly reconstituted into one model. Therefore, the design of biomimetic molecular assemblies with a reduced number of components is necessary to create simple physical models. Here, deposition of artificial extracellular matrix and model cell membranes onto planar substrates is a straightforward and powerful strategy to apply various surface sensitive techniques for the quantitative study of their structures and functions.

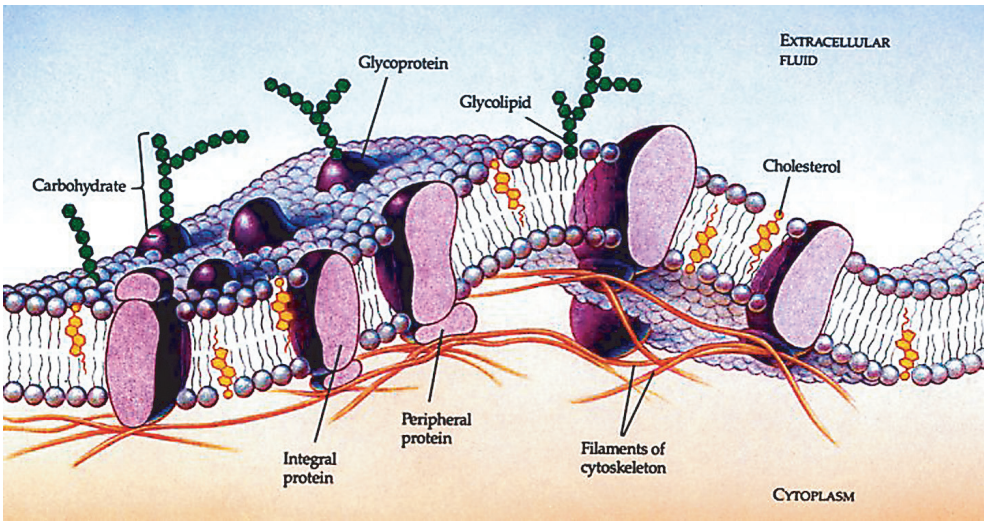

Figure 1: Schematic illustration of the plasma membrane of a cell.

For this purpose (i.e. deposition of biopolymers and cell models), it is necessary to design compatible interlayers between hard solid matter and soft biological matter

[5, 6, 7]. Scientifically, the models of cell and tissue surfaces with reduced number of components enables the study of fundamental principles of cell and tissue contacts by applying rather simple physical principles. For example, a recent study of Bruinsma and Sackmann [8] further extended the theoretical concept of cell adhesion by Bell, Dembo, and Bongrand [9], which explains a double-well potential with a shallow minimum from "weak adhesion" and a sharp minimum inside the repeller in terms of first order wetting/dewetting transition.

The interface matching between solids and biological matter enables the fabrication of novel biofunctional hybrid materials by means of stress-free immobilization of proteins and proliferation of cells onto solid-based devices. For example, the study of trans-membrane protein functions on planar solid substrates (glass, semiconductors, and metals) [10, 11, 12, 13] often requires biopolymer interlayers to avoid the direct protein-substrate contact, which often results in denaturing of proteins. To date, several different strategies have been proposed for the design of ECM and glycocalix models. A straightforward strategy is the direct use of natural ECMs like laminin, fibronectin, and hyaluronan [11, 3]. Although many studies demonstrate that they can bridge cells and solid substrates without denaturing of proteins or cell death (apoptosis), the physical properties of these natural macromolecules are not well defined.

Another promising approach is the surface coating with hygroscopic polymer films or hydro gels, such as dextran [14] and poly (ethylene glycol) (PEG) brushes [15]. Owing to steric (entropic) forces, such films could achieve a sufficient resistance against non-specific adsorption of proteins, which have been used in numerous fields. Such entropic repeller molecules are known to induce large fluctuations to destabilize the cell-surface contact, so that cells and lipid membranes are repelled from the surface [16].

More recently, many studies have been conducted to utilize multilayers of strong polyelectrolyte films as polymer interlayers [17, 18]. Although this type of films can easily be grown by alternative deposition of cationic and anionic polymer films, they have fundamental drawbacks. Most of these polyelectrolyte complexes are based on strong polyelectrolytes, which carry extremely high charge densities at wide pH ranges. Such highly charged surfaces often attract cells and proteins too strongly when they are oppositely charged. In fact, it was previously found that adult mammal cell membranes (from human erythrocytes) secreted by negatively charged sialic acid residues were dissipated on the surface of a commonly used polycation (poly-L-lysine), which can be understood as de-wetting of cell membranes [19]. As an alternative material, regenerated thin films of cellulose have been reported as excellent interlayers to accommodate artificial and native cell membranes without notable defects [12, 19, 20, 21]. These films can be prepared either by spin-coating or by layer-by-layer deposition of synthetically modified cellulose, followed by chemical regeneration to the

original cellulose [22]. Both methods enable the control of the film thickness within nm accuracy, while keeping very small topographic roughness (typical r.m.s. roughness of 5 Å independent from total thickness or preparation methods). Using ellipsometry coupled to a climate chamber, the equilibrium swelling behavior of polysaccharide films has been studied under well defined osmotic pressure conditions (see Appendix A.2) [22]. Indeed, cellulose films with a thickness of 5 – 20 nm can be used as a platform to spread both artificial and native cell membranes (see Appendix A.3) [21].

The next challenging task towards a more sophisticated design of biocompatible interfaces would be to switch the interplays of forces in polymer layers by external stimuli. As chemically switchable polymer material, a monolayer of a diblock copolymer (poly 2-(dimethylamino)ethyl methacrylate -block- methyl methacrylate, DMAEMA-*b*-MMA) with equal number of monomers ($n = 36$) for hydrophobic and hydrophilic blocks (DB 50) was chosen. The hydrophilic DMAEMA moieties are weak polyelectrolyte brushes, whose degree of ionization (d.i.) can be switched near physiological conditions. This is more promising than conventional strong polyelectrolytes because (i) the degree of ionization (i.e. the charge density) is lower than fully charged polyelectrolytes and (ii) the switching between "charged" and "un-charged" state can occur around neutral pH. As schematically presented in Figure 2, the charging/decharging of the DMAEMA block is expected to alter not only the degree of ionization (electrostatic forces), but also the polymer conformation (entropic forces), degree of hydration (hydration forces), and surface free energy of the film surface (dispersive forces). Thus, this enables the reversible switching of the generic interaction potential between solid surfaces and biological matters (cells, lipid membranes, water soluble proteins, etc.).

Previously, An et al. studied the physisorption of Gibbs monolayers (Figure 3 A) of similar diblock copolymers with 70 mol % and 80 mol % of hydrophilic block (DB 70 and DB 80) to the air/water interface [23, 24, 25] and to the solid/liquid interface [26]. However, although they observed a systematic effect of the pH conditions on the resulting film thickness, the grafting density was found to be very poor (1300 $Å^2$ per polymer chain) to be used as a homogeneous platform for deposition of biofunctional layers [26]. This can be attributed to the limited compressibility of self-assembled glassy MMA backbones, whose statistical segment length coincides with 5 - 6 monomers [27, 28].

To overcome this fundamental problem, a new class of diblock copolymer with equal number of monomers ($n = 36$) from each block (DB 50) was designed for this study. In contrast to DB 70 and DB 80, that form soluble Gibbs monolayers at the air/water interface, DB 50 with a larger fraction of hydrophobic MMA block is expected to form insoluble Langmuir monolayers at the air/water interface (Figure 3 B), where

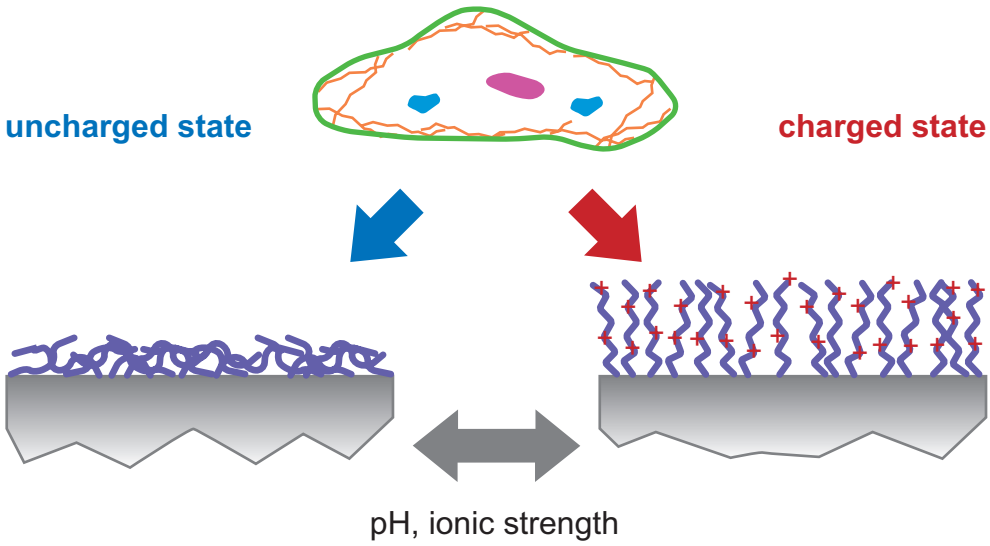

Figure 2: Schematic illustration of switching of polymer conformation due to pH changes. With this induced variation the cell-substrate or membrane-substrate interactions are altered.

the accessible area per molecule and lateral density can be precisely controlled.

In Chapter 4, the Langmuir monolayers of DB 50 monolayers were characterized at the air/water interface. Owing to the large fraction (50 %) of the hydrophobic block, the DB 50 forms a stable Langmuir monolayer at the air/water interface. The in-situ and ex-situ film balance experiments suggest that the hydrophilic block adsorbs to the air/water interface at its uncharged state (pH = 8.5), but stretches into the subphase at the charged state (pH = 5.5). Optimization of the preparation protocols facilitates the fabrication of stable and homogeneous films of DB 50 on hydrophobized substrates at well defined lateral chain densities. Ellipsometry and x-ray reflectivity experiments confirmed that the film thickness can be systematically regulated by the lateral chain densities. In Chapter 5 the detailed structures of DB 50 monolayers at the solid/liquid interface, i.e. the degree of hydration, film thickness, and roughness in aqueous media, were quantitatively investigated by neutron reflectivity. By using heavy water (D_2O) instead of water (H_2O), the contrast in scattering length between hydrogen and deuterium was exploited. Firstly, the global shape of the reflectivity curves of a DB 50 film of low grafting density (are per chain: 435 Å^2) exhibited a distinct difference between pH = 8.5 and 5.5, indicating a clear change in thickness, degree of hydration, and roughness of the diblock copolymer monolayer. The film remained stable against intensive rinsing with buffer and multiple pH titration cycles, which verified the stability and the capability of reversible switching. The interfacial switching was less prominent at higher polymer chain density (area per chain: 340 Å^2), which is attributed to the steric interaction between densely packed polymer

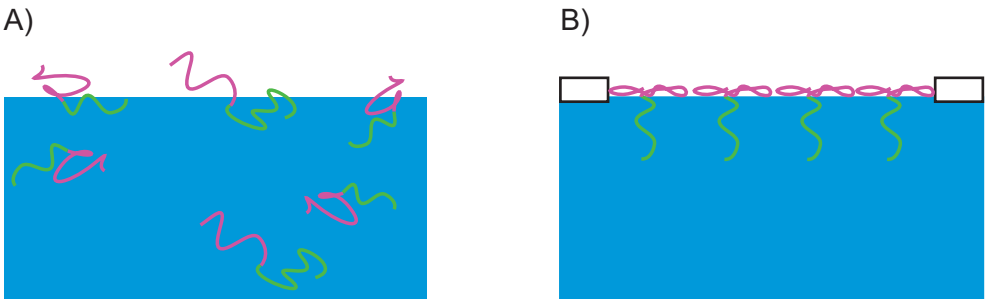

Figure 3: Schematic illustrations of A) a Gibb's monolayer where molecules are in solution as well as adsorbed at the interface and B) an insoluble Langmuir type monolayer with well defined area per molecule.

chains. As the next step to study the interaction between DB 50 films and biofunctional molecules, two series of experiments have been carried out using fluorescence microscopy and neutron reflectivity: (i) nonspecific physisorption of water soluble proteins (bovine serum albumin, BSA), and (ii) spreading of model cell membranes. Although the difference in protein adsorption could hardly be quantified between pH = 8.5 and 5.5, a clear switching of the separation distance between a model cell membrane and a DB 50 film could be observed.

Thus, the obtained results clearly demonstrate that the system established in this study can be utilized as a tunable platform to reversibly switch the interaction between biomembranes and solid surfaces. A simple but straightforward method presented here, strongly suggest its versatile scientific and practical applications, such as attachment and detachment of cells by external chemical stimuli and creating the gradient of interaction potentials. The details of the results are presented in the following chapter.

1. Materials and Methods

In this chapter, all materials and methods used in this study are presented. Since the description of the reflectivity techniques, namely ellipsometry, x-ray and neutron reflectometry needs a more extensive consideration, these techniques are described in a separate chapter.

1.1 Diblock Copolymer

The diblock copolymer poly(2-(dimethylamino)ethyl methacrylate -*block*- methyl methacrylate (DMAEMA-*b*-MMA)was synthesized by the group of S.P. Armes et al. from University of Sussex (U.K.) according to the protocol described elsewhere [29].

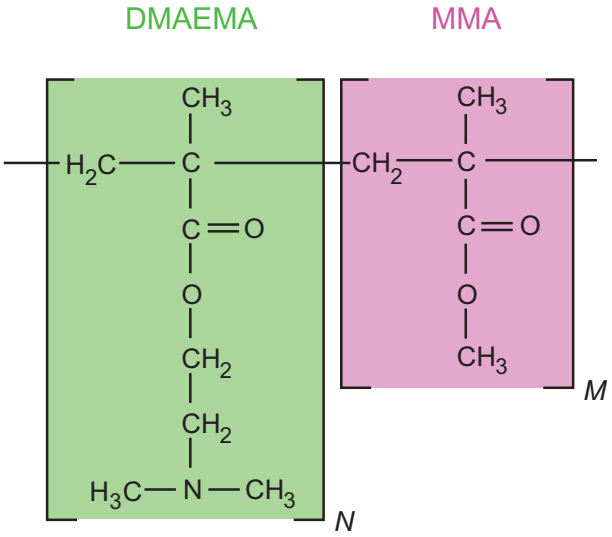

Figure 1.1: Chemical structure of the DMAEMA-*b*-MMA diblock copolymer. The MMA part is hydrophobic and the DMAEMA part can be charged or uncharged depending on the pH. N and M denote the number of monomers.

Figure 1.1 shows the chemical structure of the diblock copolymer. It consists of two types of polymers, a hydrophobic MMA block and a hydrophilic DMAEMA part which is a weak polyelectrolyte with a dimethyl amino group that can be charged or neutral depending on the pH. The pK_a of bulk DMAEMA was found to be 7.3 ± 0.1, whereas the surface $pK_a = 6.7 \pm 0.2$ at the air/water interface, which is different as

found by An and Thomas [30] using a combination of neutron reflection and surface tension measurements. This feature of the diblock copolymer is of special interest because the degree of ionization (d.i.) changes drastically around physiological pH conditions as shown in Table 1.2. The MMA part of the diblock copolymer is hydrophobic and exhibits a glassy behavior at room temperature. Three different compositions of the polymer are listed in Table 1.1.

Compound	DMAEMA ratio	M_w [kD]	M_w/M_n
DB 66	0.66	22.2	1.11
DB 50	0.50	9.3	1.10
DB 42	0.42	9.3	1.10

Table 1.1: Different compositions of the diblock copolymer. M_w is the molecular mass and M_w/M_n the polydispersity index.

subphase pH	degree of ionization (d.i.)
5.5	0.85
6.5	0.61
7.5	0.23
8.5	0.12

Table 1.2: Degree of ionization (d.i.) of DMAEMA part at the surface at different pH conditions taken from Reference [30].

Depending on the percentage of the hydrophilic DMAEMA block, the diblock copolymer is soluble or insoluble in an aqueous solution. Baines et al. [29] found as solubility threshold a minimum of 60% of the hydrophilic block. In order to form a Langmuir monolayer at the air/water interface it is necessary that the polymer is insoluble. On the other hand, the fraction of the chargeable polymer should be as big as possible to yield a bigger effect. With this considerations, DB 66, DB 50, and DB 42 were used in this study.

1.2 Chemicals

If not stated otherwise, all chemicals where purchased from Sigma-Aldrich (Munich, Germany) and used without further purification. The water used throughout this study was deionized ultra pure water from a Millipore (Molsheim, France) purification system with a specific resistance of $R > 18\,\mathrm{M\Omega cm}$.

As buffer, phosphate buffered saline (PBS) was used, consisting of 10 mM of the phosphate salt NaH_2PO_4 and additionally 100 mM NaCl as supporting salt. The buffer was titrated to the desired pH using HCl and NaOH.
Phospholipids for vesicle preparation from Avanti Polar Lipids (Alabaster, USA) were used without any further purification. A detailed list including chemical structures can be found in Appendix A.4.

1.3 Substrates

Several types of substrates were used. For ellipsometry and x-ray reflectivity measurements, silicon wafers was the material of choice because of the flat surface and the material properties. The silicon (100) wafers were a gift from Wacker Siltronic (Burghausen, Germany) and thermally oxidized to an oxide thickness of 150 nm at Infineon (Munich, Germany).
For neutron reflectivity experiments, silicon blocks ($80\times50\times15\,mm^3$) were used. Here, the neutron beam enters the block from the side and is reflected at the solid/liquid interface.
The fluorescence microscopy measurements were carried out with glass cover slides ($24 \times 24\,mm^2$, thickness 0.17 mm) from Karl Hecht KG (Sondheim, Germany).

1.3.1 Cleaning

A clean surface is the basic requirement for further successful modification and functionalization. All substrates were cleaned using a modified RCA method [31, 32] in the following manner:

- Ultrasonication (3 min) and subsequent rinsing with acetone and methanol.
- Ultrasonication in a solution of 1:1:5 (v/v) ammoniumhydroxide (30%) : hydrogenperoxide (30%) : water for 5 min.
- Immersing the substrate into the same solution for 30 min at 60°C.
- Intensive rinsing with water (10 ×).
- Drying at 70°C for 3 h and storing in a vacuum chamber to keep the surface free from bulk water.

1.3.2 Hydrophobization

The clean SiO_2 surface is extremely hydrophilic (contact angle of a water droplet $< 10°$). To render the surface hydrophobic for the Langmuir-Blodgett (LB) and

Langmuir-Schaefer (LS) transfer, two methods were used. The silanization with alkylsilanes uses covalent coupling of the reagent to the surface, while spin coating of poly(methyl methacrylate) (PMMA) only yields a physisorbed film.

Silanization

To prepare the hydrophobic surface required for the LB deposition technique, the wafers were silanized with alkylsilanes, octadecyl trimethoxy silane (ODTMS) in this study. They can couple covalently to the surface –OH groups and form a stable, homogeneous and hydrophobic layer [33]. Immediately after removing the wafers from the vacuum chamber, they were put in a solution of 5 vol % ODTMS and 0.5 vol % butylamine (catalyst) in toluene[1]. The substrates were ultrasonicated for 1 h at 14°C and immersed for 30 min in the same solution. The samples were rinsed intensively with toluene and sonicated for another 2 min, then rinsed with methanol. After evaporation of methanol, the samples were dried at 70°C for 3 h, then stored in a vacuum chamber. Ellipsometry measurements yielded a thickness of 23 ± 2 Å for the monolayer which agrees well with the literature values for a dense monolayer with a tilt angle of approx. 30°.

Spin Coating of PMMA

Another way to hydrophobize the surface is spin coating of PMMA. A solution of approx. 10 mg ml^{-1} of PMMA or d8-PMMA (fully deuterated) in toluene was prepared. The sample was covered with pure toluene and spun for 30 s at 3500 rpm with a Delta 10 spin coater (Süss Mikrotechnik, Garching, Germany). Subsequently, the sample was covered with the PMMA solution and spun for another 60 s at 3500 rpm. Finally, the wafers were stored for 2 h at 120° C and the thickness of the polymer film was measured by ellipsometry. The descried procedure resulted in homogeneous films of approx. 28 ± 2 nm thickness depending on the exact concentration.

1.4 Lipid Bilayer Preparation

Appropriate mixtures of solutions of the desired phospholipids in chloroform were mixed in glass vials. The solvent was evaporated with a jet of dry nitrogen and subsequently the vials were stored in the vacuum chamber for at least 8 h. Afterwards, an aqueous vesicle solution of PBS was prepared by vortexing and incubating at 40° C for 2 h. To get small unilamellar vesicles (SUVs), the solution was extruded 11 times

[1]The used toluene (puriss. grade) was bought from Fluka (Munich, Germany), stored in bottles with molecular sieve under nitrogen atmosphere with crown cap ($H_2O < 0.005\%$).

using a LiposoFast LF-1 extruder (Avestin Inc., Ottawa, Canada) with a filter pore size of 50 nm to get small unilamellar vesicles. A mean diameter of 60 nm for these vesicles was reported by Tutus et al. [34] measured with dynamic light scattering.
To form a lipid bilayer, this solution was very slowly injected into the flow chamber and after 1 h waiting time, the flow chamber was rinsed with PBS at least five times the volume of the chamber to remove any vesicles from the bulk buffer.

1.5 Langmuir Film Balance

1.5.1 Principles of the Langmuir Film Balance

Amphiphilic molecules self assemble in a monolayer at the air/water interface. This monolayer reduces the surface tension of the subphase [35]. With a Langmuir film balance (shown in Figure 1.2) it is possible to monitor the surface tension while controlling the accessible area A_{tot} and therefore the area per molecule A_{mol}. The lateral pressure π can be written as

$$\pi = \gamma_0 - \gamma \tag{1.1}$$

where γ_0 denotes the surface tension of the bare subphase (in case of water $\gamma_0 = 73\,\mathrm{mN\,m^{-1}}$ at $T = 20°\mathrm{C}$) and γ the surface tension of the film-covered surface. Keeping the temperature constant, pressure-area ($\pi - A$) isotherms can be recorded. To measure the surface tension, a Wilhelmy system is used. Here, a piece of filter paper is suspended in the subphase and connected to a spring. The strain of the spring is measured and electronically recorded with a computer.
The force $\vec{F}$ acting on a rectangular Wilhelmy plate with the dimensions l, w, t and density ρ has three different contributions. Gravity acting on the mass of the plate and surface tension are pulling downwards and the buoyant effect of the plate immersed at a height h is pushing it upwards, see Equation 1.2.

$$\vec{F} = \rho glwt + 2\gamma(t + w)cos\theta - \rho_{subphase}gtwh \tag{1.2}$$

In this special case, the buoyancy can be neglected because the density of the filter paper is close to that of pure water. The gravity causes only a constant offset which has to be subtracted. With these considerations we have a linear dependence of the surface tension and the force acting at the Wilhelmy plate. This is only dependent on the circumference of the plate and the contact angle which is assumed to be zero.

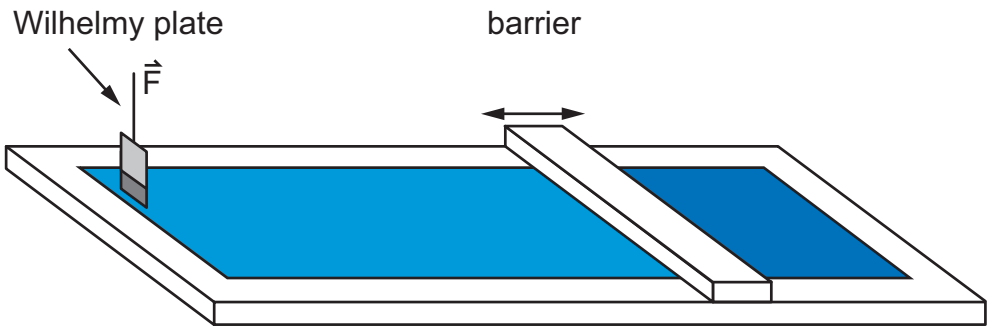

Figure 1.2: Langmuir film balance with a single barrier and a Wilhelmy plate as pressure sensor. The barrier controls the accessible area for the monolayer. The lateral pressure π exerts a force $\vec{F}$ to the Wilhelmy plate which is recorded.

1.5.2 Pressure-Area ($\pi - A$) Isotherms

The pressure-area isotherms in this study were all performed with a self-built film balance made out of Teflon yielding a maximum accessible area of $A_{max} = 1008\,\mathrm{cm}^2$ and a μ-trough with an area of $120\,\mathrm{cm}^2$ (Kibron, Helsinki, Finland). The temperature T was kept constant at 20 °C with an external water bath (Julabo, Seelbach, Germany). To record an isotherm, the appropriate amount of diblock copolymer in a chloroform solution was spread onto the PBS subphase at well defined pH conditions. After 15 min for evaporation of the solvent, the film was compressed with a single barrier at a velocity of $v = 100\,\mu\mathrm{m\,s}^{-1}$.

1.5.3 In-Situ Subphase Titration

For the in-situ subphase titration experiments, the film was compressed to a lateral pressure of $\pi = 20\,\mathrm{mN\,m}^{-1}$. After 5 min waiting time, HCl was injected into the subphase to lower the pH conditions. The area was kept constant and the lateral pressure π was recorded as a function of time.

1.5.4 Langmuir-Schaefer Transfer

To control the grafting density of the transferred monolayers, the area per molecule was adjusted with the barrier prior to the Langmuir-Schaefer transfer [36] at a compression velocity $v = 100\,\mu\mathrm{m\,s}^{-1}$. 5 min after reaching the desired transfer pressure π, the hydrophobized silicon substrate was horizontally lowered with a film lift till contact with the subphase occurs as shown in Figure 1.3. After additional 5 min, the sample was raised again and stored 30 min at 70° C to dry the film. To get rid of the salt on the film, the block was rinsed carefully with water and dried with a jet of N_2.

Subsequently, the film thickness was determined by ellipsometry and the sample was stored for later use in a sealed glass box.

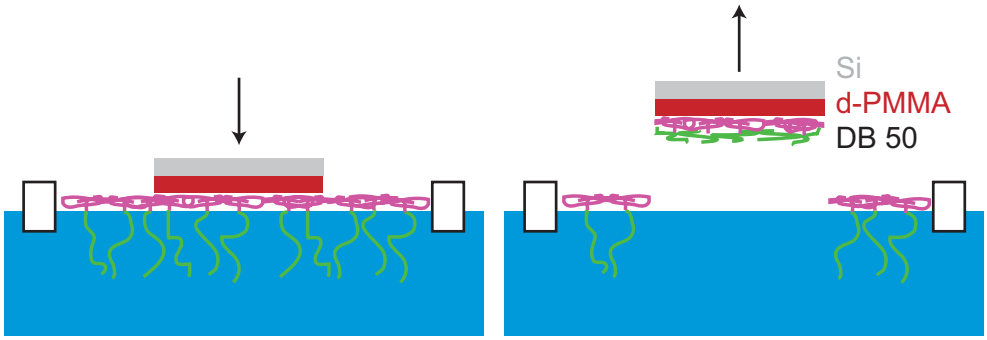

Figure 1.3: Langmuir film Schaefer transfer of the monolayer at the air/water interface to the hydrophobic substrate.

1.6 Contact Angle Measurement

The contact angles of sessile droplets of PBS buffers (at pH = 5.5 and 8.5) on the deposited diblock copolymer films were measured with a FTA 200 contact angle meter (First Ten Ångstroms, Portsmouth, VA, U.S.A.). The obtained droplet shapes were analyzed with an ellipsoidal fit. Further details are given in Section 3.1.5.

1.7 Fluorescence Microscopy

For fluorescence studies, an inverted microscope was used (Axiovert 200, Zeiss, Jena, Germany). As a light source, a high pressure mercury lamp (HBO 100, Osram, Munich, Germany) was installed. The fluorescence images were taken by a cooled CCD camera (Orca ER, Hamamatsu Photonics, Herrsching, Germany), digitized by a frame-grabber card (Stemmer Imaging, Puchheim, Germany), and processed with a home-made imaging software "Open Box" [37, 38]. As fluorescence probe, 7-nitro-2-1,3-benzoxadiazol-4-yl coupled to phosphatidylcholine headgroup (NBD-PC) and the appropriate filter set - a combination of exciter (440/21 nm), dichroic (455 nm), and emitter (510/23 nm) (Omega Filters, USA) - were used.

1.8 Flow Chamber for Neutron Reflectometry

The neutron reflectivity measurements at the solid/liquid interface were done with a flow cell that allowed for buffer exchange and injection of protein or lipid solutions.

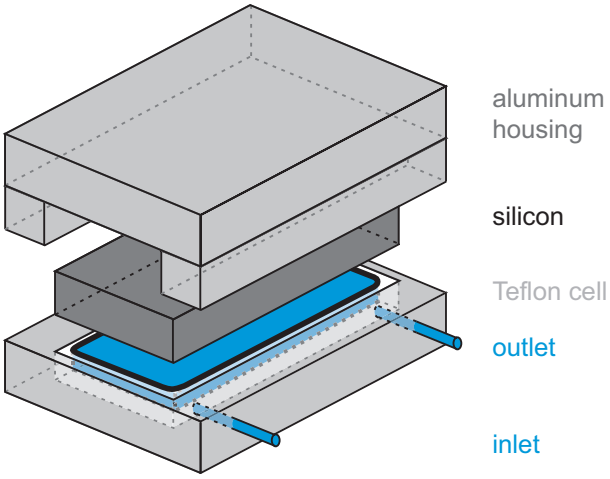

Figure 1.4: Flow chamber for the neutron reflectometry experiments at the solid/liquid interface.

The homemade chamber (shown in Figure 1.4) is a slightly modified version of the design of Satija et al. [39]. Within the aluminium housing the silicon block can be temperated with a water bath and is pressed onto a PTFE chamber with inner dimensions of 72 × 42 × 3 × mm^3. This yields a chamber volume of approximately 11 ml including the tubing. It is sealed with an O-ring out of EDPM-70 (C. Otto Gehrckens GmbH & Co. KG, Pinneberg, Germany) and equipped with an inlet and outlet made out of stainless steel.

1.9 Beamlines

In this section, a brief description of the beamlines used in this study is given.

1.9.1 X-Ray Reflectometer

The x-ray reflectometer (XRR) at the Hahn-Meitner-Institut (HMI) in Berlin (Germany) is a self built diffractometer. The setup is drawn schematically in Figure 1.5. The x-ray beam from a Cu anode passes a line focus (0.04 mm × 8 mm) and hits the sample under an angle θ. After being reflected at the sample, the beam passes a slit (2.0 mm) and is monochromatized with a pyrolytic graphite crystal before entering the detector. To protect the detector from high intensities, like the direct beam or in the range of total reflection, a Ni absorber is inserted in the beam.
The resolution of the instrument is mostly determined by the slits yielding $\Delta q = 0.003\text{Å}^{-1}$. The normalized measured background was constant for all measurements at $I_b = 1.7 \cdot 10^{-7}$.

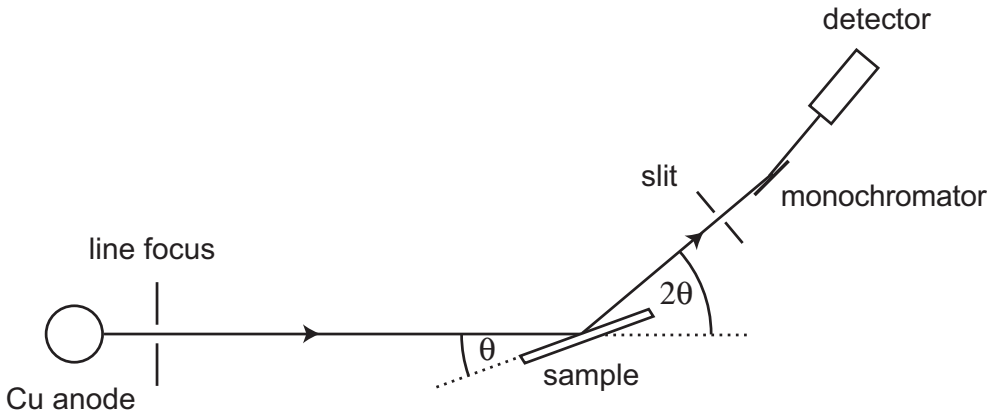

Figure 1.5: X-ray reflectivity setup used at the Hahn-Meitner-Institut (Berlin, Germany). The x-ray beam from a Cu anode passes a line focus and hits the sample under an angle θ. The reflected beam passes a slit and is monochromized with a pyrolytic graphite crystal before entering the detector.

1.9.2 Neutron Reflectometer

The beamline V6 at the BENSC reactor at the HMI (Berlin, Germany) is a horizontal neutron reflectometer operating at a wavelength of $\lambda = 4.66\,\text{Å}$. A detailed description is given elsewhere [40]. Figure 1.6 shows a sketch of the experimental setup. The neutron beam comes from the reactor in a neutron guide and is reflected at a monochromator for wavelength selection. Passing the beryllium filter, all higher harmonic reflections are cut off. With a slit system the beam collimation and resolution can be adjusted. The sample is hit under an angle θ and the reflected intensity is monitored with a position sensitive ^{3}He detector at an angle 2θ.

1.9.3 Neutron Diffractometer

The beamline D16 at the high-flux reactor at Institut Laue Langevin (ILL) in Grenoble (France) is a small momentum transfer neutron diffractometer with variable vertical focussing. It is ideally suited for the study of partially ordered structures, such as stacked membranes, using neutrons with a wavelength of $\lambda = 4.5$ Å. Figure 1.7 shows a sketch of the setup.

The beam is collimated with a slit system either focussing on the sample or the detector. Obeying the width of the neutron beam, the 2D detector is used as a linear detector by integrating over the total out-of-plane intensity. A whole measurement scan is done by setting the detector to a fixed angle and rocking the angle θ of the sample.

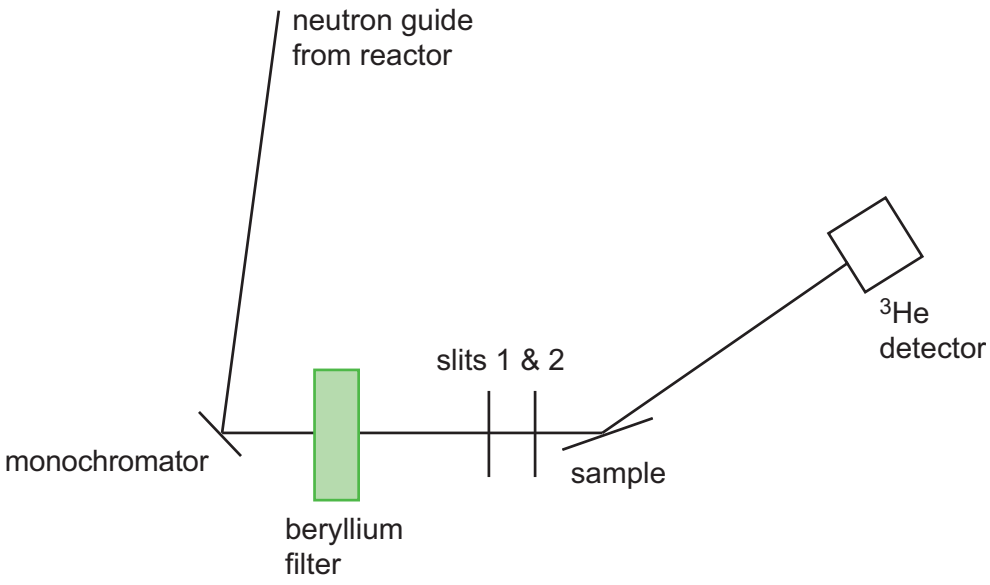

Figure 1.6: V6 neutron reflectivity setup used at the Hahn-Meitner-Institut (Berlin, Germany). The neutrons come from a neutron guide out of the reactor hall and are monochromatized by reflection on a crystal. Higher harmonics of the this Bragg reflection are cut off with a beryllium filter. Then beam passes a two slit system to determine collimation and resolution and is reflected at the sample to the ^{3}He detector.

1.9.4 SAXS/WAXS Beamline

A2 at HASYLAB (DESY, Hamburg, Germany) is a x-ray diffraction beamline for simultaneous measurement of small angle x-ray scattering (SAXS) and wide angle x-ray scattering (WAXS). The x-ray beam with a fixed energy of 8 keV (wavelength of $\lambda = 1.55$ Å) comes from a bending magnet at the storage ring DORIS III (circumference 289.2 m) using a positron beam of 120 mA with an energy of 4.45 GeV. Figure 1.8 shows the setup. The beam hits the sample and two linear detectors record the scattered intensity. Alternatively to the linear SAXS/WAXS detectors it is possible to use a 2D CCD detector (mar USA Inc. Products, U.S.A.) at a variable distance to record the 2D scattering pattern.

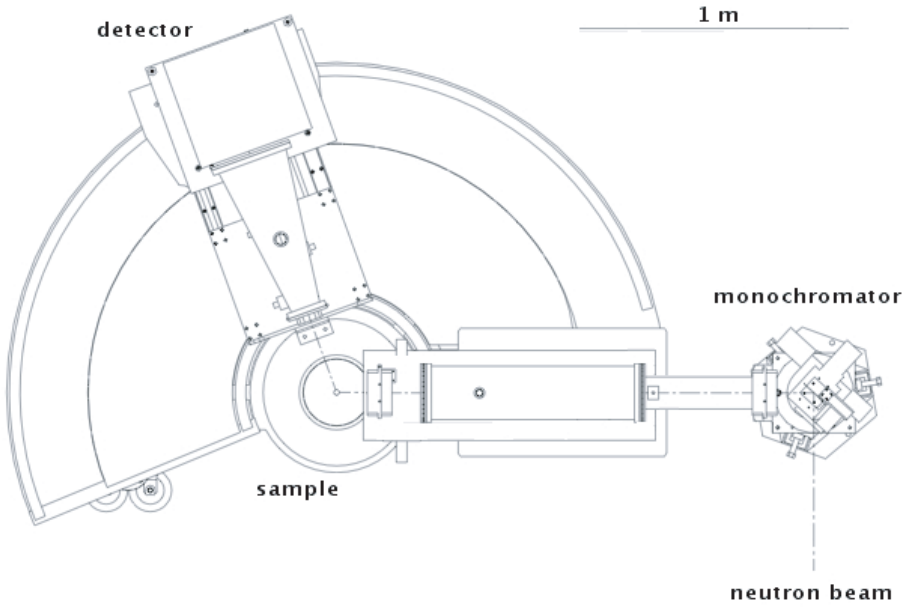

Figure 1.7: D16 beamline at ILL (Grenoble, France). The monochromatized neutron beam hits the sample and is reflected to the 2D ^{3}He detector.

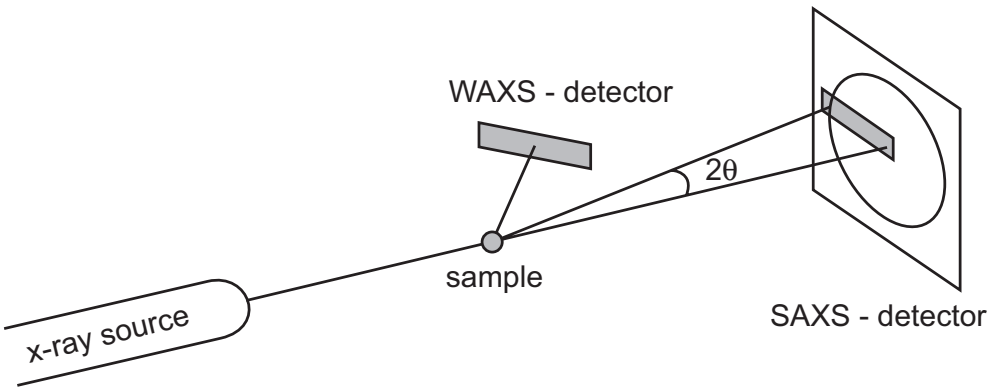

Figure 1.8: A2 Beamline at HASYLAB (DESY, Hamburg, Germany). The X-ray beam from the bending magnet hits the sample and the WAXS and SAXS intensity is recorded simultaneously with two linear detectors.

2. Reflectometry Techniques

Reflectometry techniques are an ideal tool to investigate surfaces because of their non-invasive character and the resulting information about structures normal to the surface as well as in plane patterns. In the following, three types of reflectometry measurements are described.
Ellipsometry uses a polarized electromagnetic wave (mainly visible light) and measures the intensity of the specular reflected beam depending on its polarization state and phase.
X-ray reflectivity (XRR) uses an electromagnetic wave with a smaller wavelength. Here, only the total intensity (square of the amplitude) of the evanescent beam is measured with respect to the incident beam at different angles of incident.
The third technique, neutron reflectometry (NR) uses massive particles (neutrons), which can be described as matter waves. Although yielding a wavelength in the same region as in the case of x-rays, the dispersion relation is significantly different because of their non zero rest mass. In this chapter, the fundamental principles of the three reflectometry techniques (ellipsometry, x-ray reflectivity and neutron reflectivity) will be described.

2.1 Ellipsometry

Ellipsometry is an optical, non-invasive technique suited for the study of layered structures, especially soft interfaces. The term is derived from the word "ellipsometer" coined by Rothen in 1945 [41], who designed the optical instrument for measuring the thickness of thin transparent films deposited on a solid surface in the range from a few up to thousand Å. The apparatus was named like that because it measured the change in elliptical polarization of the light wave reflected at the sample. An apparatus based on similar principles had already been used by Drude in 1889 [42] and others before the introduction of the new "ellipsometer" in 1945.

2.1.1 Theory of Ellipsometry

There is a big number of references treating the theory of ellipsometry and polarized light, one of the most complete descriptions can be found in Azzam et al. [43]. Here, a brief description of the theoretical basis is given.

The theory of ellipsometry is explained in terms of reflection and refraction at planar interfaces of stratified media. The beam of light can be described with the electromagnetic theory as plane wave traveling along the z-axis in a medium with a complex index of refraction $\mathbf{n} = n - ik$ where n is the real part and k the complex part, called the extinction coefficient.

$$\mathbf{E} = \mathbf{E}_0 \, e^{i(\omega t + \delta)} \, e^{-i\omega n z/c} \, e^{-\omega k z/c} \tag{2.1}$$

For the reflection at interfaces, the incident plane wave $\mathbf{E}$ comes through medium 1 and impinges at the interface to medium 2 at an angle ϕ_1. A part of the wave will be reflected and a second one will be transmitted into medium 2. Obeying Maxwell's equations and satisfying the boundary conditions, the angle of incidence must equal the angle of reflection and the angle of refraction is related as

$$\mathbf{n}_1 sin\phi_1 = \mathbf{n}_2 sin\phi_2, \tag{2.2}$$

known as Snell's law. Considering the media as transparent, n_1 and n_2 are real as well as ϕ_1 and ϕ_2.
Having multiple interfaces as shown in Figure 2.1 it is necessary to consider all reflected beams as well as the transmitted beam to gain the two components of the total Fresnel reflection coefficients R_p and R_s parallel and perpendicular to the surface normal.

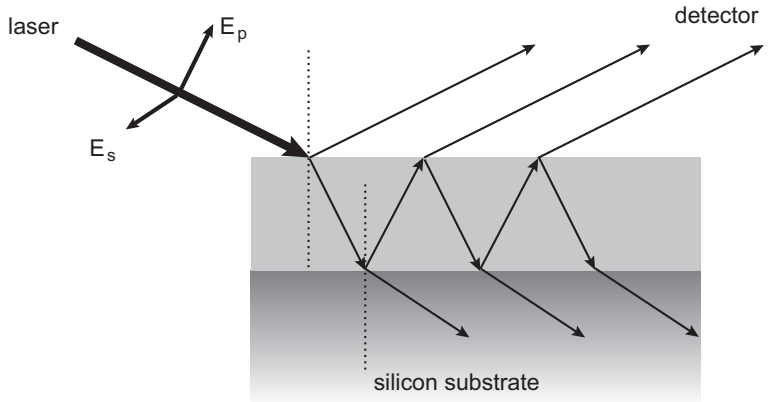

Figure 2.1: Reflection of a laser beam at the interfaces of the multi layer structure. E_p and E_s are the wave vectors parallel and perpendicular to the plane of incidence, which contains the beam and the surface normal.

With the total Fresnel reflection coefficients R_p and R_s, the fundamental equation of ellipsometry (Equation 2.3) can be derived which expresses the two ellipsometric angles Δ and Ψ in relation to R_p and R_s [43]

$$\frac{R_p}{R_s} = \tan\Psi e^{-i\Delta}. \tag{2.3}$$

Δ can vary from 0° to 360° and Ψ from 0° to 90°. From Equation 2.3 one can calculate Ψ directly

$$\tan\Psi = \sqrt{\frac{R_p R_p^*}{R_s R_s^*}}. \tag{2.4}$$

For the determination of Δ two equations are necessary:

$$\cos\Delta = \frac{\mathrm{Re}\,(R_p R_s^*)}{\sqrt{R_p R_p^* R_s R_s^*}} \tag{2.5}$$

and

$$\sin\Delta = \frac{\mathrm{Im}\,(R_p R_s^*)}{\sqrt{R_p R_p^* R_s R_s^*}}. \tag{2.6}$$

The two ellipsometric parameters Ψ and Δ are determined by the polarization states of the light before and after reflection at the sample. Therefore these two angles are the values to be measured. With these, layer thickness and refractive index of a layer can be gained with a least square fit, since an analytical inversion of the complex Fresnel reflection coefficients is not possible.

2.1.2 Ellipsometer

In this study, two kinds of ellipsometers were used. A commercial nulling ellipsometer (Multiskop, Optrel GbR, Berlin, Germany) and a self modified rotating analyzer (rA) ellipsometer (Elli SD 2000, Plasmos GmbH Prozeßtechnik, München, Germany). Both ellipsometers have a polarizer compensator sample analyzer (PCSA) setup as shown in Figure 2.2 and are using a HeNe laser with a wavelength of $\lambda = 632.8\,\mathrm{nm}$. The nulling ellipsometer rotates analyzer and polarizer independently to identify the angles of zero reflected intesity and the rA ellipsometer records the intensity dependence of the angle of the analyzer at a fixed angle of the polarizer. Although the nulling principle yields slightly more accurate values for Ψ and Δ, it has the disadvantage of longer measurement times.

2.1.3 Imaging Ellipsometer

An imaging ellipsometer can measure thickness and refractive index locally resulting in a 2D profile. For this purpose, the intensity at the detector has to be resolved in two dimensions and microscope optics have to be installed. A conventional point-like ellipsometer is modified to an imaging ellipsometer by exchanging the photomultiplier

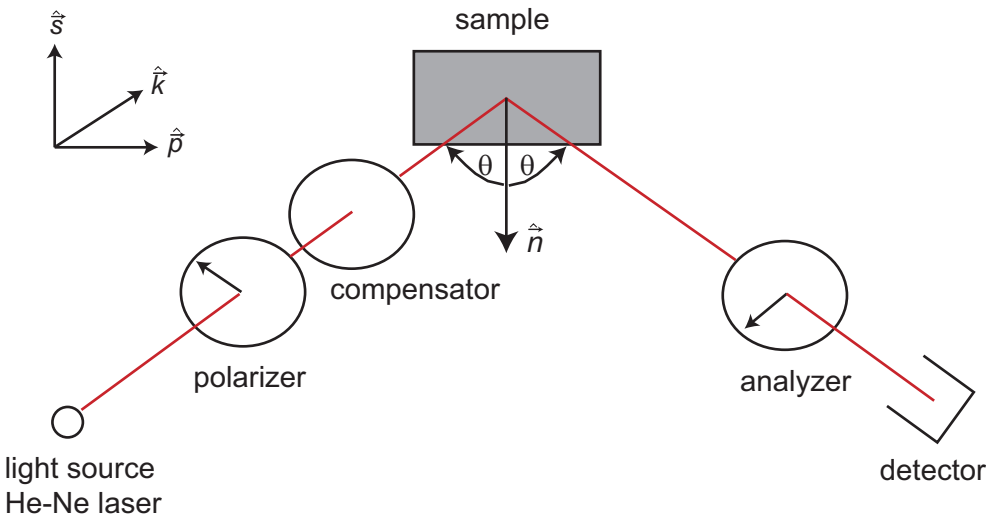

Figure 2.2: Scheme of the polarizer compensator sample analyzer (PCSA) principle of ellipsometry

with a CCD camera and inserting an objective and a tube lens into the beam. Images shown in this study were recorded with a self-built setup using the modifications described.

2.2 X-Ray and Neutron Reflectometry

Since there are many similarities in x-ray (XRR) and neutron (NR) reflectometry, the basic principles and theory will be described together, indicating parameters for XRR with an subscript x and for NR with an subscript N. In the literature numerous detailed reviews about NR and XRR can be found [44, 45, 46]. In the next section the basics of these techniques will be described briefly.

2.2.1 Reflection at a surface

In contradiction to ellipsometry, x-ray and neutron reflectivity measurements record the reflected intensity versus the specular reflection angle θ. However, the phase information in general cannot be determined as it is the case for visible light because of instrumental restrictions.

When x-rays or neutrons impinge on a surface they are reflected. The reflection geometry is depicted in Figure 2.3. The incident beam with wave vector k_i is reflected at the surface at the angle of incidence θ_i resulting in a wave vector k_f. These vectors describe the plane of reflection. The angle between incoming and outgoing beam is then 2θ and the momentum transfer q_z at specular reflection is:

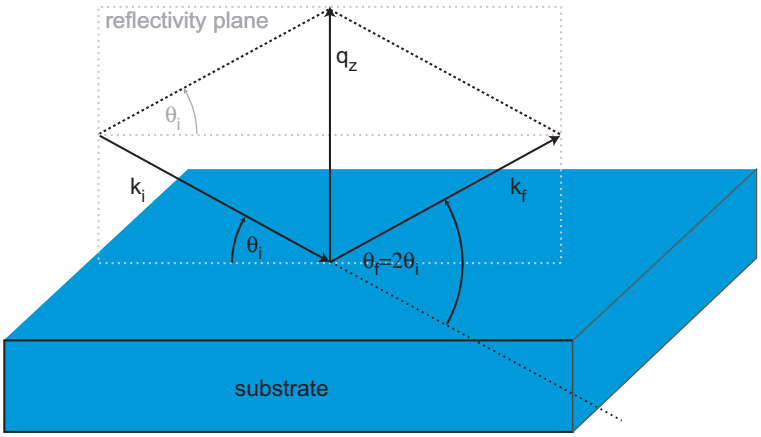

Figure 2.3: Sketch of the reflectivity geometry. The incident beam with wave vector k_i is reflected at the surface at the angle of incidence θ_i resulting in a wave vector k_f. The angle between incoming and outgoing beam is then 2θ and the momentum transfer is q_z.

$$q_z = \frac{4\pi}{\lambda} \sin \theta_{in}. \tag{2.7}$$

Specular x-ray reflectivity and neutron reflectivity measure the reflected intensity depending on the momentum transfer (i.e. specular angle). Using similar considerations as in the preceding chapter the relevant parameter is the complex refractive index $\mathbf{n}$,

$$\mathbf{n} = 1 - \delta + i\beta. \tag{2.8}$$

In the case of x-rays δ_x and β_x can be expressed as:

$$\delta_x = \frac{\lambda^2}{2\pi} r_e \rho_e, \tag{2.9}$$

$$\beta_x = \frac{\lambda}{4\pi} \mu_x, \tag{2.10}$$

where $r_e = 2.818 \cdot 10^{-15}\,\mathrm{m}$ is the classical electron radius, ρ_e the electron density and μ_x the absorption constant of the sample.
The analogous description of n for neutrons of a wavelength λ yields

$$\delta_N = \frac{\lambda^2}{2\pi} N b \tag{2.11}$$

and

$$\beta_N = \frac{\lambda}{4\pi} \mu_n. \tag{2.12}$$

Here b is the coherent scattering length and N the atomic number density. μ_n again is the absorption constant which is negligible in the case of neutrons for most substances

except those containing Li, B, Cd, Sm and Gd where the absorption cross section is large.
If medium 1 is air, Snell's law (Equation 2.2) yields

$$cos\,\theta_1 = n_2\, cos\,\theta_2. \tag{2.13}$$

Since for nearly all materials the refractive index **n** is smaller than unity, there exists a critical angle θ_C below which total reflection occurs and only an evanescent field penetrates into the sample. A very good approximation valid for small angles gives

$$\theta_C \;=\; \sqrt{2\,\delta}. \tag{2.14}$$

The measured quantity using reflectometry techniques is the reflectivity R as a function of the wave-vector transfer q. The reflectivity R is defined as

$$R(\theta) \;=\; \frac{I(\theta)}{I_0} \tag{2.15}$$

or

$$R(q) \;=\; \frac{I(q)}{I_0}. \tag{2.16}$$

Assuming that the electron density or scattering length density in the case of neutrons is continuous the reflection can be treated like in optics (see Section 2.1.2) and the reflected intensity can be obtained using the boundary conditions at the interfaces for the electromagnetical wave leading to the Fresnel equations.
A detailed derivation can be found in [45] and results in:

$$R(q) \;=\; rr* \;=\; \left| \frac{q_z - \sqrt{q_z^2 - q_c^2 - \frac{32i\pi^2\beta}{\lambda^2}}}{q_z + \sqrt{q_z^2 - q_c^2 - \frac{32i\pi^2\beta}{\lambda^2}}} \right|^2 \tag{2.17}$$

When the momentum transfer q is large in comparison to q_c, i.e. $q \;>\; 3\,q_c$ the equation simplifies to the following asymptotic behavior:

$$R(q) \;=\; \frac{q_c^4}{16q^4}. \tag{2.18}$$

In Figure 2.4 measured data points for specular x-ray reflection ($\lambda \;=1.54\,\text{Å}$) at a silicon oxide surface are shown together with the calculated Fresnel reflectivity $R(q)$ and the asymptotic q^{-4} power law which is also known as Porod's law [47]. It can be seen that the power law converges with the Fresnel reflectivity but the measured intensity is dropping too low. This is due to interfacial roughness. All of the descriptions above is valid only in the case of ideal flat interfaces.

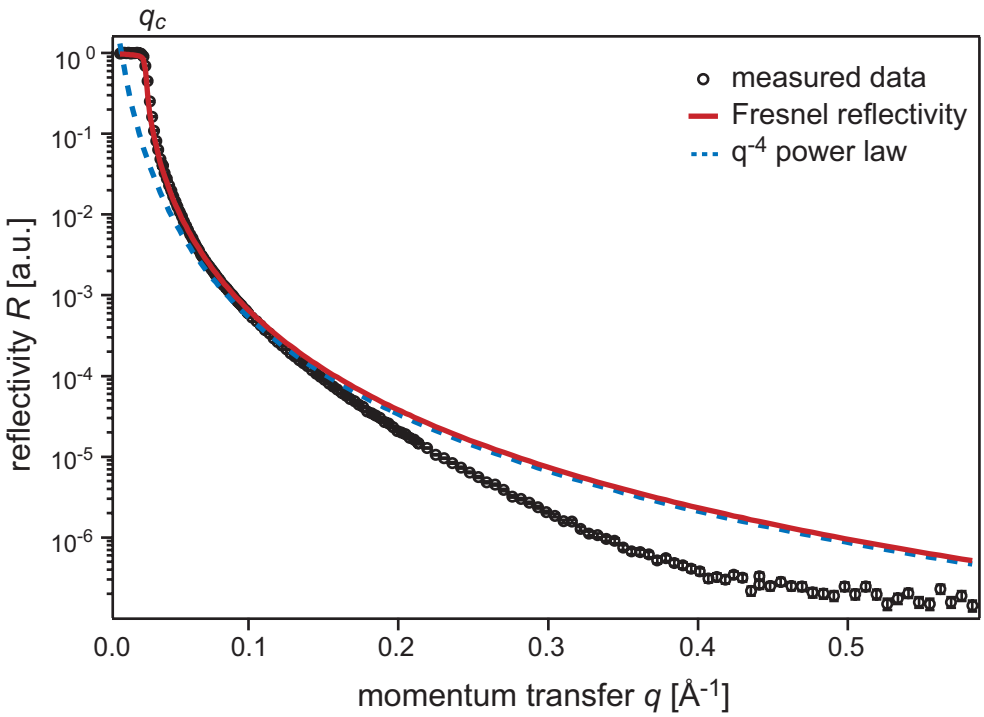

Figure 2.4: The graph shows the measured data points (black circles) for specular reflection at a siliconoxide interface. The red line depicts the calculated Fresnel reflectivity and the broken line the q^{-4} power law.

In real systems all interfaces exhibit a certain roughness that changes the reflectivity. For the further discussion it is important to distinguish between roughness and waviness of the sample. If the curvature of the surface is smaller than the coherence length l_c of the incident beam it is waviness of the surface. This causes the angle of incidence to appear smaller or bigger than it would be at a perfectly flat surface, therefore increasing the divergence of the beam which can be accounted as a worse instrumental resolution. In the other case of the curvature being longer, the surface is called rough. For this case the change in scattering length density from medium 1 to medium 2 is a smooth transition. The main effect of this interfacial or surface roughness is a reduction of the reflected intensity as shown with the measured data in Figure 2.4. An exact, quantitative treatment of surface roughness is extremely difficult and much beyond the scope of this brief description. In the literature several articles and reviews can be found treating the roughness aspect [48].

2.2.2 Reflection from layered sample

The derivation above can be easily expanded to a multi-layered sample. Taking an additional film on top of the substrate into account the Fresnel equations are expanded to another interface. Considering a 100 nm film on a substrate the reflectivity curve will exhibit interference fringes, so called Kiessig fringes. Figure 2.5 shows the calculated Fresnel reflectivity curve for this ideal layered system.

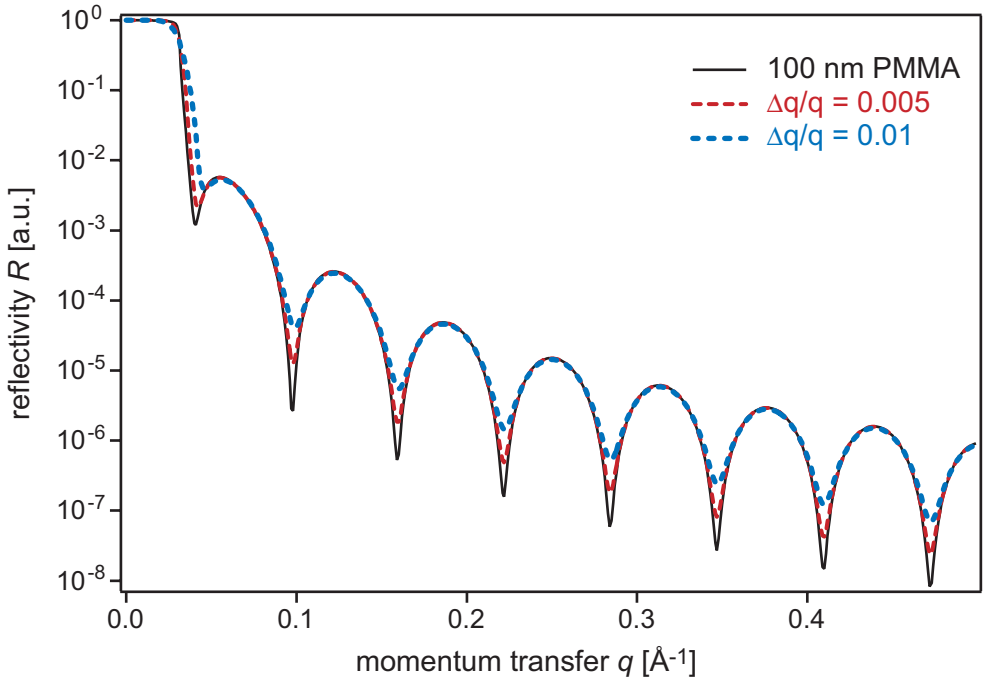

Figure 2.5: Calculated reflectivity for an ideal system of 100 nm PMMA on a silicon oxide substrate. The black line represents the infinite resolution, the red broken line $\Delta q = 0.005\,\text{Å}^{-}1$ and the blue broken line $\Delta q = 0.01\,\text{Å}^{-}1$. The limited resolution smears out the minima.

The thickness of the film determines the position and width of the Kiessig fringes, which makes them an ideal criteria for data analysis of the characteristic thickness. By taking the difference in q from minimum to minimum one can calculate d according to:

$$d = \frac{2\pi}{\Delta q} \tag{2.19}$$

Together with information from other techniques, such as ellipsometry this helps to restrict the models used to fit the reflectivity results and can lead to the scattering length density or electron density of the specimen [44].

Another important parameter for XRR and NR is the resolution of the instrument. The width and height of the beam being reflected is controlled mainly by slit systems

yielding a certain angular resolution $\Delta\theta$. The wavelength resolution $\Delta\lambda/\lambda$ is set by the monochromator being typically of the order of 10^{-3} or less. Therefore, the overall instrument resolution Δq for fixed wavelength reflectometers is determined by the beam divergence and slit dimensions.

In Figure 2.5 two additionally calculated curves are plotted using a resolution of $\Delta\, q = 0.005\,\text{Å}^{-}1$ (red broken line) and $\Delta\, q = 0.01\,\text{Å}^{-}1$ (blue broken line). The finite resolution smears out the minimum positions as well as the critical angle and has to be taken into account for the fit.

In this study the software Parratt32 was used to fit the reflectometry data. This treats the specimen as layers with a certain thickness d, scattering length density Nb and a roughness σ that determines the gradient from one layer to the other giving rise to a smooth transition. The program is named after L.G. Parratt who published in 1954 basic work on reflectometry [49].

3. Theoretical Concepts - Polymers and Surface Forces

In this chapter the basic theoretical concepts concerning interfaces, polymers, and polyelectrolytes and their forces are discussed.

3.1 Surface and Interface Forces

Since this study is dealing with surfaces and flat interfaces, the forces acting in these systems will be considered in the next sections. Controlling the interfacial forces is the key to model cell-cell or cell-surface interactions. Since there is a very complex interplay of different forces, it is important to design special model systems that can be fully understood and easily tuned to the desired parameters. To control the surface properties of the ultrathin polyelectrolyte, the following forces have to be taken into account:

- hard-core or hard-sphere repulsion
- van der Waals force
- steric and entropic polymer forces
- hydration force
- electrostatic force.

3.1.1 Hard-Core Repulsion

On a macroscopic scale, hard sphere repulsion can be schematically described as two billiard balls that cannot penetrate each other. On the microscopic scale, very strong repulsive forces can arise due to overlapping of electron clouds (i.e. quantum mechanical probability functions). If a polymer layer is compressed, the potential corresponding to this repulsion is given by:

$$w(r) = + \left(\frac{\sigma}{r}\right)^n, \qquad n = \infty, \tag{3.1}$$

where σ is the radius of the hard sphere. This simple theta function potential does not allow the compression of spheres. By changing the exponent from infinity to an integer between 9 and 16, one can obtain the power-law dependent potential[2]

$$w(r) = \left(\frac{\sigma}{r}\right)^n, \qquad n = 9...16. \tag{3.2}$$

Another way to describe the hard core repulsion is an exponential dependence on the separation, described by:

$$w(r) = c\, e^{-\frac{r}{\sigma_0}} \tag{3.3}$$

with c and σ_0 being adjustable constants and σ_0 between 0.002 and 0.003 nm. The two later ones are more realistic in that they allow the finite compressibility or "softness" in a molecular level. Even though the theoretical basis is very poor, because of their mathematical convenience this assumption is commonly used [2].

3.1.2 van der Waals Force

Van der Waals (VdW) forces are generally described as dispersion forces, London forces, charge-fluctuation forces, electrodynamic forces, and dipole-induced forces [2]. Thus, in condensed matter this force operates in adhesion, physisorption and structure formation.
The VdW pair interaction potential is given by

$$V_{vdW}(r) = -\frac{C}{r^6}, \tag{3.4}$$

where r is the distance and C is a specific constant.
The VdW potential between two parallel surfaces can be represented as

$$V_{vdW}(r) = \frac{A}{12 \cdot \pi \cdot r^2}, \tag{3.5}$$

where the Hamaker constant A can be calculated by the Lifshitz theory [2].

3.1.3 Hydration Force

Although the theoretical description of hydration forces is difficult, these forces dominate the swelling of polymer films in a wide range of the disjoining pressure. Actually, they measure the energy required to disrupt the ordered water structure when water molecules bind to hydrophilic species (i.e. ionic or H–bonding groups) [2].
Hydration interaction potential obeys an exponential decay law with a characteristic decay length λ_{hydr}:

$$V_{hydr} = V_0 \cdot e^{-\frac{D}{\lambda_{hydr}}} \tag{3.6}$$

$$P_{hydr} = P_0 \cdot e^{-\frac{D}{\lambda_{hydr}}} = \frac{V_0}{\lambda_{hydr}} \cdot e^{-\frac{D}{\lambda_{hydr}}} \tag{3.7}$$

D denotes the seperation and P_0 is an intrinsic pressure. λ_{hydr} had been estimated experimentally, $\lambda_{hydr} = 0.6$Å– 6Å, [2, 50] and P_0 differs from 10^8 Pa up to 10^{12} Pa [51, 50].

3.1.4 Electrostatic Force

In general, the free energy of the coulomb interaction between two charged particles is described as

$$V_{el}(r) = \frac{q_1 q_2 e^2}{4\pi\epsilon\epsilon_0 r}. \tag{3.8}$$

Particles have the charges q_1 and q_2 and a separation r. e is the elementary charge ($e = 1.6022 \times 10^{-19}$ C), ϵ_0 the dielectric constant ($\epsilon_0 = 8.8542 \times 10^{-12}\mathrm{CV^{-1}m^{-1}}$), and ϵ is the relative dielectric constant of the medium.
Since physiological conditions always require aqueous solution including a certain ion concentration, ϵ has to be determined for this environment. Further, this study is dealing with layered stratified media which rises the special interest in the interaction potential between surfaces instead of single particles.
Even pure water at pH = 7.0 contains 10^{-7} M of H_3O^+ ions and is therefore strictly an electrolyte solution. At physiological conditions the ion concentration is much higher (up to 0.2 M). This existence of a "bulk" reservoir of ions effects the electrostatic potential of charged surfaces [2] [52]. Firstly, it is important to know about the ionic distribution in an electrolyte solution at a charged surface. Ions having the opposite sign as the surface charges are called counterions and the other species is named co-ions. Considering a surface at $x = 0$ and an electrostatic potential ψ_x, the density of ions of type i with valency $\pm z_i$ in the solution at any location x is given by the Boltzmann distribution

$$\rho_{xi} = \rho_{\infty i}\, e^{\frac{-z_i\, e\, \psi_x}{kT}}. \tag{3.9}$$

This gives the distribution of co– and counterions in the electrolyte as function of the distance to the interface. Using a monovalent 1:1 salt like NaCl, the boundary conditions of electrical neutrality of the whole system so that $\rho^- = \rho^+$ far away from the surface and the fact that the local potential is affected by the local charge density has to be taken into account. The net charge density is

$$\rho = -2\rho_\infty ze \sinh \frac{ze\psi}{kT} \tag{3.10}$$

Using the Poisson equation

$$\nabla^2\psi = -\frac{4\pi\rho}{\epsilon\epsilon_0}, \tag{3.11}$$

the Poisson-Boltzmann equation is derived

$$\nabla^2\psi = \frac{8\pi\rho_\infty ze}{\epsilon\epsilon_0} \sinh \frac{ze\psi}{kT}. \tag{3.12}$$

Solutions of Equation 3.12 have been studied by Gouy [53], Chapman [54] and Debye and Hückel [55]. The perhaps best-known, is the linearization for small potentials due to Debye and Hückel

$$\nabla^2\psi = \kappa^2\psi, \tag{3.13}$$

where $1/\kappa$ is the Debye length

$$\kappa = \sqrt{\frac{4\pi e^2}{\epsilon\epsilon_0\, kT} \sum_i n_i z_i^2}, \tag{3.14}$$

representing the length scale of the screening.
For example, in a solution with 100 mM NaCl at 25° C, $1/\kappa = 0.96$ nm.

3.1.5 Surface Free Energy and Contact Angle

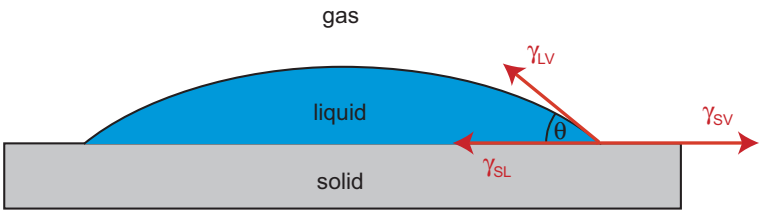

Figure 3.1: Sessile droplet of liquid on a solid surface. The contact angle θ is determined by the interfacial tensions.

When a drop of liquid is placed onto a surface it depends on the surface and liquid properties if it wets the interface and spreads out or if remains as a sessile droplet as shown in Figure 3.1. The contact angle θ of the three phase contact line is determined by Young's equation [56]:

$$\gamma_{LV}\, cos\, \theta = \gamma_{SV} - \gamma_{SL}. \tag{3.15}$$

Here, the solid surface, the liquid droplet and the gas phase must be in equilibrium. The contact angle is determined by the interfacial tensions at the three phase contact line and is a measure of the surface free energy, since a displacement of the liquid changing the covered area A would be accompanied by a change in surface free energy. Therefore, the contact angle can be used to describe the interfacial properties like spreading or wetting of fluids on substrates qualitatively and quantitatively [52].
The stable membrane-substrate contact can be generalized as a complete wetting situation of solids with complex fluids [8, 57, 7]. For instance, the presence of membranes should result in the gain of surface free energy, which can typically be characterized by a positive spreading coefficient S [58, 59].

$$S = \sigma_{SL} - (\sigma_{SM} + \sigma_{ML}) \tag{3.16}$$

Interactions of a complex fluid such as a lipid bilayer with a substrate are dependent on this spreading coefficient S.

3.2 Polymer and Polyelectrolyte Theory

A very short and basic introduction is given to the theory of polymers and polyelectrolytes. In literature, there are several reviews on this topic especially dealing with polymers at interfaces [60, 61].

3.2.1 Flexible Polymers

A polymer is called flexible if the thermal energy is higher than the energy barriers of the backbone rotation. These polymers have a randomly fluctuating three dimensional conformation which can only be described statistically [61]. An ideal chain in dilute solution was firstly described by Kuhn with a universal random walk model [62]. The chain has N bonds, each of length l. Then, with the random walk, the mean square displacement $< R^2 >$ is proportional to N (number of "steps")

$$< R^2 >= l^2 N. \tag{3.17}$$

The radius of gyration R_g, which is the root-mean-square (rms) distance of the segments from the center of mass, is given by

$$R_g^2 = \frac{1}{6} l^2 N. \tag{3.18}$$

Since real polymers have restrictions in the bond geometry, Flory [63, 64] introduced the so-called "characteristic ratio" C_∞, which is a rigidity constant. With this constant, Equation 3.17 is modified to

$$< R^2 >= C_\infty l^2 N. \tag{3.19}$$

For all these considerations, the finite volume of the polymer and solvent effects were neglected. Additionally, attractive van der Waals forces have to be taken into account. The segment-solvent interaction is conveniently described with the Flory-Huggins parameter χ [65]. The excluded volume may be written as vl^3, v being the dimensionless excluded volume parameter.
Finally, a scaling law [63, 64, 66, 67, 68] can be used to describe the conformation of a chain in three dimensions with excluded volume in a good solvent with the critical exponent $\nu = \frac{3}{5}$,

$$R_g^2 = lN^\nu. \tag{3.20}$$

3.2.2 Copolymers

Copolymers are polymer chains composed of two or more different monomer units. An interesting class of copolymers are block copolymers, since they display a rich variety of structures both in solution and at interfaces [61]. A special case is a diblock copolymer which consists of N monomer units of type A and M units of type B. If the hydrophilicity of the two monomers (A and B) is different, these diblock copolymers can form micelles, lamellar or even cubic structures. In this study, a diblock copolymer with a hydrophobic and a hydrophilic block that can be charged or uncharged is used to form an insoluble monolayer at the air/water interface. This is a requirement for the Langmuir-Schaefer transfer method.

3.2.3 Polyelectrolytes

By introducing charges, a simple homopolymer is changed to a polyelectrolyte. Each monomer carries an ionizable group which can be a strong acid or base, so that its charge is independent of the pH. In contradiction to these strong polyelectrolytes, a weak polyelectrolyte carries weak acidic or basic groups. Their degree of ionization (d.i.) strongly depends on the pH. When a polyelectrolyte is dissolved in aqueous solution, the chain will exhibit a certain amount of charges. The polyelectrolyte can be characterized with a length l_e between the charges on the chain. The charges have two main effects: (i) the chain stretches, because the internal repulsion can be minimized in a linear geometry, and (ii) the intramolecular repulsion between chain segments increases [61].
As already discussed for surfaces in Section 3.1.4, any charged particle in an electrolyte solution attracts counterions. Equations 3.12 and 3.14 are yielding the solution for

a flat geometry. Similar screening effects also apply for polyelectrolytes [61]. A stretched, charged polymer chain is best resembled as a cylinder [69]. Since the cylindrical symmetric field diverges at the cylinder axis, very strong non-linear screening effects occur at small separations. This prohibits a straightforward analytical solution [61].

For low charge densities, the so-called Debye-Hückel regime, one can write a potential using $l_{eff} = l_e$. At higher polyelectrolyte charge densities, counterions are strongly trapped (condensation of counterions) due to the field divergence. Here, the effective charge density becomes $l_{eff} = zl_B$, a constant resembling an effective charge of one elementary charge per z Bjerrum lengths [70]. The Bjerrum length is defined as

$$l_b = \frac{e^2}{4\pi\epsilon\, kT} \tag{3.21}$$

and yields the distance between two monovalent ions at which their Coulomb interaction energy equals kT.

4. Diblock Copolymer at Air/Water & Air/Solid Interface

This chapter deals with the properties of diblock copolymer monolayers at the air/water interface and on solid supports (silicon wafers and cover slides), transferred by the Langmuir-Schaefer (LS) technique. The system was characterized with a Langmuir film balance and the dry samples were investigated by contact angle measurements, ellipsometry and x-ray reflectometry. It is shown that by LS deposition stable and reproducible monolayers of DB 50 and DB 42 are transferred onto solid substrates. The special interest in the DMAEMA-*b*-MMA diblock copolymers lies in the charging/decharging of the DMAEMA part around physiological pH conditions. Previous works of An et al. showed already the physisorption of DB 80 and DB 70 from solution to hydrophobic substrates [26]. These studies had the disadvantage of a very low grafting density due to the self avoidance of the polymer chains during the self-assembly process of physisorption. A monolayer transfer at well controlled area per molecule A_{mol} is possible with the Langmuir-Schaefer technique. A prerequisite for this method is an insoluble Langmuir monolayer at the air/water interface. Therefore, the physical properties of three types of DMAEMA-*b*-MMA copolymers were investigated with a Langmuir-type film balance.

4.1 Langmuir Isotherms

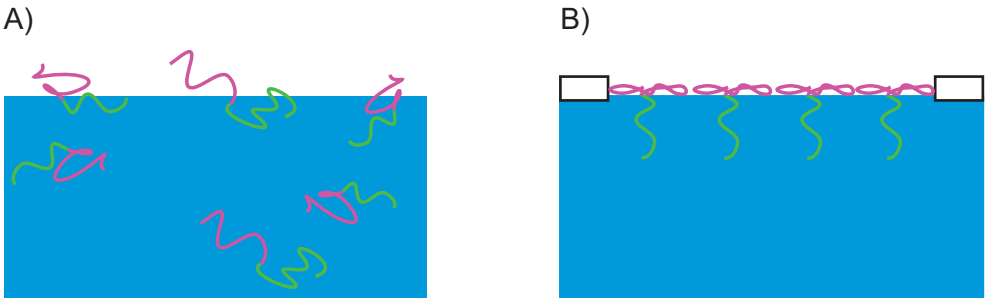

Figure 4.1: Schematic illustrations of A) a Gibb's monolayer where molecules are in solution as well as adsorbed at the interface and B) an insoluble Langmuir type monolayer with well defined area per molecule.

All Langmuir isotherms were recorded as described in Section 1.5.2. The first type of diblock copolymer used was DB 66, the DMAEMA part being 66 % of the number of monomers. The film balance isotherms recorded and measurements at a constant area of this molecule showed a steady decrease of pressure over time. This behavior indicates a finite solubility of the molecule thus forming rather a Gibb's than a Langmuir monolayer. The two schemes are depicted in Figure 4.1. These observations are in agreement with the findings of Baines et al. [29]. They showed the solubility of the DMAEMA-*b*-MMA block copolymers down to a ratio of 66 % of the hydrophilic DMAEMA part but the next lower composition was 50 % which was insoluble. Since this prevents the precise control of the area per molecule A_{mol}, the composition of choice has to have a smaller fraction of the hydrophilic block, namely 50 % (DB 50) or 42 % (DB 42).
Figure 4.2 shows the isotherms at two different pH conditions (red line corresponds to pH = 5.5 and the blue line to pH = 8.5, respectively).

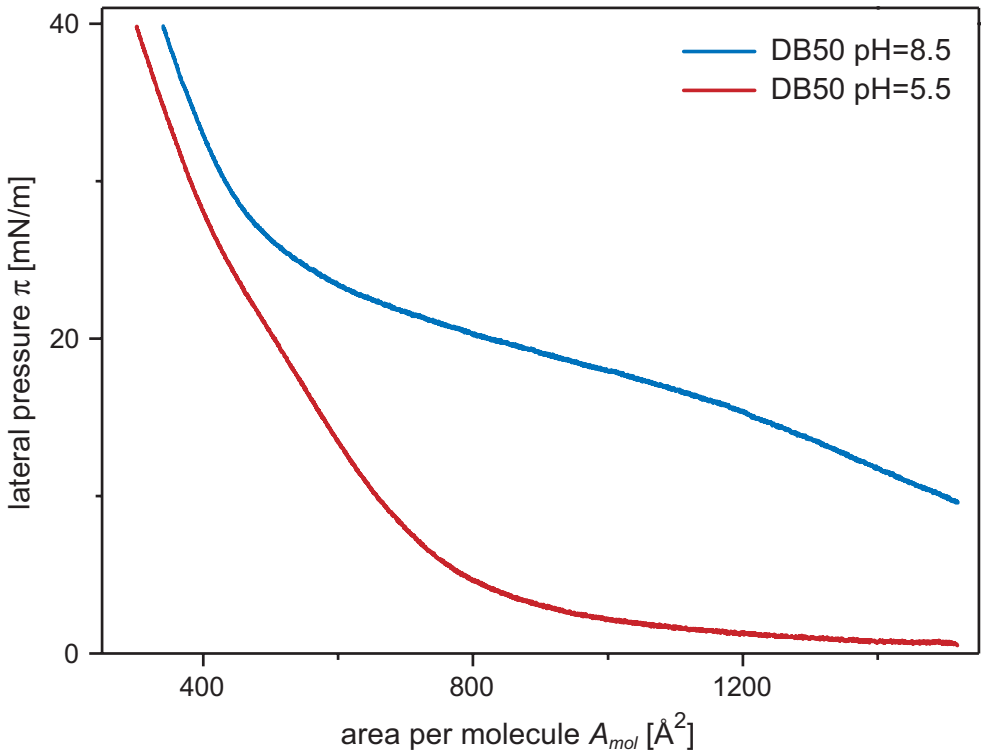

Figure 4.2: Langmuir isotherms of DB 50 at pH = 5.5 and pH = 8.5

It is obvious from Figure 4.2 and Table 4.1 that the behavior of the diblock copolymer strongly depends on the pH of the subphase. This is due to the fact, that the degree of ionization (d.i.) of the DMAEMA block changes significantly as shown in 1.2. In the low pressure regime ($\pi < 25\,\mathrm{mN\,m^{-1}}$), the area per molecule needed at pH = 8.5

π[mNm^{-1}]	A_{mol} (pH = 5.5)	A_{mol} (pH = 8.5)	ΔA
40	300 ± 5Å^2	340 ± 5Å^2	40 Å^2
35	338 ± 5Å^2	380 ± 5Å^2	42 Å^2
30	381 ± 5Å^2	432 ± 5Å^2	51 Å^2
25	435 ± 5Å^2	537 ± 5Å^2	102 Å^2
20	505 ± 5Å^2	825 ± 5Å^2	320 Å^2
15	576 ± 5Å^2	1215 ± 5Å^2	639 Å^2

Table 4.1: Area per molecule A_{mol} per DB 50 molecule shown for pH = 5.5 and pH = 8.5 and the difference ΔA with respect to the lateral pressure π.

is much bigger than for pH = 5.5, but in the high pressure regime the difference decreases. Such behavior can be explained with the adsorption of the DMAEMA block to the interface due to lack of charges and therefore less hydrophilicity compared to the highly charged state at pH = 5.5.

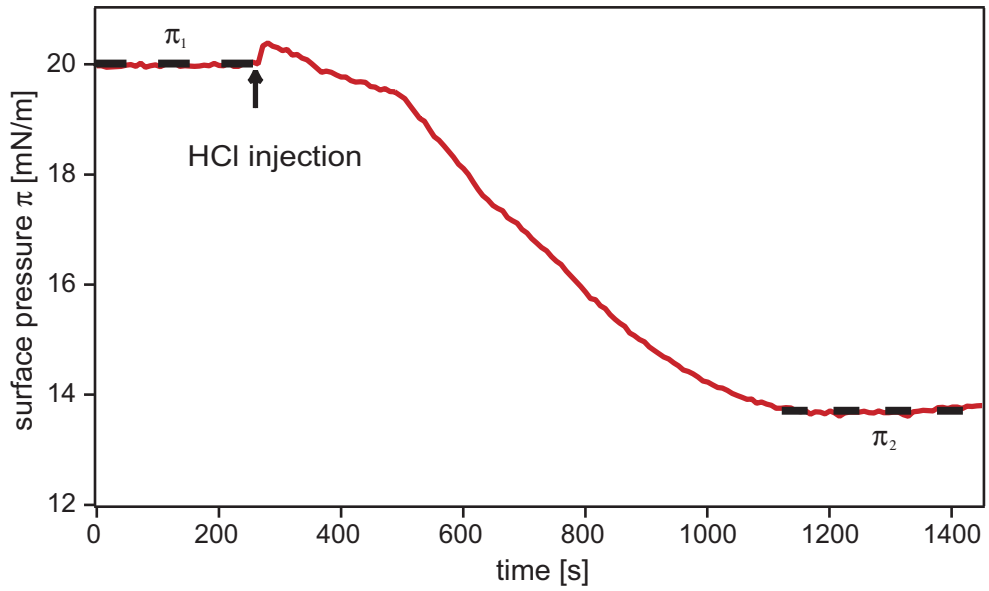

Figure 4.3: In-situ titration experiment at constant area. The DB 50 monolayer was compressed up to a lateral pressure of $\pi = 20$mN m^{-1}. After 5 min waiting time, HCl was injected into the subphase to lower the pH conditions. The surface pressure decreases drastically after the injection.

To further investigate this circumstance, a pH titration experiment according to Section 1.5.3 was performed at a constant area per molecule which is shown in Figure 4.3. The film was compressed to a lateral pressure of $\pi = 20$ mN m^{-1}. After 5 min waiting time, HCl was injected into the subphase to lower the pH conditions. Then the surface pressure decreases drastically to $\pi \approx 14$ mN m^{-1} after the injection of HCl.

Previously, Ahrens and Helm [71] reported the condensation of counter ions in diblock copolymer monolayers, whose hydrophilic block is a strong polyelectrolyte (polystyrene sulfate). Using specular x-ray reflectometry at the air/water interface, they postulated the condensation of counter ions in charged polymer brushes [72].

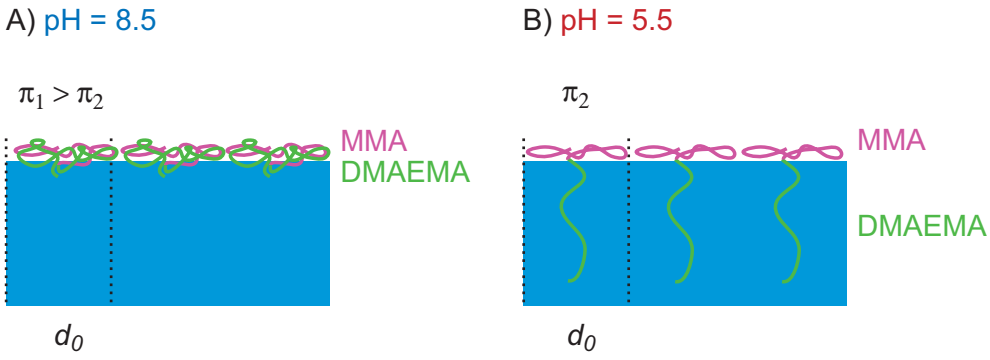

Figure 4.4: Sketch of the conformation of DB 50 monolayer at the air/water interface. (A) shows the polymer adsorbed at the interface at pH = 8.5 and (B) at pH = 5.5 the mostly charged DMAEMA block stretches out into the subphase.

The impact of the ionic strength of the subphase on the DB 50 monolayer was examined by measuring Langmuir isotherms with different salt concentrations as shown in Figure 4.5. In fact, the isotherms of the charged DB 50 monolayer (pH = 5.5, stabilized with 10 mM PBS) showed only a very small difference in the presence or absence of the additional supporting salt 100 mM NaCl. Especially above 10 mN m^{-1} the curves are identical. This result suggests that the counter ions are condensed in charged DMAEMA brushes at pH = 5.5 even at a low ionic strength of the bulk subphase. The isotherms at pH = 8.5 exhibit no remarkable effects of ionic strength, indicating that the 10 mM phosphate buffer is already sufficient for the counter ion condensation.

To further analyze the Langmuir isotherm one can deduce the compressibility of the monolayer as:

$$\chi = -\frac{1}{A}\left(\frac{\partial A}{\partial \pi}\right)_T . \tag{4.1}$$

The compressibility χ of a monolayer is the two dimensional analogue to the three dimensional compressibility of a bulk system. It yields the relation between external strain and the answer of the material. Therefore, it can be used to describe the physical properties of a substance dependent on the external conditions.

Figure 4.6 shows the compressibility of the DB 50 monolayer deduced from the isotherms recorded at pH = 5.5 and pH = 8.5 presented in Figure 4.2, respectively. Here, the lateral compressibility of a DB 50 monolayer at low surface pressures strongly depends

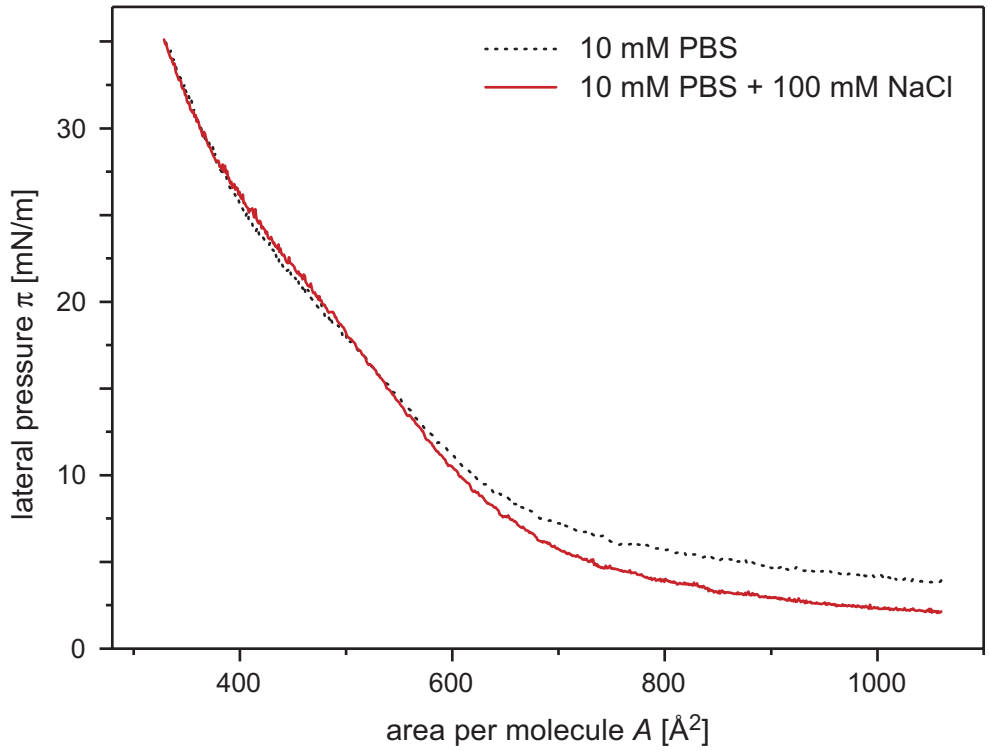

Figure 4.5: Langmuir isotherms of DB 50 on a PBS subphase at pH = 5.5 with (solid red line) and without (broken black line) 100 mM NaCl yielding nearly the same curves.

upon the adsorption of the DMAEMA block to the air/water interface. For example, the compressibility for the charged polymer (d.i. = 85 %) at $\pi = 10\,\mathrm{mN\,m^{-1}}$ is $\chi = 1.3 \times 10^{-5}\,\mathrm{m\,mN^{-1}}$, while $\chi = 8.0 \times 10^{-5}\,\mathrm{m\,mN^{-1}}$ for the uncharged monolayer (d.i. = 12 %). On the other hand, the compressibility is rather dominated by that of the glassy MMA block at high surface pressures ($\pi > 30\,\mathrm{mN\,m^{-1}}$), where the χ values for uncharged and charged monolayers become comparable: ($\chi = 1.8 \times 10^{-4}\,\mathrm{m\,mN^{-1}}$ and $\chi = 2.6 \times 10^{-4}\,\mathrm{m\,mN^{-1}}$, respectively).

DB 42 showed similar isothermal behavior with a shift in the molecular area A_{mol} to higher values. This is due to the bigger hydrophobic MMA part. With this results for all further experiments DB 50 was used because of the higher fraction of the hydrophilic block and higher possible grafting density (i.e. smaller molecular area A_{mol}).

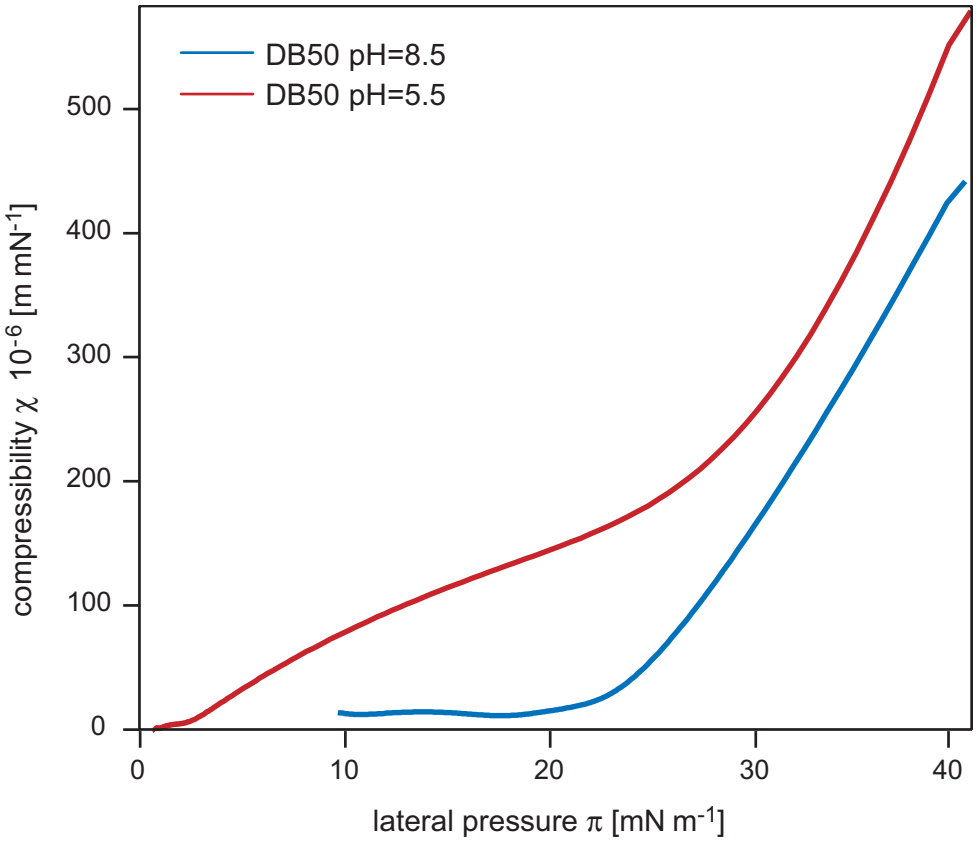

Figure 4.6: The two curves show the compressibility of the DB 50 monolayer at pH = 5.5 (red line) and pH = 8.5 (blue line). In the low pressure region, the difference is obvious, whereas in the higher pressure region, the curves become more similar yielding the finite compressibility of the glassy MMA part.

4.2 Diblock Copolymer at Solid/Air Interface

The monolayers of diblock copolymer transferred by the LS technique onto solid substrates (see Section 1.5.4) are analyzed with various techniques to determine surface and film properties. Two different coatings to hydrophobize the surface - spin coated films of d-PMMA and covalently coupled alkyl silane monolayers - were used. The hydrophilic/-phobic nature of the interface was investigated in terms of contact angle of a sessile droplet of water or PBS, respectively. The thickness of the dry films was measured with ellipsometry and x-ray reflectometry.

4.2.1 Influence of Hydrophobization on LS Transfer

As already mentioned two different coatings of the silicon substrates were used to render the surfaces hydrophobic. Firstly, ODTMS was covalently coupled to the silicon oxide as described in Section 1.3.2. This leads to a uniform dense layer of alkyl chains of a thickness $h = 2 \pm 0.5\,\text{nm}$ that yield a contact angle with water of up to 105°. The second method was spin coating of d8-PMMA as described in Section 1.3.2. Here, a thickness in the range of 20 nm to 30 nm was obtained depending on the concentration of the d8-PMMA solution. The second method is the prerequisite for the neutron reflectometry measurements, because a deuterated contrast layer is needed with a thickness of at least 20 nm.
The LS technique was applied to both hydrophobic substrates and the homogeneity and stability of the resulting diblock copolymer monolayers was analyzed. It was found that the transferred DB 50 films on d8-PMMA were more uniform and more stable against rinsing with water as the films on ODTMS, respectively.
This behavior can be explained in the context of the self affinity of d8-PMMA as hydrophobic coating and PMMA as the hydrophobic counter part for the LS deposition. It seemed, that the hydrophobicity of ODTMS was too big to yield a homogenous monolayer. For all further experiments d8-PMMA was used as precursor coating of the silicon substrates.

4.2.2 Contact Angle Measurements

The contact angle θ of sessile droplets of PBS (at pH = 5.5 and 8.5) on the deposited DB 50 films transferred at different pH conditions were measured according to 1.6 to determine the hydrophilicity/-phobicity of the polymer film. The measured values are listed in Table 4.2.
The films transferred at pH = 8.5 showed a high contact angle of $\theta = 88°$ in contact with a droplet at pH = 8.5. Such a high contact angle is actually comparable to that of a hydrophobic d8-PMMA precursor film. When the same film is in contact

LS transfer at	droplet pH = 5.5	droplet pH = 8.5
pH = 5.5	52°	55°
pH = 8.5	78°	88°

Table 4.2: Contact angle θ of sessile droplets of PBS at different pH (5.5 and 8.5) on DB 50 films transferred at different pH conditions.

with a droplet at pH = 5.5, the contact angle decreased to $\theta = 78°$, which can be explained by a slight increase in the polarity of DMAEMA block due to the charging of DMA groups at pH = 5.5. However, the high contact angles observed here imply that the poor separation of the MMA and DMAEMA blocks at the air/water interface is preserved even after the film transfer. In fact, the contact angle measurements showed hysteresis in receding contact angles and pinning centers deforming the contact line suggesting the local chemical heterogeneity of the surface due to the entanglement of MMA and DMAEMA blocks. On the other hand, the films transferred at pH = 5.5 (d.i. = 85 %) showed a significantly smaller contact angle of $\theta = 55°$ in contact with a droplet at pH = 8.5. The contact angle became even smaller, $\theta = 52°$, when the surface is in contact with a droplet at pH = 5.5. The remarkably smaller contact angles observed for the films transferred at pH = 5.5 directly imply that the separation of two blocks before the transfer is the key to maximize the hydrophilic blocks on the surface. In fact, the difference between static and receding contact angles on the films prepared at pH = 5.5 was smaller than that prepared at pH = 8.5. Taking these results into account, all further film preparations were performed with a subphase at pH = 5.5.

4.2.3 X-Ray Reflectivity and Ellipsometry Measurements

substance	$n(\lambda = 633\,\text{nm})$	$V[\text{Å}^3]$	$\rho\ [10^{-5}\,\text{Å}^{-2}]$	$\Im(\rho)[10^{-7}\,\text{Å}^{-2}]$
silicon	3.868 - i 0.024			
silicon oxide	1.462		1.98	1.18
d8-PMMA	1.49	140	1.36	1.41
DB 50	1.5	365		

Table 4.3: Material constants used for ellipsometry and XRR analysis.

The thickness of dry DB 50 films transferred at 15, 25, and 35 mN m^{-1} were firstly measured by ellipsometry according to Section 2.1. At the three transfer pressures the areas per molecule were $A = 576 \pm 10\,\text{Å}^2$ (15 mN m^{-1}) , $435 \pm 7\,\text{Å}^2$ (25 mN m^{-1}), and $338 \pm 5\,\text{Å}^2$ (35 mN m^{-1}), respectively. In comparison to the grafting densities

of physisorbed DB 70 and DB 80 ($A_{mol} \approx 1300\,\text{Å}^2$ per molecule) reported by An et al. [26], 2 - 3 times higher grafting densities are achieved by compression of the Langmuir monolayers at the air/water interface. The film thickness of silicon dioxide, d8-PMMA, and DB 50 was measured after the deposition of each layer by using the refractive indices given in Table 4.3. The mean values of the diblock copolymer layer thickness from more than five independent measurements are summarized in Table 4.4. These film thickness obtained from macroscopically large surfaces (laser beam diameter of 1 mm, the separation of individual measurement points of 2 mm) are found to be very uniform, yielding the thickness deviation of ± 5 Å throughout the experiments. These errors are comparable to those of the underlying silicon dioxide and d8-PMMA, suggesting that the homogeneity of DB 50 films is independent from the transfer pressures. In fact, the r.m.s. roughness values of the DB 50 films obtained by atomic force microscopy (tapping mode AFM for $1 \times 1\,\mu\text{m}^2$ and $5 \times 5\,\mu\text{m}^2$) were between 5 Å and 10 Å.

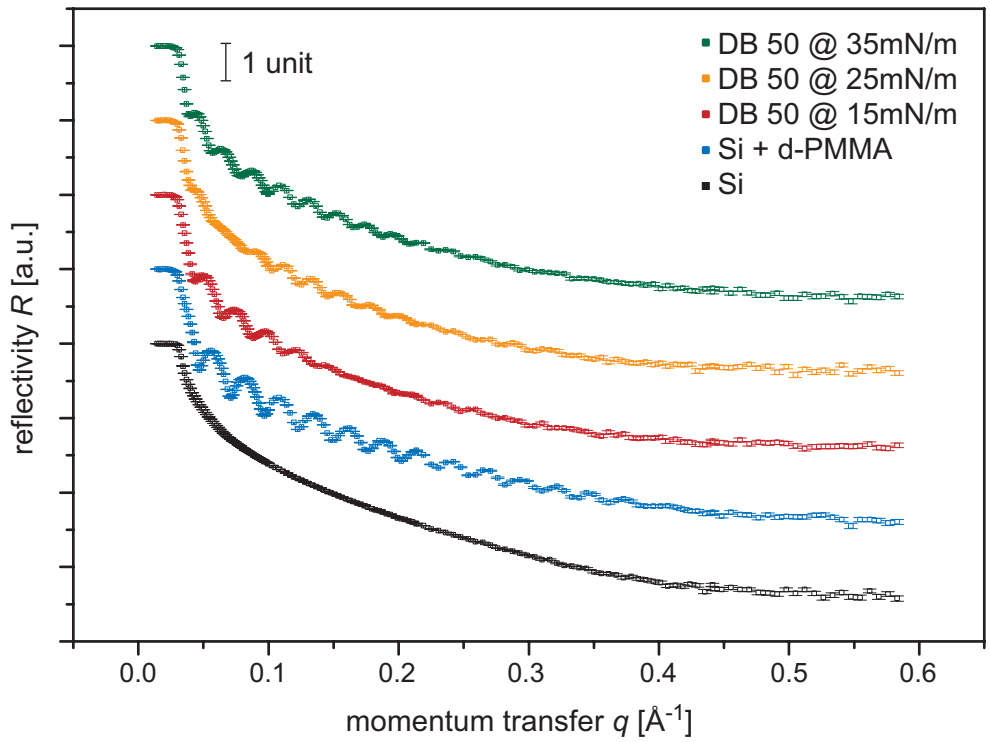

Figure 4.7: X-ray reflectivity curves (I/I_0 vs. q) of a bare silicon wafer (black), a silicon wafer coated with d8-PMMA (blue), silicon wafers with d8-PMMA and DB 50 transferred at 15 mN m^{-1}(red), 25 mN m^{-1}(yellow), and at 35 mN m^{-1}(green).

The transferred DB 50 films were also characterized by specular x-ray reflectivity experiments. In comparison to ellipsometry that can determine only the layer thickness by assuming a refractive index, x-ray reflectivity is advantageous since one can gain

π[mNm^{-1}]	A_{mol} [Å^2]	h [Å] ellipsometry	h [Å] x-ray
15	576 ± 10	39 ± 5	39 ± 5
25	435 ± 7	54 ± 5	50 ± 5
35	338 ± 5	67 ± 5	64 ± 5

Table 4.4: Area per molecule A_{mol} at the air/water interface and thickness h of DB 50 at the air/solid interface at different pressures π.

both the layer thickness and the roughness of the interface using the electron densities of individual layers. Figure 4.7 represents the reflectivity curves (I/I_0 vs. q) of the bare silicon wafer with 150 nm thick oxide layer (black), a silicon wafer spin coated with d8-PMMA (blue), silicon wafers with d8-PMMA and DB 50 transferred at 15 mN m^{-1}(red), 25 mN m^{-1}(yellow), and at 35 mN m^{-1}(green). According to the four box model (air, DB 50, d8-PMMA, and silicon dioxide) and the real and imaginary parts of the electron densities (Table 4.3), the thickness of DB 50 films can be calculated to be $h = 37$ Å (15 mN m^{-1}), 50 Å (25 mN m^{-1}), and 64 Å (35 mN m^{-1}), respectively. The calculated values show an excellent agreement with those obtained by ellipsometry (Table 4.4), indicating an increase in film thickness according to the film compression. If one assumes a constant volume V_0 of the polymer, a systematic dependence of the dry DB 50 layer thickness h on the area per molecule A_{mol} can simply be written as:

$$h = \frac{V_0}{A_{mol}} \tag{4.2}$$

Taking the molecular volumes of 225 Å^3 for DMAEMA monomer and 140 Å^3 for a MMA monomer [23] , the total volume of the DB 50 macromolecule can be roughly estimated to be $V_0 = 1.3 \times 10^4$ Å^3 [24]. If one plots the thickness h vs. area A_{mol} relationship based on V_0 (the line given in Figure 4.8), a clear deviation can be seen between the predicted thickness and the experimental results. This discrepancy from an ideal (simple) system is explained by the finite compressibility of glassy polymer chains, which are different from simple solids or liquids. The dry film exhibits voids due to entanglement of the chains and the strong dissipating forces due to the drying process which obviously let it appear thicker than the ideal molecular model but still yields the same tendency.

To conclude, in this chapter it was demonstrated that the DB 50 molecule forms an insoluble monolayer at the air/water interface and exhibits large differences in its area per molecule A_{mol} at different pH conditions. Using this property, the Langmuir-Schaefer technique was applied successfully to transfer monolayers of the

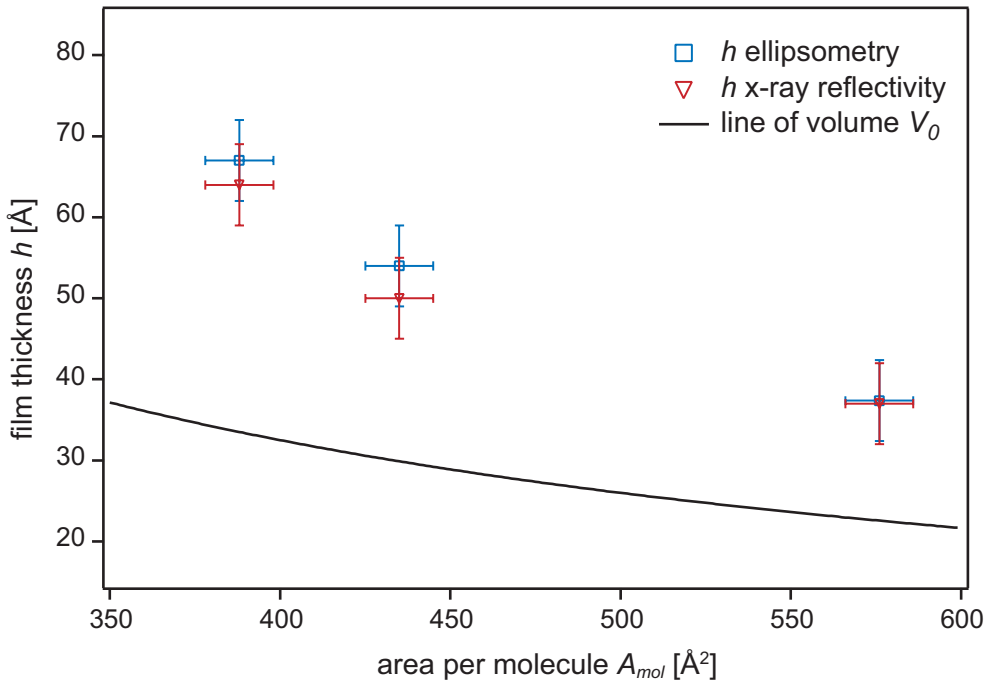

Figure 4.8: Dry film thickness measured by ellipsometry (black squares) and x-ray reflectivity (blue squares) plotted versus area per molecule, indicating a systematic dependence of film thickness on the lateral chain density. A clear deviation from the simple constant volume model can be explained by the finite compressibility of glassy polymer chains, which are different from simple solids or liquids.

diblock copolymer onto hydrophobized substrates. The transfer worked better with the PMMA spin coated samples than the ODTMS substrates. This is due to the self affinity of the PMMA which is the hydrophobic block of the DB 50 and the hydrophobic coating of the silicon wafer. The transferred films remained stable even after rinsing several times with water and could be quantitatively analyzed by ellipsometry and x-ray reflectivity.

5. Diblock Copolymer at the Solid/Liquid Interface

After establishing the diblock copolymer system on solid supports, the monolayer was investigated in aqueous environment at the solid/liquid interface. This chapter deals with the conformational change of the DB 50 due to different subphase conditions as well as with protein adsorption and lipid bilayer formation. Due to constraints in the experimental setups of ellipsometry and x-ray reflectivity, the best suited technique for this purpose is neutron reflectometry (NR).

5.1 pH Dependent Changes in Aqueous Solution

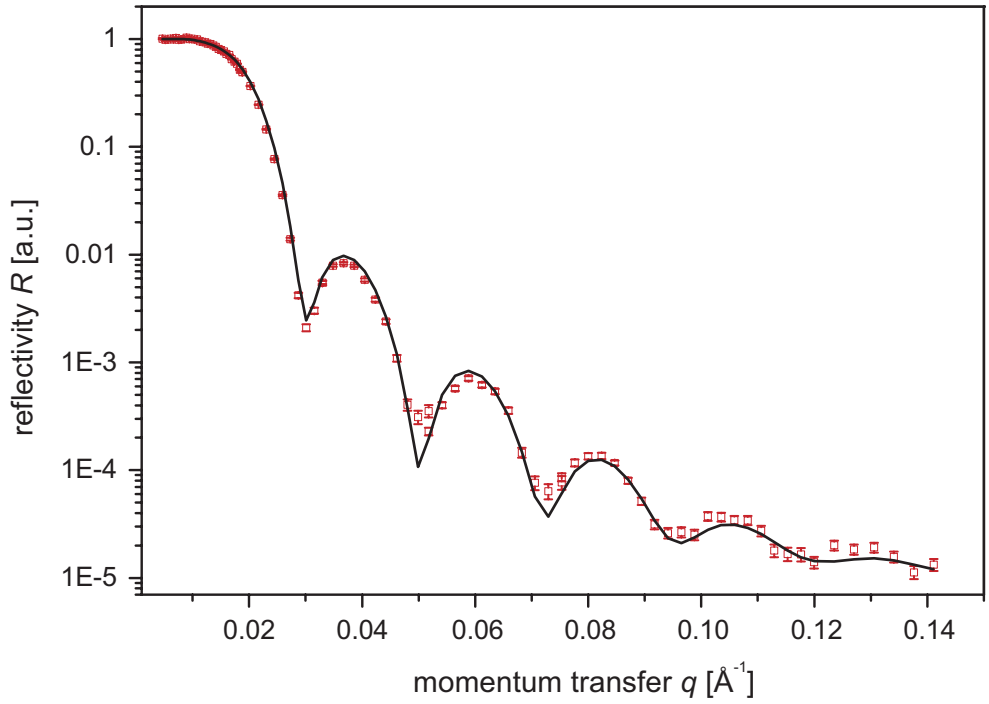

Figure 5.1: NR curve of the dry DB 50 layer with d-PMMA precursor film on silicon versus air. Reflectivity is plotted vs. the momentum transfer q. Red squares represent the measured values and the solid black line shows the best fit.

The neutron reflectometry experiments were all performed at the V6 reflectometer at

the HMI (Berlin, Germany) as described in Section 1.9.2. The scripts used for the scans can be found in Appendix A.6.
Before measuring at the solid/liquid interface, the dry film was characterized by ellipsometry and NR at the solid/air interface to gain reference data for the fitting process in aqueous environment. In Figure 5.1, the reflectivity curve of DB 50 transferred at a lateral pressure of $\pi = 25\text{mN m}^{-1}$ on the d-PMMA precursor film is presented.
The results of the four box model (silicon, d-PMMA, DB 50, air) best fit are summarized in Table 5.1.

layer	d [Å]	sld Nb [10^{-6} Å^{-2}]	σ [Å]
air	-	0	-
DB 50	29	1.40	12
d-PMMA	266	6.79	15
silicon	-	2.07	8

Table 5.1: Results of the four box model best fit. Thickness d, sld Nb and roughness σ are given for each layer using fixed values for Si and air.

These reference data for the roughness of the silicon surface, dry thickness and roughness of the d-PMMA film are used in the later fitting of the DB 50 film at the solid/liquid interface. Figure 5.2 shows the measured reflectivity of a DB 50 layer deposited at a lateral pressure of $\pi = 25\text{mN m}^{-1}$ at two different pH conditions (5.5 and 8.5). The difference in reflected intensities can be clearly distinguished qualitatively as well as quantitatively with a four box (Si, d-PMMA, DB 50, D_2O) model fit. The results of the best fits are shown in Table 5.1.

DB 50	pH = 5.5	pH = 8.5
$d_{\text{d-PMMA}}$ [Å]	279	282
$\sigma_{\text{d-PMMA}}$ [Å]	22	19
$d_{\text{DB 50}}$ [Å]	41	34
$\sigma_{\text{DB 50}}$ [Å]	16	14
$Nb_{\text{DB 50}}$ [10^{-6} Å^{-2}]	3.65	2.95
Nb_{PBS} [10^{-6} Å^{-2}]	5.87	5.97
ϕ_{PBS}	0.55	0.40

Table 5.2: Results of the four box model best fit in aqueous environment. The sld Nb of silicon and d-PMMA were kept fix at the literature values. ϕ_{PBS} denotes the fraction of D_2O in the DB 50 layer.

The thickness of the DB 50 layer at pH = 8.5 is slightly thicker than in the dry state ($d = 34$ Å) and increases significantly ($d = 41$ Å) by changing to pH = 5.5 accompanied by a slight increase in the interface roughness σ from 14 Å to 16 Å. At the same time the sld of the diblock copolymer film changes from $2.95 \cdot 10^{-6}$ Å^{-2} to $3.65 \cdot 10^{-6}$ Å^{-2}.

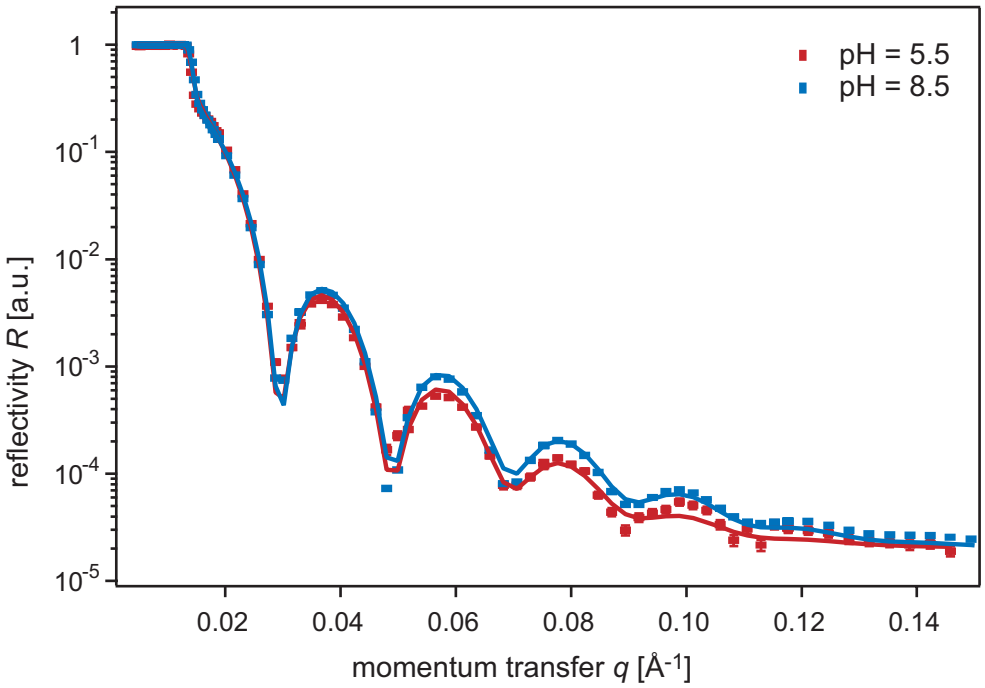

Figure 5.2: Plot of the measured reflectivity of the diblock copolymer at two different subphase pH conditions. Blue dots represent pH 8.5 and red dots pH 5.5. The lines are the best fit for both pH conditions.

An alternative to present the reflectivity data is the Fresnel plot. Here, the reflected intensity is divided by the theoretical reflectivity of the ideal system without any roughness ($\sigma = 0$), that gives the Fresnel reflectivity R_f. With this kind of normalization, smaller changes in the overall reflectivity curve can be better visualized. Figure 5.3 is the Fresnel plot of the data shown in Figure 5.2.
The hydration of the DB 50 film can be directly calculated from its sld. The quantitative measure is the fraction ϕ of D_2O in the polymer film. A swollen film exhibits a sld $Nb_{swollen}$ which is given by the sld of the dry film $Nb_{DB\,50}$, of the subphase $Nb_{subphase}$ and the fraction ϕ of the subphase in the film:

$$Nb_{swollen} = \phi Nb_{DB\,50} + (1 - \phi)Nb_{subphase}. \tag{5.1}$$

Solving this equation for ϕ yields:

$$\phi = \frac{Nb_{swollen} - Nb_{subphase}}{Nb_{DB\,50} - Nb_{subphase}}. \tag{5.2}$$

With the fitted results of the sld for the DB 50 layer for both pH conditions, the fraction of D_2O is determined to be 55 % (ph = 5.5) and 40 % (ph = 8.5). Again, due to the higher hydrophilicity at pH = 5.5 the water uptake is higher than in the uncharged state.

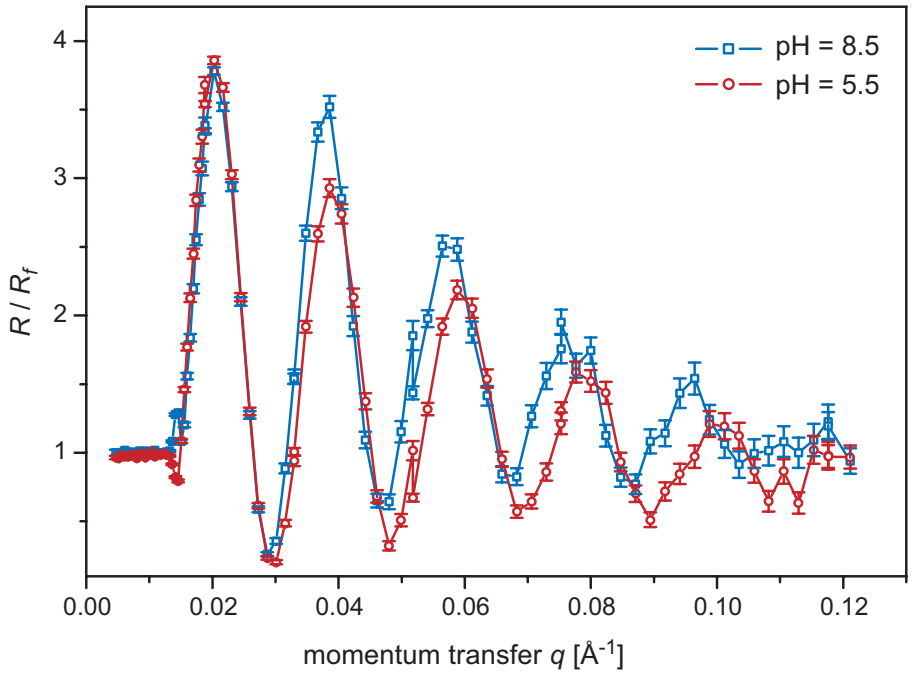

Figure 5.3: Plot of the measured reflectivity normalized by the Fresnel reflectivity of the diblock copolymer at two different subphase pH conditions. Blue squares represent pH 8.5 and red circles pH 5.5. The lines are drawn to guide the eye.

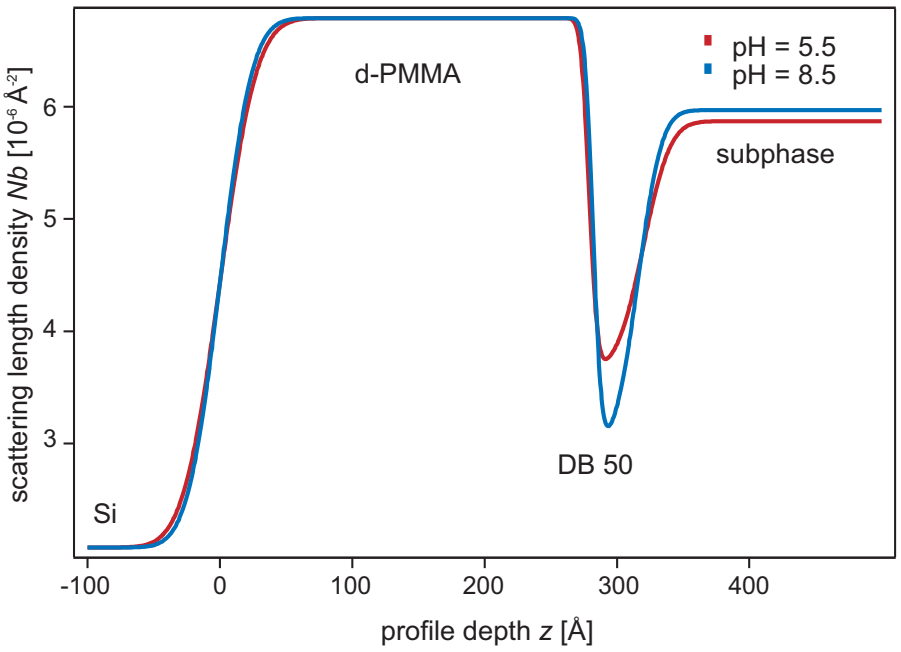

Figure 5.4: Plot of the scattering length density (sld) Nb as a function of the profile depth in z-direction. The blue line represent the fit at pH = 8.5 and the red line at pH = 5.5.

5.2 Protein Adsorption

Adsorption of proteins onto surfaces is of scientific interest in terms of biocompatibility of materials. Bovine serum albumin (BSA) was chosen as model protein because its surface adsorption behavior is extensively studied. Small angle x-ray scattering (SAXS) measurements lead to an assumption of an ellipsoidal shape ($140 \times 40\,\text{Å}^2$) of BSA. In this study, ex-situ adsorption experiments with BSA incubated DB 50 layers were performed by measuring the thickness of the adsorbed layer by ellipsometry and XRR and by fluorescence microscope images with FITC (fluorescence dye) labeled BSA. In-situ experiments were done by measuring neutron reflectometry in the flow chamber at the solid/liquid interface.

5.2.1 Ex-situ Experiments

For the ex-situ protein adsorption experiments, DB 50, films transferred at $25\,\text{mN}\,\text{m}^{-1}$ and $35\,\text{mN}\,\text{m}^{-1}$ were incubated with an aqueous solution of $0.1\,\text{mg}\,\text{ml}^{-1}$ BSA at two different pH conditions (5.5 and 8.5). The samples were measured before and after the incubation with ellipsometry and the layered structure was analyzed in terms of thickness of the adsorbed protein film. These measurements yielded a thickness of a few nm for all samples. Because of the big statistical errors, inhomogeneity and roughness of the system a quantitative evaluation was not possible. However, the thickness of an adsorbed BSA layer in the range of 1 to 4 nm is within the literature values. Qualitatively, the adsorption of BSA was observed at both pH conditions at samples transferred at $25\,\text{mN}\,\text{m}^{-1}$ and $35\,\text{mN}\,\text{m}^{-1}$.

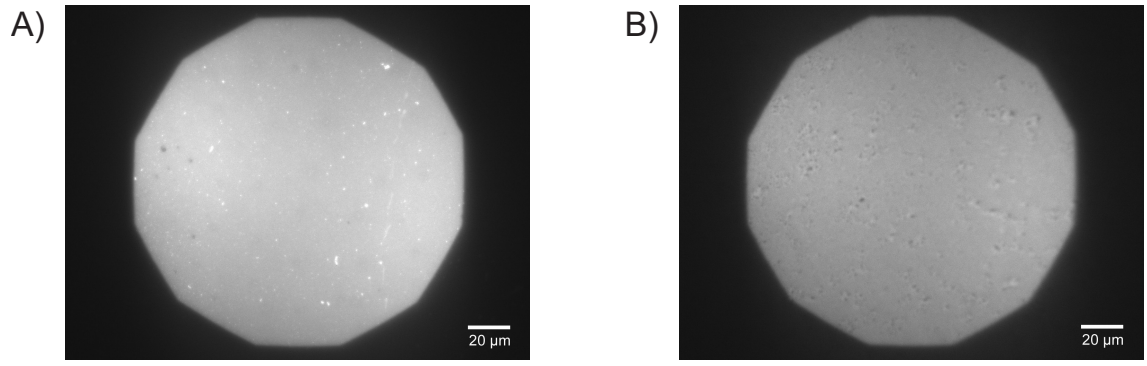

Figure 5.5: Fluorescence images of DB 50 monolayers incubated with FITC-BSA at (A) pH = 5.5 and (B) at pH = 8.5. Both pictures show a homogeneous intensity signal indicating uniform BSA adsorption within the optical resolution.

Another set of adsorption experiments of BSA was done with a fluorescence microscope. Here, a solution of FITC labeled BSA was used for the incubation and glass

cover slides were used instead of silicon substrates. All samples exhibited a fluorescence signal at pH = 5.5 and pH = 8.5 showing uniform adsorption of the protein to the diblock copolymer layer independently from the degree of ionization (i.e. surface charges). In Figure 5.5, two fluorescence microscope images are presented of DB 50 transferred at 25 mN m^{-1} incubated with 0.1 mg ml^{-1} aqueous solution of FITC-BSA at pH = 5.5 (A) and (B) pH = 8.5. There is a small difference in the absolute intensity but this cannot be used as a measure of total adsorbed amount because of the lack of an absolute reference. However, it has been demonstrated that the adsorption of BSA to bare glass slides is pH dependent.

5.2.2 In-situ Experiments

In-situ experiments for protein adsorption were performed using neutron reflectometry at the reflectometer V6 at the HMI (Berlin, Germany). Measurements were carried out with the flow chamber mentioned earlier by injecting a 1 mg ml^{-1} solution of BSA in PBS at pH = 5.5 and pH = 8.5.

Quasi-realtime measurements were done by setting the instrument to a certain angle θ for the sample and 2θ for the detector. The angle will be chosen at a designated minimum or maximum position of the reflectivity curve where the change of intensity due to adsorption was expected to be maximal. With such a setup, it is possible to record the protein adsorption kinetics if the time scale is within the data acquisition time of the respective angle (for the used settings see Appendix A.6).

The measurement scan was started right after injecting the BSA solution. For 1 h data points were taken every 200 s. The intensity varied only within the error range showing no direct signal of protein adsorption over time. However the changes may be small or selection of the momentum transfer q was not appropriate, so another full scan of the reflectivity curve was performed.

Even after the full scan, the reflected intensity before and after incubation with BSA yielded identical signals within the error range showing no significant protein adsorption.

The differences between the fluorescence microscope experiments and the neutron reflectometry scans are based on the resolution of the techniques. A dispersed protein layer of low coverage may yield a homogeneous fluorescence signal, because of the optical resolution being $\gtrsim 1\,\mu$m, but this layer may be invisible for the neutrons because of the small volume fraction and lacking of contrast to the hydrated DB 50 monolayer.

5.3 Lipid Bilayer on Diblock Copolymer

With the well characterized diblock copolymer layer at different pH and grafting conditions, lipid bilayer formation on this polymer support was studied to investigate the interactions of the polymer support with such a model membrane. Since the polymer conformation, degree of hydration, and surface charge density changes upon pH titration, the membrane-substrate interactions are influenced. This allows to tune the forces between the interfaces in-situ by changes of the subphase properties.
A lipid bilayer can be formed with several techniques. In this study, fusion of small unilamellar vesicles was chosen to a complete bilayer on a surface. The small ($d \approx 50\,\mathrm{nm}$) vesicles rupture in the vicinity of the surface due to their high curvature and form a continuous lipid bilayer. Since the melting points T_m of the used lipids SOPC (6.3° C) and SOPG ($\approx 6°$ C) [73, 74, 75] are below the room temperature of ($T_R = 20°$ C), the bilayer is in the fluid L_α phase. This is necessary to have a high diffusivity of the lipids in order to get a complete and homogenous membrane.
Two vesicle solutions were prepared - a pure SOPC vesicle suspension of $1\,\mathrm{mg\,ml^{-1}}$ and a mixed SOPC, SOPG (50 mol% each) suspension. SOPC is a neutral (zwitterionic) lipid and SOPG is negatively charged.

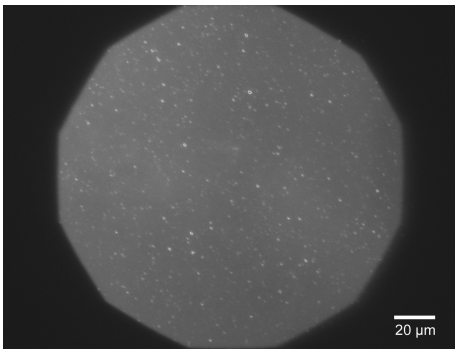

Figure 5.6: Fluorescence image of DB 50 monolayer incubated with the SOPC solution at pH = 5.5. The picture shows a homogeneous intensity signal indicating a homogeneous bilayer at optical resolution. Some bright spots are clusters of the dye due to contamination.

Before measuring the neutron reflectivity of the lipid bilayers on the diblock copolymer, fluorescence microscope experiments were performed to confirm the lipid bilayer spreading. For this, the vesicle suspensions contained addionally 0.5 mol% of NDB-PC, a lipid with a fluorescence dye. As samples, DB 50 monolayers transferred at $15\,\mathrm{mN\,m^{-1}}$, $25\,\mathrm{mN\,m^{-1}}$, and $35\,\mathrm{mN\,m^{-1}}$ onto glass cover slides were used and incubated with the vesicle solutions at pH = 5.5 and pH = 8.5. After 1 hour at 40° C, the supernatant was washed away and fluorescence microscopy images were taken. All samples showed homogenous fluorescence indicating a homogenous bilayer at the scale

of the optical resolution. In Figure 5.6, the microscopy images for DB 50 transferred at 25 mN m^{-1} incubated with the SOPC solution is shown.

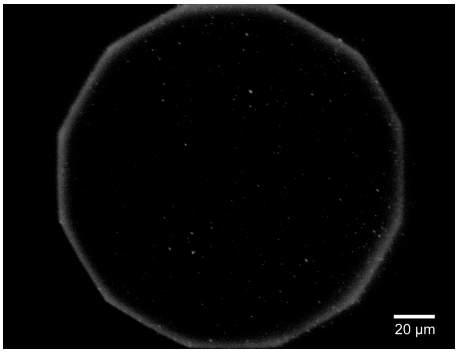

Figure 5.7: Fluorescence image of a SOPC bilayer on DB 50 after 10 min of continuous illumintaion. The corona indicates a fluid bilayer, where unbleached dyes diffuse from the non illuminated area to the illuminated area.

Due to the illumination, the fluorescence dye bleaches and the intensity decreases over time. However, at the edges of the images a stable fluorescence signal remains due to diffusion of dyes from the non illuminated region to the illuminated region. This indicates mobile lipids as expected for the fluid L_α phase. Figure 5.7 shows an image taken after 10 min bleaching the illuminated region with the brighter rim being clearly visible.

After these successful results, the neutron reflectometry experiments were performed to get more information about the polymer-membrane distance. Since the polymer as well as the lipid bilayer are protonated, the deuterated buffer yields a good contrast to the membrane layer.

The first experiment was done with the pure SOPC vesicle solution. Figure 5.8 shows reflectivity curves of the DB 50 film before and after incubation with the SOPC vesicles. In contrast to the fluorescence experiments, no bilayer could be observed, as there was only a very small change detectable by neutron reflectometry. The distances between the minima and maxima were identical and the only difference was a slightly smaller overall intensity, which could be attributed to a minor increase in roughness due to adsorption of a very small amount of vesicles. The measurements showed definitely neither a continuous nor an inhomogeneous bilayer on the polymer film.

In the next experiment, a lipid mixture of SOPC/SOPG (50 mol%/50 mol%) was used to form the bilayer. Here, in contradiction to the pure SOPC solution half of the lipids (SOPG) are charged negatively, which is the opposite charge of the DB 50 layer. After 1 h incubation time, a neutron reflectometry scan was done and the reflected intensity changed drastically indicating changes at the solid/liquid interface.

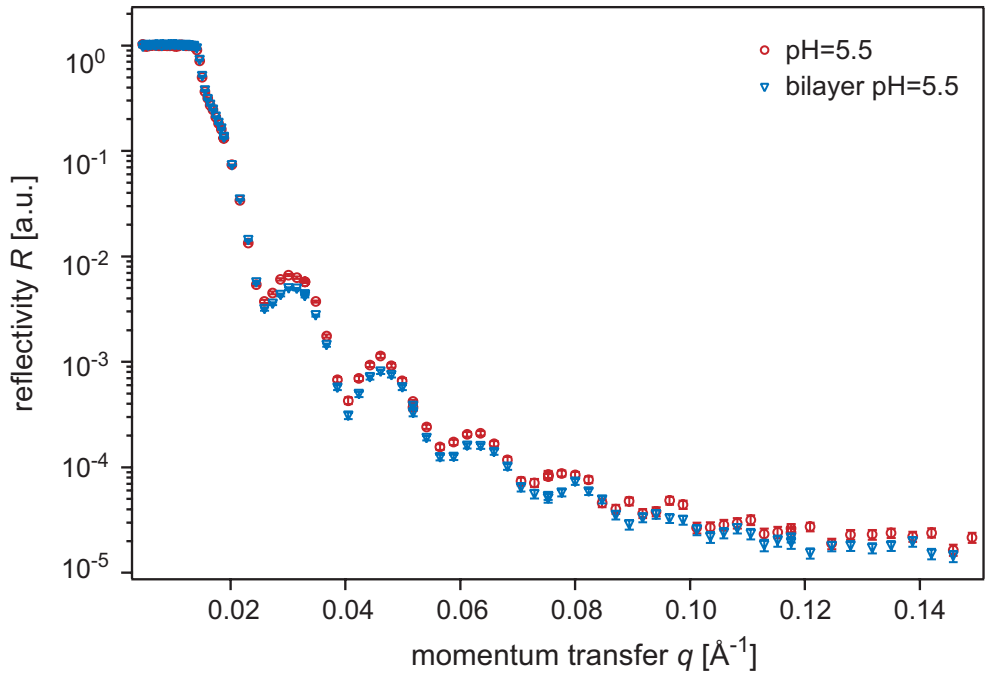

Figure 5.8: Neutron reflectivity curves of the pure DB 50 monolayer at pH = 5.5 (red) and after incubation with SOPC (blue). Both curves are nearly identical within the error range. The slightly smaller intensity for the SOPC incubated system may be due to scattering at contaminants.

Figure 5.9 shows the reflectivity curves before and after incubation with the lipid mixture at pH = 5.5. To fit these data, two more boxes have to be introduced representing the D_2O cleft between the lipid membrane and the diblock copolymer and the lipid membrane itself. As boundary conditions, the scattering length density of the D_2O spacer and the bulk D_2O reservoir are fixed to the same value and as sld for the alkyl chains of the lipid bilayer $Nb = 1 \cdot 10^{-6}$ Å^{-2}, was taken. The detailed results for the best fit are given in Table 5.3.

DB 50 + SOPC/SOPG	pH = 5.5	pH = 8.5
$d_{DB\,50}$ [Å]	37	31
$\sigma_{DB\,50}$ [Å]	14	14
d_{D_2O} [Å]	22	38
σ_{D_2O} [Å]	9	12
$d_{bilayer}$ [Å]	24	31
$\sigma_{bilayer}$ [Å]	14	14

Table 5.3: Results of the six box model best fit after incubation with the SOPG/SOPC mixture at pH=5.5 and 8.5. The sld Nb of silicon and d-PMMA were fixed at the literature values.

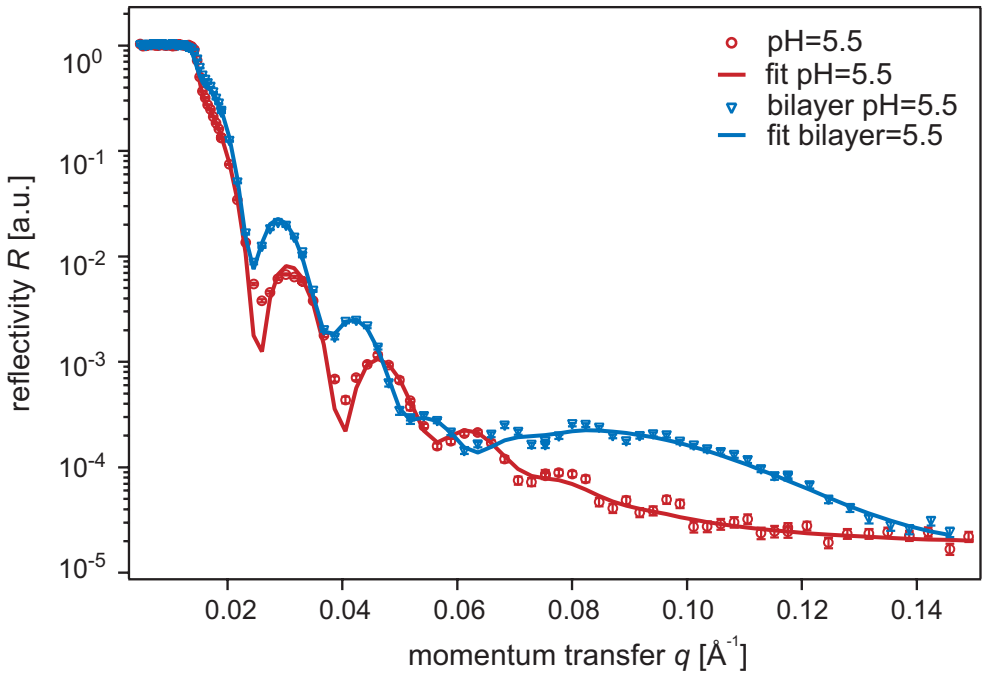

Figure 5.9: Reflectivity curves before (red circles) and after (blue triangles) incubation of the DB 50 film with the lipid mixture. The solid lines represent the best fits.

The scattering length density profile from the fits at pH = 5.5 and pH = 8.5 is displayed in Figure 5.10 together with a sketch of the polymer-supported phospholipid bilayer drawn to scale. Since the headgroups of the phospholipids were not fitted separately approximately 8 Å have to be subtracted from the thickness d_{D_2O} of the water spacer. Obviously, the D_2O spacer distance increases from 14 Å at pH = 5.5 to 30 Å at pH = 8.5. This can be attributed to the drastically lowered surface charge density of the DB 50 layer since the degree of ionization is only 12 % at the higher pH. Therefore, the electrostatic coupling between the negatively charged membrane and the positively charged diblock copolymer monolayer is much weaker and the membrane is not tightly bound to the substrate any longer but goes to an new equilibrium distance at less bound state. The electrostatic interaction could be even stronger in the first case because the two interfaces being oppositely charged counterions can be released [60] which reduces the screening length of the buffer even further. This explains the drastic increase in substrate-membrane distance due to enormously strong electrostatic forces.

In this chapter, successful in-situ monitoring of conformational changes and changes in degree of hydration of a well-defined diblock copolymer layer was demonstrated. By varying the pH in the subphase, the interfacial properties were controlled and determined quantitatively. Although no drastic difference in protein adsorption could

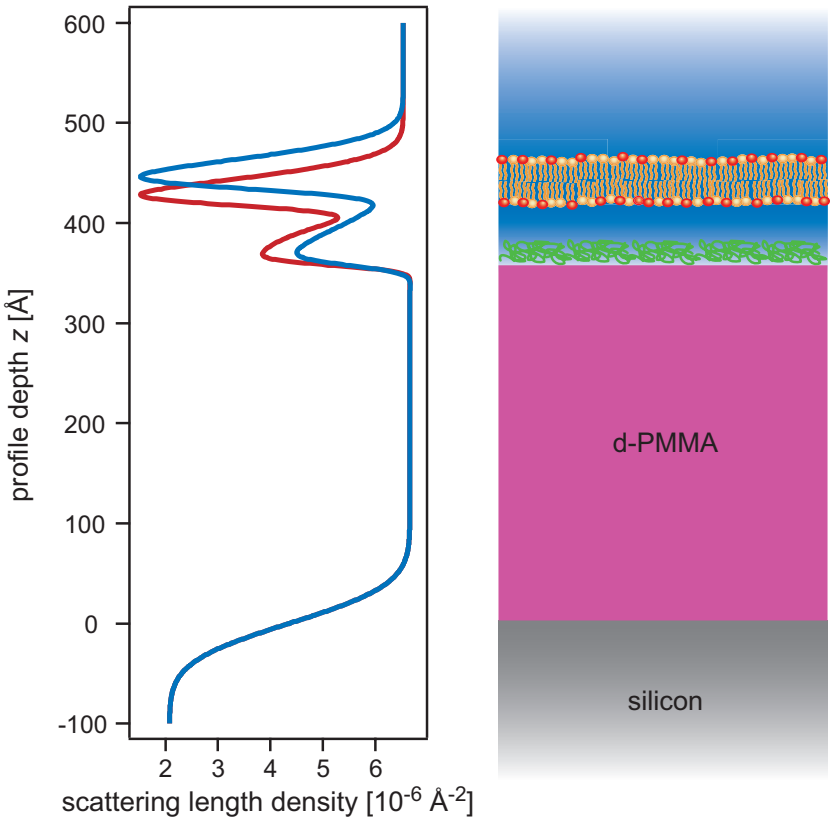

Figure 5.10: Plot of the scattering length density (sld) Nb as a function of the profile depth in z-direction. The blue line represents the fit at pH = 8.5 and the red line at pH = 5.5. On the right side a model sketch of the system drawn to scale is shown. The silicon substrate is coated with the d-PMMA precursor and contrast layer, then with the partially hydrated DB 50 layer on top, and finally with a D_2O spacer the lipid bilayer.

be quantified, the interactions between a supported membrane and the substrate were tuned. Here, for the first time the membrane substrate distance was monitored at two states. A bound state due to strong electrostatic coupling and a nearly unbound state, where the membrane floats on the polymer support. This opens up a wide field for the application of supported membranes especially to investigate membrane bending, undulations and fluctuations as well as a soft polymer interlayer for incorporation of transmembrane proteins.

6. Conclusions

As described in the previous chapters, this study successfully demonstrates the establishment of an ultrathin biomimetic polymer interlayer, whose surface properties can reversibly be altered by external chemical stimuli (pH titration). As a "tunable" polymer material, a new class of diblock copolymer that consists of a weakly cationic DMAEMA block and a hydrophobic MMA block (DMAEMA-*b*-MMA, DB 50) was chosen. In contrast to the other studies, the uniqueness of this work exists in the transfer of an insoluble, Langmuir-type monolayer of the polymer onto a pre-functionalized solid substrate at well-defined polymer chain densities using the Langmuir-Schaefer technique.

In Chapter 4, the chain conformation of the DB 50 was systematically studied at air/water interface under different subphase pH conditions. Pressure-area isotherms (Langmuir isotherms) confirmed the excellent stability of DB 50 monolayers up to a high surface pressure ($\pi > 45\,\mathrm{mN\,m^{-1}}$) at all measured pH conditions, which enables one to achieve a high lateral chain density (up to $300\,\mathrm{Å}^2$ per chain). Furthermore, it was shown that charged polymer chains desorbed from the air/water interface, while uncharged chains tend to adsorb to the interface due to less hydrophilicity. By optimizing the transfer conditions and the precursor layers, the separation of the blocks was successfully enhanced to fabricate stable and uniform films of DB 50 on solid substrates. Prior to the characterization in aqueous environment, the dry films with different lateral chain densities were characterized by combination of different physical techniques, such as contact angle measurements (surface free energy), ellipsometry (total film thickness), and specular x-ray reflectivity (film thickness, surface roughness, and separation of individual layers). Finally, using spin coated PMMA as hydrophobic precursor films the diblock copolymer monolayers were transferred at lateral pressure from $15\,\mathrm{mN\,m^{-1}}$ to $35\,\mathrm{mN\,m^{-1}}$ at pH = 5.5.

In Chapter 5, the chemical switching of transferred DB 50 films was investigated at the solid/liquid interface. The conformational changes of the diblock copolymer due to pH titration was monitored using specular neutron reflectivity measurements. Taking advantage of the big difference in scattering length between hydrogen and deuterium, the experimental system was contrast-optimized using deuterated PMMA, protonated DB 50 and D_2O as subphase. To fit the reflectivity data, this stratified molecular construct was treated by a four-box model (Si, d8-PMMA, DB 50, D_2O).

The global shape of the reflectivity curves exhibited a distinct difference between pH = 8.5 and 5.5, indicating a clear change in thickness, scattering length density (corresponding to the degree of hydration), and roughness of the DB 50 layer. The reflectivity data were perfectly reproducible after several pH cycles, which verified the stability and reversibility of chemical switching. In the charged state (pH = 5.5), the scattering length was higher due to uptake of D_2O. Together with the thickness and roughness increase, this showed clear evidences for the conformational switching from a "collapsed", less hydrophilic state to a more hydrophilic polymer "brush" regime as already depicted in Figure 2. Here, the experimental findings at the air/water interface were reproduced at the solid/liquid interface.

In Section 5.2 interactions of the DB 50 film with water soluble proteins were investigated with in-situ and ex-situ methods. With a special alignment of the neutron reflectometer, quasi-real time measurements were performed with a resolution of 2 min. Although the quantitative analysis of BSA adsoprtion at different pH conditions was not possible, the fluorescence microscope experiments showed homogeneous protein adsorption at both conditions.

In the last section (5.3) the interactions with a model membrane was studied. Fluorescence microscope images of bilayers formed with vesicle fusion yielded a homogeneous and fluid phospholipid membrane supported by the DB 50 film. With the help of neutron reflectometry it was possible to determine the separation of this membrane and the supporting polymer. A mixture of 50% charged and 50% neutral lipids (SOPG, SOPC) exhibited a distinct change from 15 Å at pH = 5.5 to 30 Å at pH = 8.5. Since the surface charge density is dependent on the subphase pH, the electrostatic coupling between DB 50 and lipid bilayer was changed from a strongly bound state at pH = 5.5 to an nearly unbound state at pH = 8.5, where the potential is too small to overcome the electrolyte screening.

The results of this study demonstrate the successful establishment of ultrathin polymer films as biomimetic interfaces, which surface properties can be altered by external stimuli. With the well-defined control of polymer conformation, degree of hydration, and surface charges, interactions between a phospholipid bilayer as model membrane could be tuned. Such supported bilayers are an enhancement and progress towards the study of proteins in their native state. Even more, interactions between more complex cell models (lipid membrane including transmebrane proteins, glycolipids) and a DB 50 functionalized planar substrate can be studied.

7. Outlook

The experiments in Chapter 5 showed the large potential of neutron reflectometry to study stratified biomimetic interfaces in an aqueous medium. The changes in degree of hydration, thickness, and surface roughness of a layer of only 4 nm could be determined quantitatively. Especially the huge difference in the scattering lengths of hydrogen and deuterium, gives rise to this sensitivity. By synthesizing different, partially deuterated diblock copolymer or deuterated proteins and lipids, this feature can be exploited even further. With such optimized systems, the kinetics of adsorption, diffusion, and even binding/unbinding processes could be investigated. For this purpose, other isotopes like Fe, Ni, and Cr can be used as well.
Another promising strategy is to use the DB 50 film as support for model membranes. There is a huge interest in studying membranes as artificial cell models on planar supports. To date, many experiments using x-ray and neutron reflectometry have been performed using the bare silicon substrate as solid support [76, 77, 78, 79, 80, 81, 82]. This strategy has major drawbacks, because the substrate-membrane interaction can not be changed or even controlled and the bilayer will be strongly dissipated due to the boundary conditions. New approaches use two lipid bilayers treating the upper one as a free floating bilayer [83]. This reduces the influence of the substrate but still prohibits the modification of the surface properties. This thesis showed the first successful demonstration, to use a thin polymer film as switchable, soft, biomimetic interlayer for proliferation of a membrane. The possibility to change the substrate membrane interactions and hence, the distance allows for incorporation of large transmembrane proteins without stress in the lipid bilayer. This yields a great potential towards the study of proteins in their native state, as well as for the study of membrane fluctuations and undulations. Especially off-specular neutron scattering is ideally suited for these experiments since they work label-free and non-destructive (radiation damage) [81, 84]. With the experimental system established in this thesis and the developments in instrumentation, like the novel reflectometer/small angle scattering instrument (REFSANS) at FRM 2 (Munich, Germany) [85, 86, 87], many open questions about membrane elasticity and the influence of proteins or lipid compositions, will be answered, studying the off-specular information.

A. Appendix

A.1 Phase Behavior of Glycolipids

In Chapters 4 & 5, the importance and the successful in-situ tuning of surface properties was demonstrated. But one can also approach the mediation, understanding and control of the interactions between solid substrates and biological matters like membranes, proteins, and cells from the opposite side, namely the biological matter side, the cell surface. Its major component is the glycocalix which covers the extracellular side of the lipid plasma membrane. Glycolipids are a very important part of the glycocalix, together with glycoproteins and other sugar components they play a vital role in cell-cell recognition, cell proliferation and mediating cell communication as well as avoiding the unspecific sticking of cells. In order to understand this complex behavior it is necessary to study simpler model systems. Here, the hydration of lamellar stacks of pure synthetic glycolipids at different temperatures and relative humidity conditions was investigated with neutron scattering.

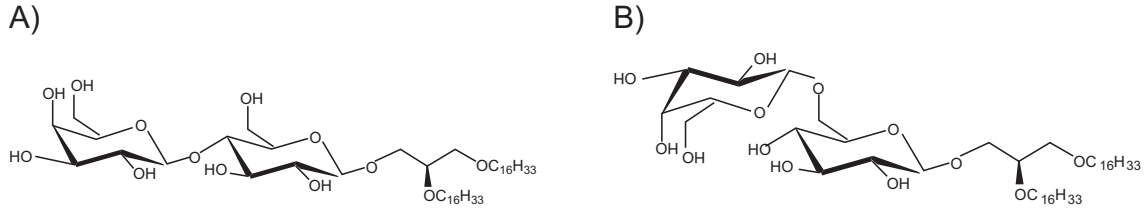

Figure A.1: Chemical structures of A) lactose 1 lipid (Lac 1) and B) gentiobiose lipid (Gent).

The artificial glycolipid molecules used in this study were synthesized by C. Gege et al. at the University of Konstanz as described elsewhere [88, 89]. The chemical structures of the lactose 1 lipid (Lac 1) and the gentiobiose lipid (Gent) are shown in Figure A.1. The headgroup of Lac 1 consists of two linearly linked glucose molecules, whereas the gentiobiose lipid has two glucose units which are 1,6 β-linked yielding a bent sugar headgroup. The two alkyl chains, each consisting of 16 carbon atoms, are linked by a glycerol junction.

A.1.1 Morphology in Bulk Dispersions

The bulk morphology of the synthetic glycolipids (Lac-1 and Gent) were studied with simultaneous SAXS and WAXS measurements at the beamline A2 at HASYLAB. The x-ray diffraction patterns of glycolipid dispersions in water in sealed quartz capillaries (Hilgenberg GmbH, Marsfeld, Germany) were recorded at different temperatures. Within the small angle region, peaks indicating the lamellar distance were found,

whereas the chain-chain correlation peaks appear in the wide angle region. Measurements of different lactose lipids have been reported already by Schneider et al. [90]. There, the melting temperature of the phase transition from the crystalline like L_C phase to the fluid L_α phase was found to be $T_m = 74°\,\mathrm{C}$ with an enthalpy of $H = 30\,\mathrm{kcal\,mol^{-1}}$.

The same measurement was performed with the dispersion of Gent. Figure A.2 shows the obtained diffraction patterns for $T = 30°$ C and $T = 80°$ C. The SAXS peak indicates a lamellar phase which characteristic distance changes. At $T = 30°$ C, a clear WAXS peak was visible due to the correlation of the alkyl chains indicating the L_β gel phase. The phase transition was observed at $T_m = 55°$ C.

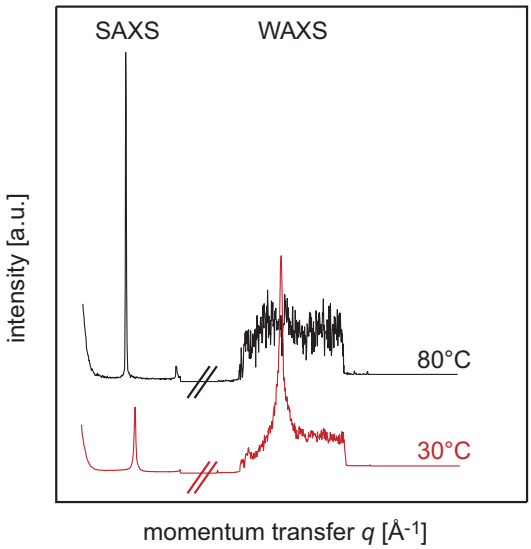

Figure A.2: SAXS and WAXS diffraction pattern of an aqueous dispersion of gentiobiose lipid. The WAXS peak disappears above 55° C due to the chain melting. The SAXS peak position determines the lamellar spacing.

The SAXS and WAXS results were confirmed by differential scanning calorimetry (DSC) measurements yielding the same phase transition temperatures.

A.1.2 Swelling of Lamellar Stacks of Glycolipids

In the fluid L_α phase, swelling experiments of lamellar stacks of glycolipids have been performed by varying the relative humidity. Samples were prepared by solvent casting of gentiobiose lipid in a mixture of $CHCl_3$ and methanol onto silicon substrates. After evaporation of the solvent, the stacks were hydrated at 99% relative humidity at 80°C. The lamellar distance was measured with SANS in a humidity chamber at the beamline D16 at the ILL (Grenoble, France).

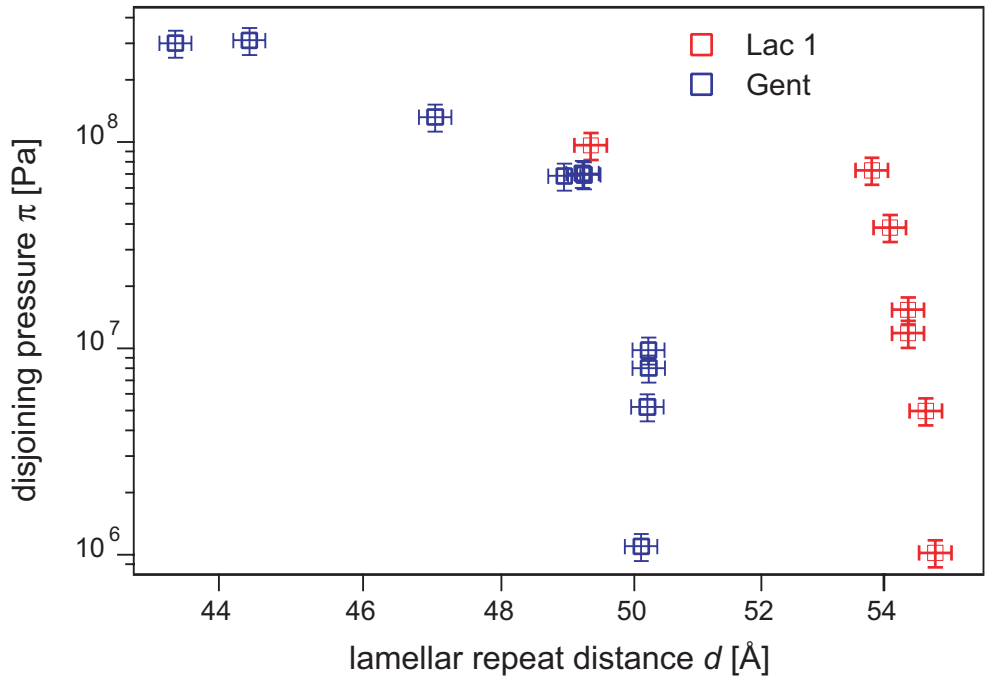

Figure A.3: Force-distance relation for Lac-1 and Gent. Swelling of the lamellar stacks were observed till the hydration limit is reached.

Figure A.3 shows the disjoining pressure vs. the thickness of the headgroup region for Lac-1 and Gent. This force-distance relation shows a swelling of the lamellar glycolipid stacks until the hydration limit is reached. From this data, a quantitative analysis of the mechanical properties is possible. The results of this synthetic glycolipid lamellae are the first step towards the understanding of the complex interplays of the glycocalix and extracellular matrix.

A.1.3 Phase Diagram of Gentiobiose Lipid

Measurements at different temperatures and relative humidity conditions were performed to get information of the phase behavior of the Gent lamellar system. Figure A.4 shows three different scans at $T = 30°$ C, 55° C, and 80° C at $\approx 98\,\%$ relative humidity. The phase transition was clearly visible as well as the coexistence of both phases at 55° C.

With the results of all performed scans, a phase diagram can be drawn as shown in Figure A.5. Here, the blue area represents the fluid L_α phase, the red area the L_β gel phase and the coexistence region is colored purple. Interestingly, the phase transitions were not only induced by the temperatures but also by the relative humidity. This can be attributed to a mechanically induced phase transition due to changes of the disjoining pressure of the system.

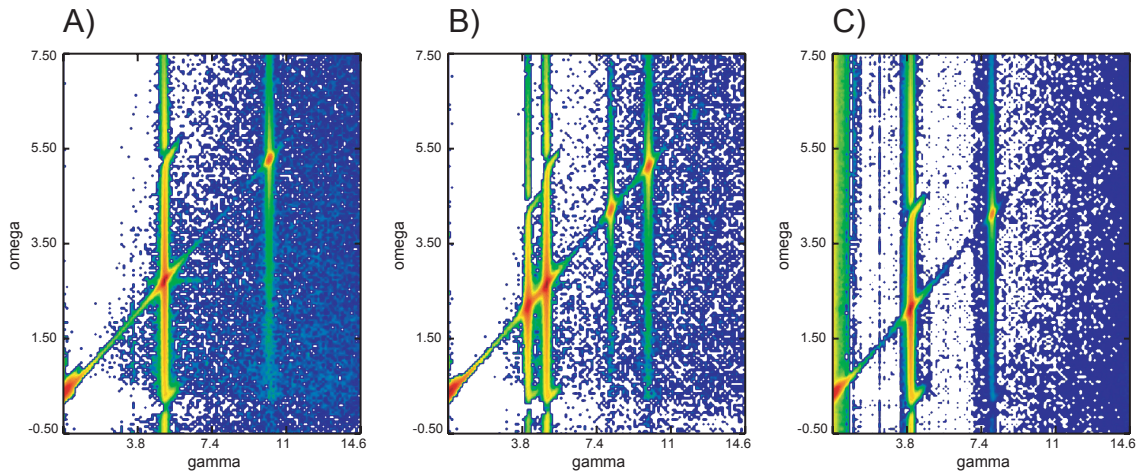

Figure A.4: Diffraction pattern of gentiobiose lipid at high relative humidity ($X \approx 95\,\%$) at 30° C (A), 55° C (B) and 80° C (C). At 55° C and 80° C first and second order Bragg peak can be seen from the monophase, at 55° C the phase coexistence is visible with first and second order Bragg peaks of both lamellar distances.

Summarizing these preliminary results, it was successfully demonstrated that the phase behavior of synthetic glycolipids could be examined by SANS at lamellar stacks. The phase transition was observed by changing the temperature as well as the disjoining pressure at a constant temperature. This gives more insight to the interplay of the forces acting in the glycocalix and yields valuable information for the design of more complex artificial cell models. To investigate the lamellar stacks further, a detailed analysis of the out-of-plane scattering has to be done. With this diffuse scattering information, the bending and undulations of bilayers can be studied quantitatively.

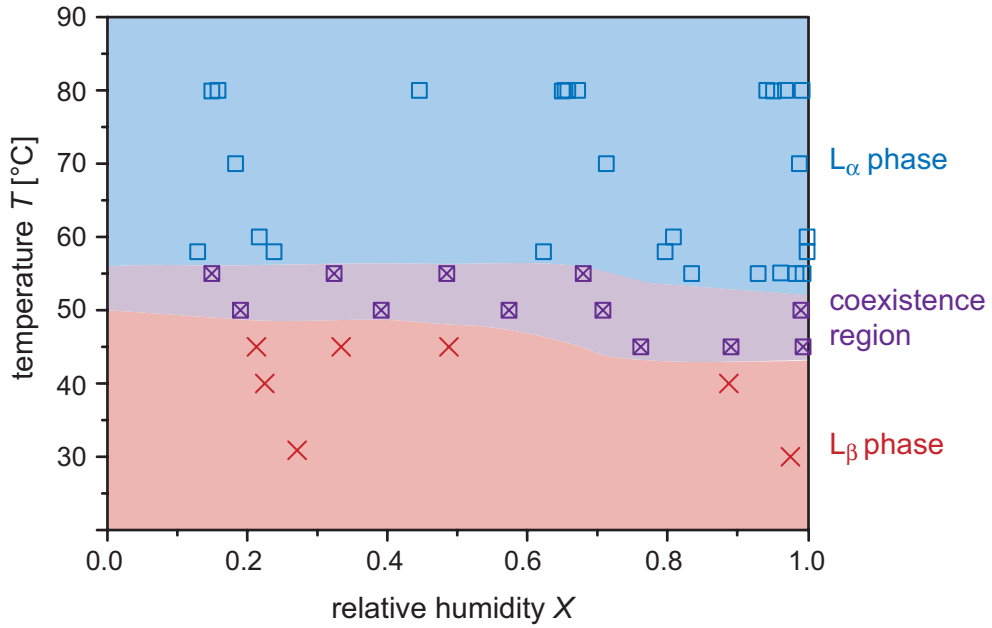

Figure A.5: Phase diagram of lamellar stacks of gentiobiose lipid. Measurement points of the fluid L_α phase are blue squares, L_β phase is indicated by red crosses and the coexistence region is depicted with purple crossed squares. Around the coexistence region the phase transition due to relative humidity or temperature can be observed.

A.2 Ultrathin Cellulose Films on Silicon Substrates

Ultrathin films of cellulose on silicon substrates were prepared by the Langmuir-Blodgett (LB) and the spin coating (SC) technique. The hydration properties were characterized quantitatively by ellipsometry under well-defined humidity conditions and analyzed in terms of force-distance relationships. Finally, micro-structured cellulose films were prepared by UV lithography and the three dimensional height profiles were examined by imaging ellipsometry [22].

F. Rehfeldt and M. Tanaka: "Hydration forces in ultrathin films of cellulose", *Langmuir* **19** (2003), p. 1467-1473.

Langmuir **2003,** *19,* 1467−1473

Hydration Forces in Ultrathin Films of Cellulose†

Florian Rehfeldt and Motomu Tanaka*

Lehrstuhl für Biophysik, Technische Universität München, James-Franck-Strasse, 85748 Garching, Germany

Received July 1, 2002. In Final Form: October 7, 2002

Ultrathin (d < 20 nm) films of cellulose were fabricated by regeneration of trimethylsilylcellulose films, which were deposited on silicon wafers by the Langmuir−Blodgett (LB) or the spin-coating method. Equilibrium film thickness with respect to relative atmospheric humidity was quantitatively measured by ellipsometry to obtain relationships between thickness and osmotic pressures within the hydrated films (force−distance curves). The hydration of cellulose LB films and that of spin-coated films under equilibrium were found to be independent from initial dry film thickness and surprisingly similar in terms of (a) maximum swelling ratio ($\rho_{max} \sim 1.6$), (b) power law exponent under high-pressure conditions ($>5 \times 10^7$ Pa), and (c) exponential decay length ($\lambda_0 = 0.32$ Å) under low-pressure conditions ($<5 \times 10^7$ Pa). Fast water uptake kinetics across an abrupt change of the relative humidity (osmotic shock) was monitored as changes in film thickness with time, yielding a characteristic time constant of $\tau = 14$ s. Furthermore, microstructures of cellulose films were processed through deep UV photolithography, and their local three-dimensional profiles could be obtained by imaging ellipsometry. Selective immobilization of native cell membranes onto such patterns will enable us to design biocompatible microtemplates to accumulate native cell membranes on solid surfaces.

Introduction

Cells utilize various types of carbohydrate complexes to communicate with their environments. The cell surface glycocalix and extracellular matrix (ECM) include a variety of poly(oligo)saccharides that have different interactions with the surrounding water.[1,2] They can maintain high local disjoining pressures, generate hydrated "cushions" between cells and tissues, and control the metabolism. In nature, such "wetting affinities" are fine-tuned by complex interplays of physical forces at interfaces,[3] which control cell−cell and cell−tissue interactions.[4] For example, at repulsive disjoining pressures, the membranes can keep a certain distance via hydrated cushions of glycocalix and ECM. However, strong "dewetting" (i.e., adhesion) can take place when the interfacial attraction becomes dominant.[5,6] Indeed, more recent studies have demonstrated that the phase separation induced by strong adhesion can even be interpreted as a first-order wetting/dewetting transition.[7,8] To apply such a "wetting principle" to real cells, better-defined models of cell and tissue surfaces are required. Several synthetic polymers are also claimed to be possible candidates for the artificial glycocalix models. To date, grafted films of dextran[9] and poly(ethylene glycol) (PEG) brushes[10] could achieve a sufficient resistance against nonspecific adsorption of proteins, which have been used in numerous fields.

Cellulose is not only the main constituent of cell walls of woody plants but also one of the most important renewable resources in the chemical industry.[11] Cellulose consists of a linear chain of glucose, and strong hydrogen bonding between these linear polysaccharides results in crystalline-like fiber structures. For the design of advanced materials, synthetic modification of cellulose has been conducted to introduce various functionalities.[12] Substitution of some hydroxyl protons causes drastic changes in the physical properties. In fact, silylated cellulose derivatives are often soluble in nonpolar solvents due to the significant reduction in the intermolecular hydrogen bonding.[13,14] For example, Wegner and co-workers[15,16] demonstrated that Langmuir monolayers of trimethylsilylcellulose (TMSC) could be transferred onto a hydrophobized substrate by the Langmuir−Blodgett (LB) method. Moreover, exposure to HCl regenerated TMSC to pure cellulose without disturbing the film morphology.

In our previous studies, we demonstrated that LB films of regenerated cellulose with thicknesses of 5−10 nm could serve as ideal interlayers to deposit model and native cell membranes. For example, we deposited an artificial lipid bilayer onto indium−tin oxide (ITO) electrodes coated with a cellulose LB film.[17] After the bilayer was spread, electric resistance of the membrane increased up to 0.5 MΩ cm^2,

* Corresponding author. Tel: ++49-89-289-12539. Fax: ++49-89-28912469. E-mail: mtanaka@ph.tum.de.

† Part of the *Langmuir* special issue entitled The Biomolecular Interface.

(1) Gabius, H. J.; Gabius, S. *Glycoscience*; Chapmann & Hall: Weinheim, 1997.
(2) Comper, W. D. *Extracellular Matrix*; Harwood Academic: Amsterdam, 1996.
(3) Israelachvili, J. N. *Intermolecular and Surface Forces*, 2nd ed.; Academic Press: London, 1992.
(4) Sackmann, E.; Tanaka, M. *Trends Biotechnol.* **2000**, *18*, 58.
(5) Parsegian, V. A.; Fuller, N.; Rand, P. *Proc. Natl. Acad. Sci. U.S.A.* **1979**, *76*, 2750.
(6) Elender, G.; Sackmann, E. *J. Phys. II France* **1994**, *4*, 455.
(7) Bruinsma, R.; Behrisch, A.; Sackmann, E. *Phys. Rev. E* **2000**, *61*, 4253.
(8) Sackmann, E.; Bruinsma, R. F. *ChemPhysChem* **2002**, *3*, 262.
(9) Löfas, S.; Johnson, B. *J. Chem. Soc., Chem. Commun.* **1990**, *21*, 1526.
(10) Harris, J. M. *Poly(ethyleneglycol) Chemistry*; Plenum Press: New York, 1992.
(11) Kennedy, J. F.; Phillips, G. O.; Williams, P. A.; Piculell, L. *Cellulose and cellulose derivatives: Physicochemical aspects and industrial applications*; Woodhead Publishing: Cambridge, 1995.
(12) Klemm, D.; Heinze, T.; Philipp, B.; Wagenknecht, W. *Acta Polym.* **1997**, *48*, 277.
(13) Klebe, J. F.; Finkbeiner, H. L. *J. Polym. Sci. A* **1969**, *7*, 1947.
(14) Klemm, A.; Stein, A. *J. Macromol. Sci., Pure Appl. Chem.* **1995**, *A32*, 899.
(15) Schaub, M.; Wenz, G.; Wegner, G.; Stein, A.; Klemm, D. *Adv. Mater.* **1993**, *5*, 919.
(16) Buchholz, V.; Wegner, G.; Stemme, S.; Ödberg, L. *Adv. Mater.* **1996**, *8*, 399.
(17) Hillebrandt, H.; Wiegand, G.; Tanaka, M.; Sackmann, E. *Langmuir* **1999**, *15*, 8451.

10.1021/la0261702 CCC: $25.00
Published on Web 11/23/2002

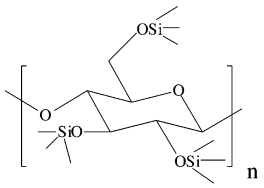

Figure 1. Structure of trimethylsilylcellulose (TMSC). The average degree of substitution (DS) per glucose unit was determined by elemental analysis: DS ~ 2.1.

which was by a factor of 5 larger than that obtained for the lipid bilayer directly deposited on ITO.[18] Indeed, the lipid bilayer could diffuse over the cellulose film and healed their local defects, observed by microinterferometry.[17] Recently, we reported the homogeneous and orientation selective immobilization of human erythrocyte membranes on cellulose LB films.[19] The selective fluorescence labeling of cytoplasmic and extracellular domains confirmed that the immobilized erythrocyte membranes selectively inverted their native (asymmetric) orientation, exposing their cytoplasmic side to bulk electrolytes. No adsorption or rupture could be seen when the erythrocytes were incubated with bare glass slides. When the glass slides were coated with polylysine films, patches of the ruptured membranes could be observed; however, the surface coverage still remained poor even after prolonged incubation. This can be attributed to a strong electrostatic attraction between a strong polycation (polylysine) and a weak polyanion (cell surface glycocalix with sialic acid residues).[20,21] On the contrary, a large surface coverage observed on cellulose suggested that the osmotic pressures among the cell surface glycocalix and those among polysaccharides with a neutral net charge (cellulose) could be similar, and therefore, the cell membrane can "wet" cellulose surfaces homogeneously.

In this study, we prepared ultrathin (thickness < 20 nm) cellulose films by means of LB deposition and the spin-coating method. Relationships between thickness and osmotic pressures within the hydrated films were quantitatively studied by measuring equilibrium film thickness as a function of relative atmospheric humidity. As a noninvasive technique with a high thickness resolution (±0.1 Å), ellipsometry coupled to a climate chamber was used to determine film thickness. The fast kinetics of the water uptake was analyzed by plotting film thickness as a function of time across an abrupt change of the relative humidity (osmotic shock). Moreover, spin-coated films of cellulose were microstructured by photolithography. Three-dimensional structural profiles of the microstructured film could be reconstructed from Ψ and Δ maps obtained by imaging ellipsometry. Details of the results will be discussed in the following sections.

Experimental Section

Materials. Octadecyltrimethoxysilane (ODTMS) was purchased from ABCR (Karlsruhe, Germany). TMSC (Figure 1) was synthesized from cellulose powder (MW ~ 25 000, purchased from Fluka), as previously reported.[15] The average degree of substitution (DS) was estimated by elemental analysis: DS ~ 2.1. All other chemicals were purchased from Fluka (Neu Ulm, Germany) and were used without further purification.

Substrates. One-side polished, p-type boron-doped silicon [100] wafers with a thermal oxide layer of about $d = 147 \pm 5$ nm were donated by Wacker Siltronic (Burghausen, Germany). Each wafer was cut into rectangular pieces (10 × 25 mm) for the LB deposition and into square pieces (24 × 24 mm) for the spin coating, respectively. The substrates were cleaned with acetone and methanol and immersed into a solution of 1:1:5 (v/v) H_2O_2 (30%)/NH_4OH (30%)/H_2O for 5 min under sonication.[22] They were soaked for another 30 min at 60 °C and rinsed intensively with water (Millipore, Molsheim, France; $R > 18$ MΩ cm^{-1}, pH = 5.5). Subsequently, the cleaned wafers were dried at 70 °C for 1 h and stored overnight in a vacuum chamber. These surface pretreatments resulted in a very hydrophilic surface, where the contact angle to a water droplet measured in an ambient atmosphere was almost zero.[23]

LB Deposition of Cellulose Films. Prior to LB deposition, self-assembled monolayers of ODTMS were grafted onto freshly cleaned wafers to render the surface hydrophobic.[23,24] Monolayer-coated surfaces became hydrophobic, showing a water contact angle of more than 95°. A chloroform solution of TMSC (concentration ~ 0.7 mg/mL) was spread on a water subphase of a self-built Langmuir trough (subphase area, 982 cm^2) at 20 °C. The monolayer was compressed to a lateral pressure of 30 mN m^{-1} (barrier speed, 100 μm s^{-1}) and transferred onto the hydrophobized substrate. Following successive deposition of monolayers, the film was dried at 70 °C for 1 h and stored overnight in a vacuum chamber. Hydrophobic trimethylsilyl side chains were cleaved by exposing the hydrophobic TMSC multilayer (water contact angle > 70°) to fuming HCl for 20 s, resulting in a regenerated cellulose film.[15,16] After regeneration, the film was rinsed intensively with water and kept in a vacuum chamber. The regenerated cellulose film is hydrophilic (water contact angle ~ 35°) and stable against water and most organic solvents.

Spin Coating of Cellulose Films. For spin coating, the concentration of TMSC in chloroform was varied within 1−8 mg/mL to control the film thickness. Undissolved, clustered TMSC was removed by centrifugation. The coating was carried out with a Delta 10 spin coater (B.L.E. Laboratory Equipment GmbH, Singen, Germany). TMSC solution (200 μL) was deposited onto a square (24 × 24 mm) wafer, and the substrate was rotated first for 10 s at 1000 rpm and for 90 s at 5000 rpm. After spin coating, the TMSC film was dried at 70 °C and stored in a vacuum chamber. The regeneration was according to the manner as described above.

Microstructure Processing. After preparation of homogeneous cellulose films, microstructures were processed by ultraviolet (UV) photolithography.[24,25] Cu electron microscope (EM) grids (SCI Science Services, Munich, Germany) were used as photomasks. An EM grid was fixed onto the cellulose surface with a drop of chloroform, and the sample was illuminated for 30 min with a 500 W mercury arc lamp (L.O.T. Oriel, Darmstadt, Germany), using a thermal filter of fused silica (thickness, 6 mm; Melles Griot, Bensheim, Germany). The illumination time was carefully optimized by checking the height difference quantitatively with ellipsometry.

Hydration of Cellulose under Equilibrium. Equilibrium thickness of cellulose films under different osmotic pressures was measured at room temperature (293 K) by a conventional PCSA (polarizer−compensator−sample−analyzer) ellipsometer (Plasmos GmbH Prozesstechnik, München, Germany). All the measurements were carried out at a constant wavelength (λ = 632.8 nm) and at a fixed angle of incidence (70°). Deviations in the initial dry thickness were within the range of ±2 Å among three independent measurement points, verifying the data reproducibility and macroscopic homogeneity of each film. The relative humidity inside the climate chamber could precisely be controlled between 4% and 98%. Furthermore, our experimental system is kept below the condensation limit; therefore, the system is free from bulk water. The film was allowed to equilibrate for

(18) Gritsch, S.; Nollert, P.; Jähnig, F.; Sackmann, E. *Langmuir* **1998**, *14*, 3118.
(19) Tanaka, M.; Kaufmann, S.; Nissen, J.; Hochrein, M. *Phys. Chem. Chem. Phys.* **2001**, *3*, 4091.
(20) Jacobson, B. S.; Branton, D. *Science* **1976**, *195*, 302.
(21) Thomas, N. E.; Coakley, W. T.; Winters, C. *Colloids Surf., B* **1996**, *6*, 139.
(22) Kern, W.; Puotinen, D. A. *RCA Rev.* **1970**, *31*, 187.
(23) Hillebrandt, H.; Tanaka, M. *J. Phys. Chem. B* **2001**, *105*, 4270.
(24) Mooney, J. F.; Hunt, A. J.; McIntosh, J. R.; Liberko, C. A.; Walba, D. M.; Rogers, C. T. *Proc. Natl. Acad. Sci. U.S.A.* **1996**, *93*, 12287.
(25) Dulcey, C. S.; J. H., G.; Krauthamer, V.; Stenger, D. A.; FAre, T. L.; Calvert, J. M. *Science* **1991**, *252*, 551.

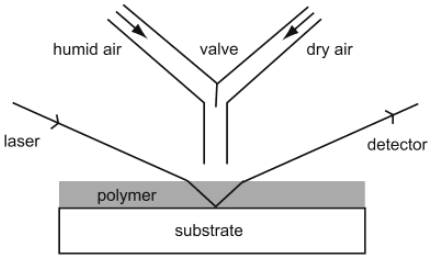

Figure 2. Schematic drawing of dynamic swelling measurements. A pipet tube in the vicinity of the measurement point (~1 mm^2) can switch the atmosphere between dry (~4%) and humid (~94%) conditions. Changes in film thickness with time were monitored using ellipsometry.

about 10 min between two subsequent measurements. From the measured ellipsometric parameters, Ψ and Δ, the thickness of the film can be calculated according to Fresnel equations[26,27] using ideal layer models. Changes in the refractive index of polymer films due to hydration were calculated with Garnet's formula.[28,29] The complex refractive indices were assumed, $n = 3.868 - i0.024$ for bulk silicon,[27] $n = 1$ for air (independent from the relative humidity), and $n = 1.46$ for silicon dioxide.[30] The initial "dry" thickness was determined at a relative humidity of around 4%, by assuming the refractive index of the dry film to be $n = 1.505$.[16] Details of the setup and the data analysis were reported elsewhere.[6,31,32]

As the sum of forces operating within the film (disjoining pressure) is in equilibrium with the osmotic pressure in the climate chamber,[5,33,34] it can be represented by

$$p = -\left(\frac{RT}{V_m}\right)\ln\left(\frac{p_w}{p_0}\right) = -\left(\frac{RT}{V_m}\right)\ln(X) \qquad (1)$$

where V_m is the molar volume of water, and T is temperature. R stands for the gas constant, while X is the relative humidity inside the chamber, which is equal to the ratio between the actual vapor pressure p_w and the saturation pressure of water in the surrounding atmosphere p_0.[35,36] Thus, one can obtain quantitative force−distance relationships by plotting the measured film thickness versus disjoining pressure.

Kinetics of Hydration under "Osmotic Shocks". To switch the atmospheric humidity in the proximity of the measurement point more abruptly, we used a pipet for supplying a constant flow of air (flow rate, 10 L/min) to the sample (Figure 2). Ellipsometric data were collected every 1.7 s across the applied osmotic shocks. The film was first kept for 10 min in a dry atmosphere (relative humidity ~ 4%), and an osmotic shock (i.e., fast switching to high humidity, ~94%) was applied. In the same manner, the dynamics of water exclusion was measured against an "inverse" osmotic shock, switching the humidity back from humid to a dry atmosphere. The kinetics of swelling and draining of the film was analyzed by plotting film thickness versus time. As the initial film thickness (5−10 nm) and its change due to swelling (2−5 nm) were much smaller than the wavelength (632.8 nm), we approximated a linear relationship between arbitral (by assuming a constant n) and real (calculated from n corrected by the Garnet equation) film thickness,[26,27] instead of calculating all the thickness values self-consistently.[31,32] Indeed, five different data points randomly chosen out of one series of experiments yielded the correlation coefficient of $\sigma = 0.999\,95$ (data not shown), confirming the validity of the approximation.

Table 1. Maximum Swelling Ratio ρ_{max} and Power Law Exponent n Estimated for Different Cellulose Films

sample[a]	no. of layers	dry thickness (before regeneration) d_{TMSC} (Å)	dry thickness (after regeneration) d_0 (Å)	ρ_{max}	n
LB-1	6	45	24	1.6	20
LB-2	10	106	56	1.4	21
LB-3	20	188	104	1.7	19
SP-1		196	73	1.6	14
SP-2		488	181	1.5	15

[a] LB stands for a Langmuir−Blodgett film, while SP stands for a spin-coated film.

Ellipsometric Imaging of Microstructured Cellulose Films. Three-dimensional profiles of the microstructured cellulose films were obtained by a self-built imaging ellipsometer, as previously reported by Albersdörfer et al.[37] Light from a He−Ne laser (λ = 632.8 nm) is reflected by the sample under an incident angle of 45° and collected with a microscope objective (numerical aperture NA = 0.4; magnification, ×20). To determine the degree of polarization, the reflected beam passes through a rotatable polarizer, and a tube lens projects the image onto a cooled CCD camera (C4880, Hamamatsu, Germany). Images taken at different angles of polarization enable one to calculate the ellipsometric parameters, Ψ and Δ, for each pixel, leading to a three-dimensional (3D) reconstruction (local thickness profile) of the microstructures.

Results and Discussion

Hydration under Equilibrium. As given in Table 1, the initial film thickness values (24−104 Å) are proportional to the number of monolayers (6−20 monolayers), suggesting the monolayer thickness of $d_{mono} = 4.0-5.5$ Å. In fact, this value is in reasonable agreement with the monolayer thickness extrapolated from much thicker films (20−120 monolayers) by X-ray reflectometry, $d_{mono} = 4.2$ Å.[15,16] Homogeneity of the regenerated cellulose film was checked preliminarily by atomic force microscopy (AFM, noncontact mode), yielding a root-mean-square (rms) roughness of about 6 Å. In this study, noncontact mode AFM was used to characterize surface topography of the dry films in air but was not applied for the hydrated films. The surface roughness was found to be almost independent from the number of monolayers. This is in good agreement with the surface roughness values reported by Schaub et al. using X-ray reflectometry, $\sigma = 8$ Å.[15] Figure 3 presents changes in the equilibrium thickness of a cellulose LB film (an initial thickness of 104 Å, 20 monolayers) plotted versus relative humidity. According to the Garnet equation,[28,29] the refractive index (right coordinate) and thickness (left coordinate) of the swollen films were calculated self-consistently and plotted as a function of relative humidity.

As seen in the figure, changes in film thickness (i.e., swelling ratio $\rho = d/d_0$) were relatively small at a humidity below 80% but increased sharply at higher humidity conditions. In previous studies, similar tendencies were also observed for physisorbed films of other polysaccharides (dextran, hyaluronic acid)[31] and for grafted films of synthetic polymer brushes (poly(2-alkyl-2-oxazoline)s).[32] The thickness value at the highest humidity condition,

(26) Azzam, R. M. A.; Bashara, N. M. *Ellipsometry and Polarized Light*; North-Holland: Amsterdam, 1977.
(27) Tompkins, H. G. *User's Guide to Ellipsometry*; Academic Press: San Diego, 1993.
(28) Garnet, M. *Philos. Trans. A* **1904**, *203*, 385.
(29) Garnet, M. *Philos. Trans. A* **1906**, *205*, 237.
(30) Jellison, G. E. *J. Appl. Phys.* **1991**, *69*, 7627.
(31) Mathe, G.; Albersdörfer, A.; Neumaier, K. R.; Sackmann, E. *Langmuir* **1999**, *15*, 8726.
(32) Rehfeldt, F.; Pagnoni, L.; Jordan, R.; Tanaka, M. *Langmuir* **2002**, *18*, 4908.
(33) Landau, L. D.; Lifschitz, E. M. *Lehrbuch der theoretischen Physik, Band V, Statistische Physik*; Akademie-Verlag: Berlin, 1987.
(34) Pashley, R. M.; Kitchener, J. A. *J. Colloid Interface Sci.* **1979**, *71*, 491.
(35) Rand, R. P. *Annu. Rev. Biophys. Bioeng.* **1981**, *10*, 277.
(36) Rand, R. P.; Parsegian, V. A. *Biochem. Biophys. Acta* **1989**, 351.
(37) Albersdörfer, A.; Elender, G.; Mathe, G.; Neumaier, K. R.; Paduschek, P.; Sackmann, E. *Appl. Phys. Lett.* **1998**, *72*, 2930.

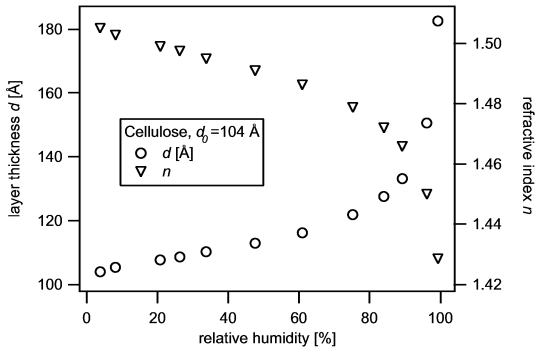

Figure 3. Static swelling curve of a cellulose LB film with initial dry thickness $d_0 = 104$ Å. The left coordinate corresponds to the absolute layer thickness d (circles), while the right coordinate corresponds to the corrected refractive index (triangles).

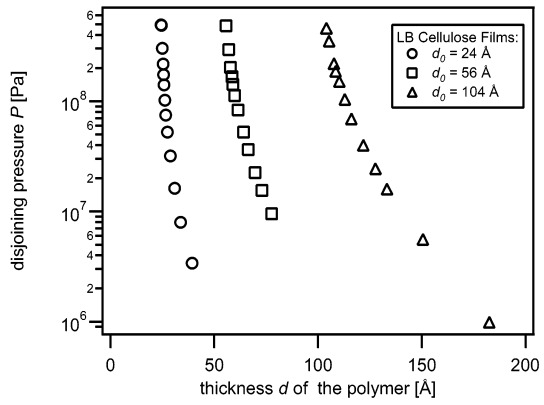

Figure 4. Force−distance relationship of different cellulose LB films under equilibrium. The disjoining pressure is plotted versus the absolute thickness of the film with different initial dry thicknesses d_0.

$d_{max} = 182$ Å, yielded the maximum swelling ratio, $\rho_{max} = d_{max}/d_0 = 1.7$. Repeated measurement cycles between low and high humidity conditions exhibited reproducible data within our experimental accuracy without any hysteresis, confirming that (a) each data point was taken under thermodynamic equilibrium and (b) there was no condensation of bulk water. In fact, our previous study on the grafted brushes of poly(2-alkyl-2-oxazoline)s suggested the presence of condensed water upon a reduction in relative humidity from 98% to 4%.[32] However, such "hydration hysteresis" could not be observed for the measured samples.

By plotting disjoining pressure (calculated from eq 1) versus the absolute film thickness d, quantitative force−distance relationships could be obtained (Figure 4). To compare hydration properties of the films with different initial thicknesses, absolute (measured) film thickness values were normalized by initial dry thickness d_0, replacing film thickness d to swelling ratio ρ (Figure 5). The maximum swelling ratio ρ_{max} showed relatively small deviations between 1.4 and 1.7 with an average value of $\rho_{max} = 1.6$ (Table 1). Variations in ρ_{max} arise from the hygrometer near the condensation limit as well as from the significant changes in the film thickness at high humidity (>90%). The normalized force−distance curves are almost congruent both in logarithmic (top) and semilogarithmic (bottom) plots, which strongly suggests

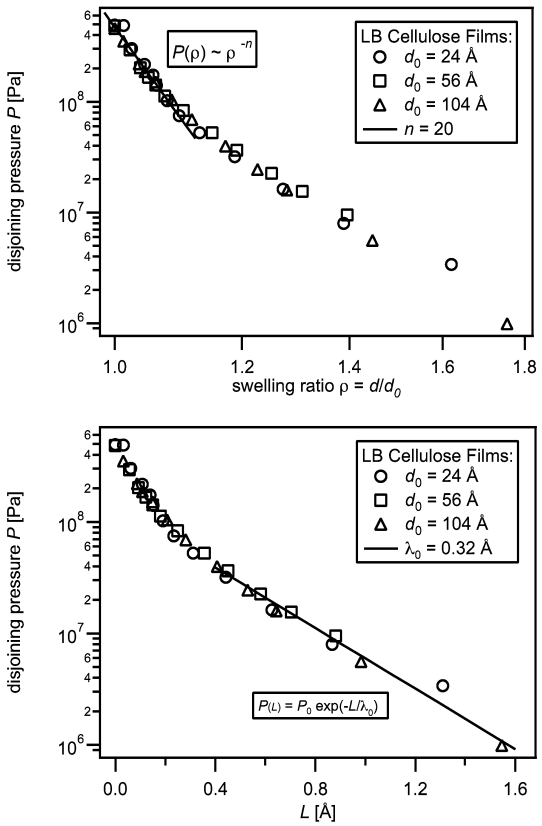

Figure 5. Hydration of cellulose LB films under equilibrium. (Top) Disjoining pressure P plotted versus the swelling ratio ρ in a logarithmic scale. The high-pressure regime ($P > 5 \times 10^7$ Pa) can be fitted with a power law, yielding an exponent $n = 20$. (Bottom) The same results plotted in a semilogarithmic scale. From the low-pressure regime ($P < 5 \times 10^7$ Pa), one can calculate an exponential decay length, $\lambda_0 = 0.32$ Å.

that the hydration properties of cellulose LB films are independent from the initial dry thickness, namely, the number of cellulose layers. This can be attributed to the layered architecture of cellulose LB films, whose polymer backbones are even oriented parallel to the dipping direction.[15] Indeed, the scenario here is suggested to be different from that of end-grafted polymer brushes, where we observed a strong influence of polymer chain length on hydration properties.[32]

In the high disjoining pressure regime (>5×10^7 Pa), the force−distance curves can be fitted with a power law

$$P(\rho) \sim \rho^{-n} \tag{2}$$

Under these conditions, the film is strongly compressed so that a very large exponent ($n = 20$) was obtained (Figure 5, top). Such a strong repulsion can be approximated with a theta function reflecting the infinite jump of the energy for a hard-core potential[3] that originates from the incompressibility of the polymer chains.

In the lower disjoining pressure regime, polymer films exhibit a different swelling behavior (Figure 5, bottom). In fact, an abrupt shift from a power-law-like dependence to an exponential decay could be observed at around $P = 5 \times 10^7$ Pa. According to a significant water uptake at high humidity, hydration force becomes dominant in the

lower pressure regime. Here, a new parameter L, the distance between two neighboring monosaccharides, is introduced. In a cubic lattice model, L can be represented as

$$L(\rho) = a_0(\rho^{1/3} - 1) \quad (3)$$

where a_0 is the size of a monosaccharide, $a_0 = 7.5$ Å.[38] Rau and Parsegian[39] reported that the interaction at a small intermolecular distance is dominated by an exponentially decaying hydration force according to

$$P = P_0 \exp(-L/\lambda_0) \quad (4)$$

λ_0 stands for a decay length, while P_0 stands for an intrinsic pressure generated by the hydration forces. When eq 4 was applied to the lower disjoining pressure regime of the force−distance curve (Figure 5, bottom), we obtained $\lambda_0 = 0.32$ Å and $P_0 = 1.4 \times 10^8$ Pa.

Hydration of spin-coated cellulose films under equilibrium was also studied in the same manner as described above. Thickness of the resulting film was found to be almost proportional to TMSC concentration. Homogeneity of the regenerated film was also checked preliminarily by AFM, yielding a relatively larger rms value (30 Å) in comparison to that of LB films. In comparison to the LB films, regeneration of the spin-coated films resulted in more pronounced reduction in the film thickness by a factor of approximately 2.7 (Table 1). Figure 6 presents normalized force−distance relationships of spin-coated cellulose films with initial thicknesses of 73 and 181 Å. For all the measured samples, we observed no hysteresis during several swelling cycles, suggesting there was no condensation of bulk water. As shown in the figure, the normalized force−distance curves are almost congruent in both logarithmic (top) and semilogarithmic (bottom) plots, which strongly suggests that the hydration properties of spin-coated cellulose films are independent from the initial dry thickness. Actually, the maximum swelling ratio ρ_{max} was almost identical ($\rho_{max} = 1.5-1.6$). Similar tendencies were also reported for physisorbed polysaccharide films with a random chain conformation, claiming that ρ_{max} was rather characteristic for each polysaccharide.[31] Interestingly, the ρ_{max} values of spin-coated cellulose films were almost identical to those obtained for LB films (Table 1). In contrast to the highly ordered, anisotropic orientation of cellulose backbones in LB films, cellulose backbones in spin-coated films are more isotropic and, therefore, less ordered.[15] However, the analysis of the regime dominated by hydration forces (Figure 6, bottom) yielded the same decay length ($\lambda_0 = 0.32$ Å) and similar intrinsic pressure ($P_0 = 1.9 \times 10^8$ Pa). Although the intermonomer distance L should be slightly different from that of a cubic lattice, these results clearly denoted the similar hydration properties of LB films and spin-coated films, almost independent from the initial film thickness (Table 2).

Previously, several studies have been conducted to measure hydration forces within various polysaccharide films. Rau and Parsegian reported quantitative measurements of forces between stiff and hydrophilic biopolymers at controlled osmotic pressures.[39,40] Interaxial distances within bulk films and pellets (thickness of 0.5−1 mm) of xanthan, schizophyllan, and hydroxypropylcellulose were determined by X-ray scattering in the presence of non-

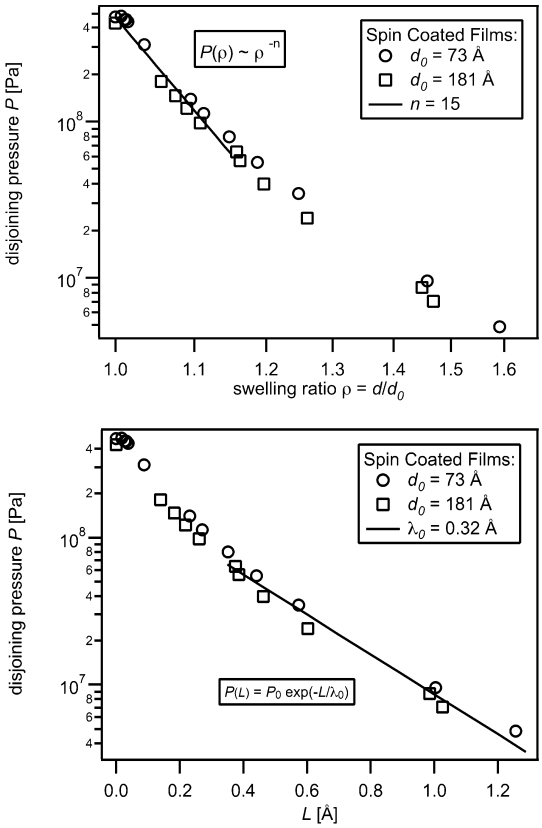

Figure 6. Hydration of spin-coated cellulose films under equilibrium. (Top) Disjoining pressure P plotted versus the swelling ratio ρ in a logarithmic scale. The high-pressure regime ($P > 5 \times 10^7$ Pa) can be fitted with a power law, yielding an exponent $n = 15$. (Bottom) The same results plotted in a semilogarithmic scale. From the low-pressure regime ($P < 5 \times 10^7$ Pa), one can calculate an exponential decay length, $\lambda_0 = 0.32$ Å.

Table 2. Hydration Parameters Calculated from Equation 4

sample	λ_0 [Å]	P_0 [Pa]	sample	λ_0 [Å]	P_0 [Pa]
LB-1	0.30	1.4×10^8	SP-1	0.32	2.1×10^8
LB-2	0.32	1.4×10^8	SP-2	0.32	1.8×10^8
LB-3	0.32	1.3×10^8			

miscible polymer solutions, such as poly(ethylene glycol), with various concentrations. Hydration forces were measured in the separation range between 13 and 33 Å, yielding decay distance values of $\lambda_0 = 2.9-3.3$ Å (xanthan), 3.4 Å (schizophyllan), and 3−4 Å (hydroxypropylcellulose). However, in contrast to their approach to explain two different regimes with a double-exponential function,[40] our experimental results in the high disjoining pressure regime obviously could not be fitted with exponential decays but rather followed a power law. Using almost the same ellipsometry setup, Mathe et al. measured force−distance relations for physisorbed films of hyaluronic acid (linear, anionic polysaccharide) and dextran (branched polysaccharide without net charges). As a clear difference from the cellulose films studied here, the maximum swelling ratios of these two polysaccharides were significantly larger, $\rho_{max} = 6.0$ (hyaluronic acid) and $\rho_{max} = 3.4$ (dextran), suggesting that they possess larger water uptake abilities than cellulose. The measured force−

(38) Aspinall, G. *The Polysaccharides*; Academic Press: New York, 1982.
(39) Rau, D. C.; Parsegian, V. A. *Science* **1990**, *249*, 1278.
(40) Bonnet-Gonnet, C.; Leikin, S.; Chi, S.; Rau, D. C.; Parsegian, V. A. *J. Phys. Chem. B* **2001**, *105*, 1877.

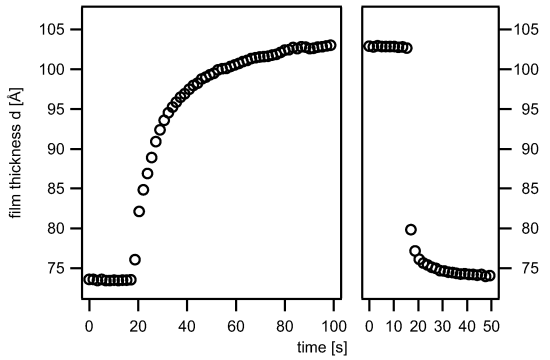

Figure 7. Dynamic swelling curve of a spin-coated cellulose film (d_0 = 73 Å). At t = 17 s, the atmospheric humidity was abruptly switched between the humidity of 4% and 94%, yielding the characteristic time constants of τ = 14 s (swelling) and τ = 4 s (draining).

distance curves in the high-pressure regime were fitted by a power law, yielding rather small exponents both for hyaluronic acid and dextran, n = 9−9.5. As such strong repulsion in this pressure regime can be related to the incompressibility of polymer chains, it is plausible that the smaller exponents of dextran and hyaluronic acid coincide with their higher compressibility due to the less ordered, more flexible polymer chains. Hydration forces in the low-pressure regime were analyzed by assuming the same monosaccharide size, a_0 = 7.5 Å. Remarkably, the calculated values of decay length (λ_0 = 2.0 Å for hyaluronic acid and λ_0 = 1.1 Å for dextran) were much larger than that of cellulose (λ_0 = 0.32 Å), corresponding to their higher water uptake abilities (i.e., larger ρ_{max} values). Since both cellulose and dextran are based on the same monosaccharide unit (glucose), such significant differences in hydration due to different conformational degrees of freedom seem to be correlated to their different native functions.

Hydration under Osmotic Shocks. An abrupt change in atmospheric humidity was applied to study dynamic (i.e., nonequilibrium) hydration of cellulose films. Monitoring of fast water uptake of hygroscopic polymers is difficult when the finite time required to exchange the atmosphere becomes competitive to (or longer than) that of the hydration kinetics. In fact, our preliminary measurements showed that the dynamic swelling of cellulose films was faster than the characteristic time constant for switching humidity, $\tau \sim 35$ s.[32] Using the setups described in the Experimental Section, we can switch the local humidity conditions in proximity of the measurement point with a characteristic time of 1 s. Figure 7 represents the hydration kinetics of a spin-coated cellulose film with an initial dry thickness of 73 Å. Prior to the measurement, the film was equilibrated under a relative humidity of 4%. At t = 17 s, the atmosphere was switched to a high humidity (94%), leading to a fast increase in film thickness (Figure 7, left). The characteristic time constant τ was defined as the time that is required for the film to reach the thickness $d = (1 - e^{-1})d_{max}$.[32] The time constant calculated from the dynamic swelling was τ = 14 s. After the film reached equilibrium with the humid atmosphere, relative humidity was switched back to 4%. Previously, Mathe et al. studied the characteristic swelling kinetics for hyaluronic acid and dextran using a slightly modified setup: τ = 1 s for hyaluronic acid and τ = 3 s for dextran.[31] As the time constants of the studied systems were comparable to or even smaller than the standard measurement interval (1.7 s), they monitored merely changes in the intensity of reflected light with a CCD camera at a fixed angle polarization and simulated the thickness. On the contrary, we used the conventional setup for accuracy of the thickness measurement, because the hydration kinetics of cellulose (τ = 14 s) could be followed. A logarithmic presentation of the measured data points suggested that dynamic hydration might involve two different kinetic processes, and therefore, more detailed analyses are further demanded. As seen in the figure, the exclusion of water from the swollen film, that is, "draining" of the film, was found to be faster than water uptake, yielding a smaller time constant of τ = 4 s. Kinetic time constants measured for LB films were identical to those for spin-coated films. In comparison to the faster swelling kinetics observed for other polysaccharides with less ordered, more flexible backbones, the "stretched" hydration kinetics of cellulose can be attributed to the fewer conformational degrees of freedom of "rigid" cellulose backbones and to the strong intermolecular hydrogen bridges to stabilize their supramolecular architectures under various conditions.

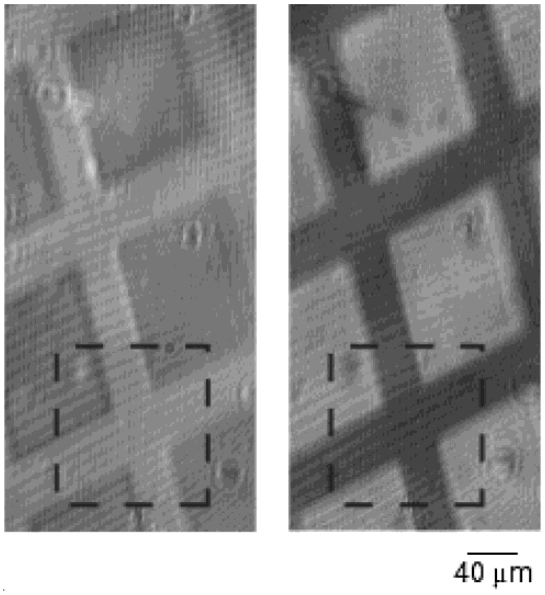

Figure 8. Δ (left) and Ψ (right) images of the spin-coated cellulose film (d_0 = 183 Å) taken by an imaging ellipsometer. The scale bar corresponds to 40 μm. 3D profiles of the highlighted region were reconstructed in Figure 9.

Imaging of Microstructured Films. Microstructures of cellulose substrates were processed rather simply through deep UV photolithography. In the case of LB films, illumination with deep UV light (λ < 220 nm) is necessary to cleave alkylsiloxane monolayers as well as cellulose backbones, recovering the original silica surface.[24] To avoid thermal decomposition of the films, fused silica was placed between the lamp and the sample as a heat absorber. Figure 8 presents Δ (left) and Ψ (right) images of the spin-coated cellulose film (d_0 = 183 Å), where an EM grid was used as a photomask (grid width, 42 μm; spacing, 80 μm). Although interference fringes from the optics could be seen, the patterns were sharply contrasted in both images. Three-dimensional profiles of the highlighted region were reconstructed from the calculated local film thickness (for each CCD pixel) by the self-developed fitting

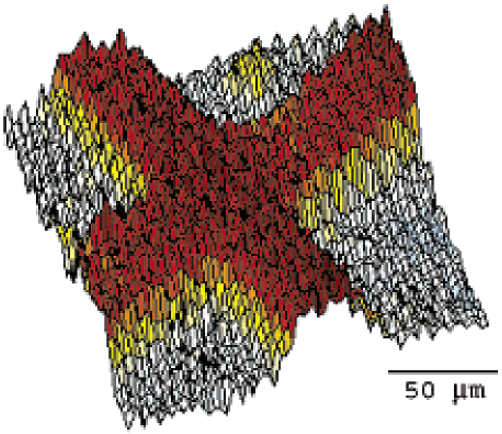

Figure 9. 3D profiles of the structured cellulose film ($d_0 = 183$ Å) with a top-to-bottom height difference of about 18 nm.

routine,[37] verifying the sharp edges of the microstructured cellulose film (Figure 9).

Recently, we accomplished orientation selective immobilization of native cell membranes (human erythrocytes) on cellulose LB films,[19] where selective fluorescence labeling demonstrated that the immobilized erythrocyte membranes selectively inverted their native, asymmetric orientation. On the other hand, no adsorption or rupture of cells could be seen when they were incubated with bare glass slides or quartz substrates. Since the surface of the microstructured film presented in Figure 8 and Figure 9 consists of (a) bare silica (thermally oxidized silicon) and (b) an ultrathin ($d \sim 18$ nm) cellulose layer, it includes a large potential to fabricate microdomains based on immobilized native cell membranes without losing their asymmetric orientation and functions (Figure 10). Actually, the microstructures remained stable even against intensive rinsing with water and storage in ambient conditions for more than 6 months. In contrast to the direct "stamping" of isolated artificial lipid bilayers and proteins onto solid supports,[41,42] such a strategy will further enable one to create biocompatible micropatterns (templates) to accumulate native cell membranes.

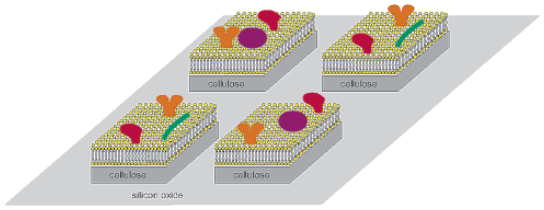

Figure 10. Schematic presentation of native cell membranes confined on microstructured cellulose surfaces.

Acknowledgment. The authors are indebted to Professor E. Sackmann for the constant support and instructive comments and thankful to Wacker Siltronic for donation of silicon wafers. M.T. is grateful to Professor G. Wegner (Max Planck Institute for Polymer Research) for his helpful advice in the synthesis of cellulose derivatives. F.R. thanks Drs. G. Mathe and K. Neumeier for helpful suggestions and A. Muschielok for experimental assistance. This work was supported by the Deutsche Forschungsgemeinschaft (Ta 259/2) and by the Fonds der Chemischen Industrie. M.T. is a recipient of the Emmy Noether Fellowship of DFG.

LA0261702

(41) Groves, J. T.; Boxer, S. G. *Acc. Chem. Res.* **2002**, *35*, 149.
(42) Kam, L.; Boxer, S. G. *J. Biomed. Mater. Res.* **2001**, *55*, 487.

A.3 Native Cell Membranes on Patterned Polymer Support

The immobilization of native cell membranes on planar support is becoming of increasing more interest. Tanaka et al. demonstrated the selective wetting of solid substrates with different coatings with native cell membranes [19]. The cells used in their study were adult human erythrocyte ghost cells (ery ghosts) prepared by washing, lysing, and resealing native erythrocytes. It could be shown that these ery ghosts formed a homogeneous layer on cellulose but not on the bare glass surface or on poly-L-lysine, where only strongly adhered patches were found. This work was continued with micro-structured ultrathin cellulose films on glass slides where the selective wetting of the substrate with erythrocyte ghost cells was demonstrated [21].

M. Tanaka, A.P. Wong, F. Rehfeldt, M. Tutus and S. Kaufmann: "Selective deposition of native cell membranes on biocompatible micropatterns", *J. Am. Chem. Soc.* **126** (2004), p. 3257-3260.

J|A|C|S
ARTICLES
Published on Web 02/24/2004

Selective Deposition of Native Cell Membranes on Biocompatible Micropatterns

Motomu Tanaka,* Amy P. Wong, Florian Rehfeldt, Murat Tutus, and Stefan Kaufmann

Contribution from the Lehrstuhl für Biophysik E22, Technische Universität München, James-Franck-Strasse 1, D-85748 Garching, Germany

Received October 10, 2003; E-mail: mtanaka@ph.tum.de

Abstract: We establish two methods to deposit native biomembranes (human erythrocyte membranes and sarcoplasmic reticulum membranes) selectively onto biocompatible microtemplates. The first method utilizes UV photolithography to micropattern the regenerated cellulose, while the second uses the "stamping" of protein barriers onto homogeneous cellulose supports. The relatively simple methods established here allow for the position selective spreading of three-dimensional native cells into two-dimensional films, retaining the orientation and lateral density of transmembrane proteins in their native state.

Introduction

Supported lipid membranes have been intensively and widely studied in the last couple of decades as a general model system of cell- and tissue surfaces.[1−3] Several methods have been developed for micropatterning solid supported membranes to manipulate and characterize each corral individually.[4−7] For example, the membrane patterns can be used as quasi two-dimensional fluid matrixes (instead of bulk three-dimensional matrixes such as gels) that allow for the accumulation and reorganization of functional molecules by electrophoresis.[8,9] The use of micropipettors will enable the parallel monitoring of interactions between the partitioned membranes and the analytes (antibodies, drugs, etc.) by spotting different analytes onto individual corrals. Moreover, the partitioning of membranes prohibits the diffusion of proteins across the separating barriers and, therefore, includes a large potential for complementary coupling of supported membranes and semiconductor devices[10−13] by matching of the lateral dimensions.

Incorporation of transmembrane (integral) proteins into the membrane introduces biospecific functions, which enables one to physically model cell adhesion.[14−17] One method is to reconstitute transmembrane proteins into artificial phospholipid vesicles (proteoliposomes) and to deposit them on solid surfaces; however, a fundamental drawback of this method is that control of the orientation and density of the proteins in vesicles is difficult. One of the most straightforward ways to overcome this issue is to use native cells as natural proteoliposomes. As generally known, the orientation of transmembrane proteins in cell membranes is stringently regulated by nature.[18] Along this line, several studies have been conducted to immobilize native cells (erythrocyte, HeLa cells, etc.) on several types of colloidal particles (Latex, silica, etc.).[19−21] Previously, we reported the spreading of native cell membranes (erythrocytes) onto planar solid substrate coated homogeneously with cellulose films.[22] Since no adhesion or rupturing of cells could be observed on bare glass substrates, the results suggested the potential for "printing" arrays of native cell membranes. Here we demonstrate direct spreading of native cells on biocompatible microtemplates, which has never been reported. In the following, two simple methods are described to process microtemplates of regenerated cellulose for local immobilization of native biomembranes on planar supports without losing membrane asymmetry.

Materials and Methods

Erythrocyte ghosts were prepared from freshly drawn blood as reported by Schwoch and Passow.[23] Orientation of the erythrocyte membrane was identified with two immune-fluorescence labels: (1)

(1) Tamm, L. K.; McConnell, H. M. *Biophys. J.* **1985**, *47*, 105−113.
(2) Sackmann, E. *Science* **1996**, *271*, 43−48.
(3) Sackmann, E.; Tanaka, M. *Trends Biotechnol.* **2000**, *18*, 58−64.
(4) Groves, J. T.; Ulman, N.; Boxer, S. G. *Science* **1997**, *275*, 651−653.
(5) Kung, L. A.; Groves, J. T.; Ulman, N.; Boxer, S. G. *Adv. Mater.* **2000**, *12*, 731−734.
(6) Morigaki, K.; Baumgart, T.; Offenhausser, A.; Knoll, W. *Angew Chem., Int. Ed.* **2001**, *40*, 172−174.
(7) Groves, J. T.; Boxer, S. G. *Acc. Chem. Res.* **2002**, *35*, 149−157.
(8) Stelzle, M.; Mielich, R.; Sackmann, E. *Biophys. J.* **1992**, *63*, 1346−1354.
(9) Groves, J. T.; Wulfing, C.; Boxer, S. G. *Biophys. J.* **1998**, *71*, 2716−2723.
(10) Hillebrandt, H.; Wiegand, G.; Tanaka, M.; Sackmann, E. *Langmuir* **1999**, *15*, 8451−8459.
(11) Purrucker, O.; Hillebrandt, H.; Adlkofer, K.; Tanaka, M. *Electrochim. Acta* **2001**, *47*, 791.
(12) Hillebrandt, H.; Tanaka, M.; Sackmann, E. *J. Phys. Chem. B* **2002**, *106*, 477−488.
(13) Steinhoff, G.; Purrucker, O.; Tanaka, M.; Stutzmann, M.; Eickhoff, M. *Adv. Funct. Mater.* **2003**, *13*, 841−846.
(14) Brian, A. A.; McConnell, H. M. *Proc. Natl. Acad. Sci. U.S.A.* **1984**, *81*, 6159−6163.
(15) Chan, P.; Lawrence, M. B.; Dustin, M. L.; Ferguson, L. M.; Golan, D. E.; Springer, T. A. *J. Cell Biol.* **1991**, *10*, 245−255.
(16) Qi, S. Y.; Groves, J. T.; Chakraborty, A. K. *Proc. Natl. Acad. Sci. U.S.A.* **2001**, *98*, 6548−6553.
(17) Goennenwein, S.; Tanaka, M.; Hu, B.; Moroder, L.; Sackmann, E. *Biophys. J.* **2003**, *85*, 846−855.
(18) Rothman, J. E.; Lenard, J. *Science* **1977**, *195*, 743−753.
(19) Jacobson, B. S.; Branton, D. *Science* **1976**, *195*, 302−304.
(20) Cohen, C. M.; Kalish, D. I.; Jacobson, B. S.; Branton, D. *J. Cell Biol.* **1977**, *75*, 119−134.
(21) Kaufmann, S.; Tanaka, M. *ChemPhysChem* **2003**, *4*, 699−704.
(22) Tanaka, M.; Kaufmann, S.; Nissen, J.; Hochrein, M. *Phys. Chem. Chem. Phys.* **2001**, *3*, 4091−4095.
(23) Schwoch, G.; Passow, H. *Mol. Cell. Biochem.* **1973**, *2*, 197−217.

10.1021/ja038981d CCC: $27.50

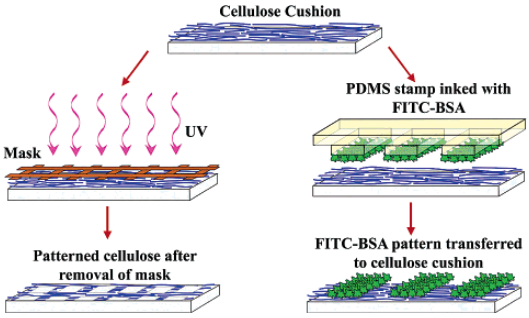

Figure 1. Preparation of cellulose microtemplates. The first method (a) uses deep UV photolithography to micropattern the cellulose, while the second (b) utilizes the "stamping" of protein barriers onto polymer supports.

the extracellular part of glycophorin could be labeled with a first monoclonal antibody (mouse IgG) and a second polyclonal antibody (goat anti-mouse IgG) with tetramethylrhodamine isothiocyanate (TRITC, outside label), while (2) the cytoplasmic domain of Band 3 could be recognized with a first monoclonal antibody (mouse IgG) and a second TRITC-labeled polyclonal goat anti-mouse IgG antibody (inside label). To gain the maximum immunofluorescence signals, the concentration, incubation time, and pretreatment with bovine serum albumin (BSA) were carefully optimized.[22] In brief: The first monoclonal antibody for the inside label was diluted 2500 times (by volume), while the one for the outside label was diluted 500 times. For both labelings, the second polyclonal antibody was diluted 150 times. The incubation time for each antibody labeling was about 30 min. Nonspecific adsorption of antibodies was avoided by treating the sample with a solution of bovine serum albumin (BSA, 30 mg/mL) for 1 h before the immunolabeling. Prior to the spreading upon cellulose microtemplates, we confirmed that intact erythrocyte ghosts retained their native orientation throughout the preparation, exhibiting fluorescence signals only from antibodies to the extracellular domain of glycophorin.

Ultrathin films of cellulose (thickness ~5 nm) were prepared by Langmuir−Blodgett deposition of synthetic trimethylsilyl cellulose (TMSC) onto hydrophobized glass substrates, followed by regeneration with HCl vapor.[10,22,24] Preparation of cellulose microtemplates was represented in Figure 1. The first method (a) used deep UV photolithography to micropattern the cellulose,[24] while the second (b) utilized the "stamping" of homogeneous protein barriers onto polymer supports.[25−27] Ni electron microscope grids (SCI Science Services, Munich, Germany, feature size: 40 μm, spacing between the grids: 60 μm) were used as photomasks. An EM grid was fixed onto the cellulose surface with a drop of chloroform, and the sample was illuminated for 30 min with a 500 W mercury arc lamp, using a thermal filter of fused silica (thickness: 6 mm, Melles Griot, Bensheim, Germany). The illumination with deep UV light (emmision lines at λ = 244, 194, and 185 nm) led to the ablation of cellulose backbones and alkylsilanes,[24,28] resulting in a hydrophilic glass surface. A poly(dimethysiloxane) (PDMS) stamp was formed by curing the two-part elastomer, Sylgard 184 (Dow Corning, Midland, MI), upon patterned photoresist at 70 °C for 1 h.[26] The photoresist was spun to a thickness of approximately 1.5 μm onto hexadimethyldisilazane (HMDS)-primed silicon wafers (3 × 3 cm^2) and was patterned with standard photolithographic techniques. These masters were used indefinitely. PDMS was cured on the masters and plasma-cleaned for 50 s to render the surface hydrophilic.

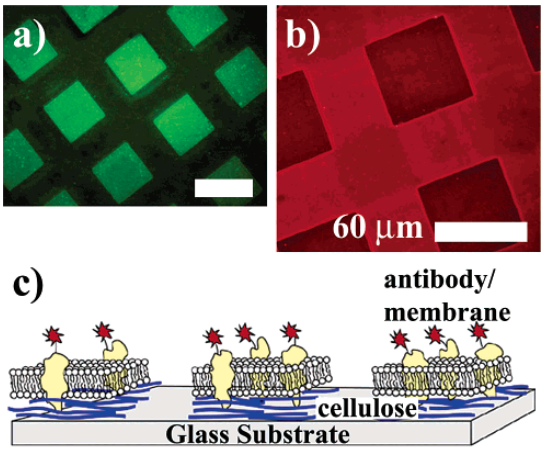

Figure 2. (a) Fluorescence image of cellulose micropatterns exposed to a solution of bovine serum albumin labeled with fluorescein isothiocyanate (FITC-BSA) after removing the photomask. FITC-BSA adsorbs only onto the ablated area (bare glass substrate). (b) Human erythrocyte membranes spread on cellulose microtemplates (without BSA treatment). After incubation, the cytoplasmic domain of Band 3 is identified with a monoclonal and a TRITC-labeled polyclonal antibody (inside label). (c) Orientation of the erythrocyte membrane after spreading. Erythrocyte ghosts selectively adhere and rupture only on the cellulose micropatterns, exposing their cytoplasmic side.

Results and Discussion

Figure 2a shows the fluorescence image of cellulose micropatterns exposed for 10 min to a solution of BSA (1 mg/mL) labeled with fluorescein isothiocyanate (FITC) after removing the photomask. FITC-BSA adsorbs onto the ablated area (i.e., bare glass substrate). Human erythrocyte ghosts are then incubated with the cellulose micropatterns at 37 °C for 2 h. After several washes to remove any unbound intact erythrocytes, the inside labels are applied (Figure 2b). A homogeneous fluorescence signal from the TRITC-labeled antibody confirms that the immobilized erythrocyte membrane exposes the cytoplasmic domain uniformly (Figure 2c). Here, the treatment with FITC-BSA is inserted only to visualize the patterns before incubation with the cells, but it does not influence the resulting patterns of erythrocyte membranes. It should be noted that the fluorescence signals in this image are from labeled transmembrane proteins and not from lipids. Outside labeling reveals no fluorescence signal up to our detection limit (data not shown), suggesting that all the adherent cells ruptured and inverted their orientation to "inside-out". Here, the treatment of the cellulose patterns with BSA solution has no influence on the selective spreading of cell membranes; the spreading of erythrocyte membranes took place only on the cellulose film but not on the glass surface.

Figure 3a shows the fluorescence image of "stamped" FITC-BSA patterns in an aqueous buffer. A poly(dimethysiloxane) (PDMS) stamp (feature size: 5 μm, spacing between the grids: 25 μm) is inked with a 1 mg/mL solution of FITC-BSA for 10 min and then placed upon a cellulose film for 10 min under a 30 g weight. Some bleeding of the BSA grids during stamping leads to a slightly larger transferred feature size, but the resulting

(24) Rehfeldt, F.; Tanaka, M. *Langmuir* **2003**, *19*, 1467−1473.
(25) Kung, L. A.; Kam, L.; Hovis, J. S.; Boxer, S. G. *Langmuir* **2000**, *16*, 6773−6776.
(26) Kam, L.; Boxer, S. G. *J. Biomed. Mater. Res.* **2001**, *55*, 487−495.
(27) Sapuri, A. R.; Baksh, M. M.; Groves, J. T. *Langmuir* **2003**, *19*, 1606−1610.
(28) Mooney, J. F.; Hunt, A. J.; McIntosh, J. R.; Liberko, C. A.; Walba, D. M.; Rogers, C. T. *Proc. Natl. Acad. Sci. U.S.A.* **1996**, *93*, 12287−12291.

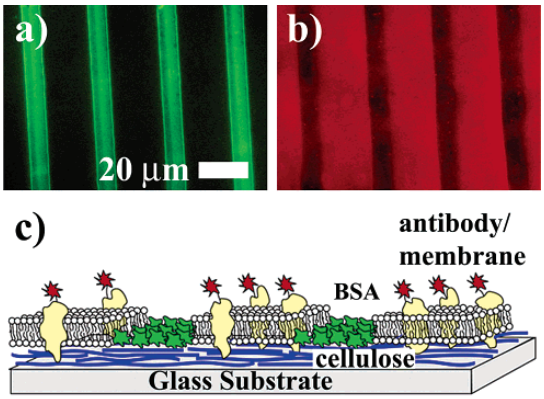

Figure 3. (a) Fluorescence image of "stamped" FITC-BSA patterns using a PDMS stamp. (b) Incubation of erythrocyte ghosts to the same microtemplates and subsequent inside labeling yield homogeneous fluorescence signals from areas with cellulose films. (c) "Inside out" orientation of erythrocyte membranes after deposition onto cellulose with FITC-BSA patterns. The protein patterns are stable after spreading and labeling.

micropatterns of FITC-BSA are stable for several days under water without any degradation. Incubation of erythrocyte ghosts to the microtemplates and subsequent inside labeling yields homogeneous fluorescence signals from areas with the cellulose cushion, but no fluorescence signal can be detected from areas with FITC-BSA. The fluorescence image with the FITC filter set is identical to that in Figure 3a, confirming that the protein barriers remain stable after treatment with cells and antibodies. Outside labeling of this system also exhibits no fluorescence signals, which verifies that spreading of cell membranes also results in an inside-out orientation (Figure 3c).

Immobilized erythrocyte membranes can cover macroscopically large surfaces homogeneously for both types of microtemplates. Immune-fluorescence labeling of transmembrane proteins exhibits no boundaries between the ruptured membrane patches, suggesting that the immobilized cell membranes fuse with each other and "wet" the surface continuously. Since the height deviation (~5 nm) is much smaller than the width of each pattern ($\geq 5\,\mu$m), the surface heterogeneity can be treated almost as a columnar one. Therefore, the spreading of cell membranes can be understood as an analogue of "complete wetting", characterized by a positive disjoining pressure and a positive spreading coefficient S:

$$S = \sigma_{SL} - \sigma_{SM} - \sigma_{ML}$$

where σ_{SL}, σ_{SM}, and σ_{ML} correspond to the tensions at substrate/liquid, substrate/membrane, and membrane/liquid interfaces, respectively. For example, strong electrostatic attractions between strong polycations and weak polyanions (glycocalix with sialic acid residues) destabilize the membrane and result in the formation of regions of tight local contact (de-wetting).[22] Cell membranes therefore prefer cellulose surfaces over bare glass and BSA-coated substrates to achieve a positive disjoining pressure and a positive spreading coefficient.

In addition to erythrocyte ghosts, sarcoplasmic reticulum (SR) vesicles are spread onto the similar cellulose micropatterns. SR vesicles, microsomes extracted from rabbit muscle as reported by de Meis and Hasselbach,[29] are purchased from Nimbus Biotechnologie GmbH (Leipzig, Germany). SR vesicles store

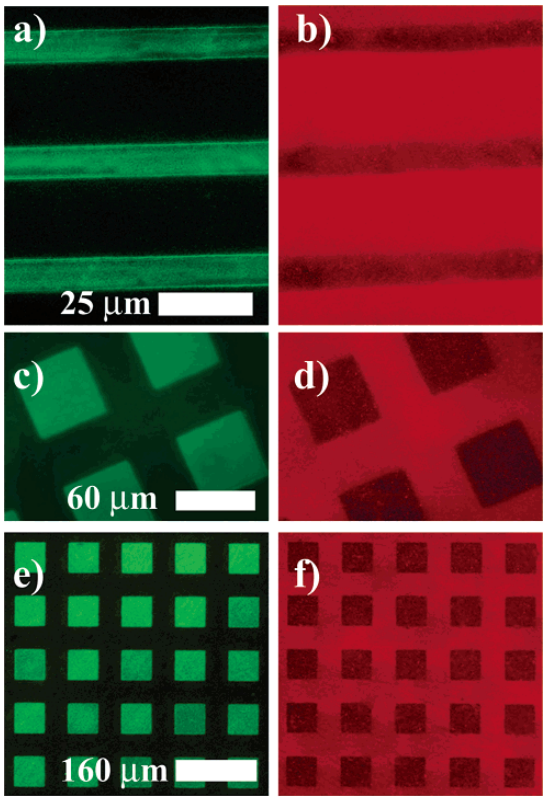

Figure 4. (a) Fluorescence images of the cellulose film with "stamped" FITC-BSA patterns. (b) After spreading of SR vesicles, the cytoplasmic head of Ca^{2+}-ATPase is labeled with a monoclonal and a TRITC-labeled polyclonal antibody. The protein patterns are stable after spreading and labeling. (c) Fluorescence images of the photostructured cellulose film treated with FITC-BSA solution. (d) Selective spreading of SR membranes onto cellulose micropatterns. The adsorbed FITC-BSA effectively prevents the spreading of SR membranes onto the bare glass substrate. (e and f) Fluorescence images of the same micropatterns taken with a lower magnification, demonstrating the uniform confinement of SR membranes over a macroscopically large area.

calcium ions in muscle fibers and contain two calcium ion transporters: the ryanodine receptor and Ca^{2+}-ATPase. The SR vesicles are disrupted through the preparation, and therefore, the membrane orientation cannot be controlled. After the vesicles are incubated with cellulose micropatterns at 37 °C for 2 h, the cytoplasmic head of Ca^{2+}-ATPase in the immobilized SR membrane is labeled with a first monoclonal mouse IgG antibody and a second TRITC-labeled polyclonal goat anti-mouse IgG antibody. When SR vesicles are incubated with the cellulose film with "stamped" FITC-BSA patterns (Figure 1b) and labeled with antibodies, we also observe clear patterns of TRITC-labeled Ca^{2+}-ATPase within the isolated grids (Figure 4, parts a and b). Parts d and f of Figure 4 show the TRITC-labeled SR membranes on a photostructured cellulose film (Figure 1a), which had been pretreated with 1 mg/mL of FITC-BSA solution before spreading membranes (Figure 4, parts c and e). In these series of experiments, treatment of the photolithgraphically patterned cellulose (Figure 1a) with FITC-BSA prior to incubation with the SR vesicles is necessary, since

(29) de Meis, L.; Hasselbach, W. *J. Biol. Chem.* **1971**, *246*, 4759−4763.

preliminary experiments showed that SR membranes readily spread not only upon cellulose films but also on other surfaces such as bare glass slides, poly(lysine), etc. (data not shown). This can be attributed to the fact that SR vesicles resemble artificial proteoliposomes more than native cells, because the extracted SR membranes are free of glycocalix and cytoskeleton and consist only of lipids and proteins. Similar to what is observed for erythrocyte ghosts, SR vesicles selectively spread on the prepatterned cellulose film, where Ca^{2+}-ATPase is homogeneously distributed. Fluorescence images taken at lower magnification (Figure 4, parts e and f) clearly demonstrate the uniform confinement of immobilized membranes over a macroscopically large area.

Fluorescence recovery after photobleaching (FRAP) experiments suggest no clear sign of protein diffusion in both of the native membranes,[30] which can be attributed to the following: (1) In intact erythrocyte membranes, Band 3 proteins are bound to the cytoskeleton (spectrin) via ankyrin. The cytoskeleton which remains after erythrocyte rupture as suggested by previous reports[19,21] acts as a net, preventing protein diffusion across spectrin network. The mesh size, which is less than 1 μm,[31] is smaller than the diameter of the bleached spot ($\sim$9 μm), and thus, diffusion is not observed. (2) Direct immune-fluorescence labeling of the proteins provides sufficient drag to protein diffusion. Two IgG antibodies (first monoclonal and second polyclonal) are used to label each protein. The total molecular weight of two IgGs is up to 300 kD, which is larger than that of the protein (about 50 kD for Band 3 and 110 kD for Ca^{2+}-ATPase). The diffusion of such "bulky" antibody complexes can significantly be impeded by the steric hindrance from the neighboring proteins (antibody complexes) and cytoskeletons. Thus, quantitative measurements of protein mole fractions and the use of smaller marker molecules will be necessary to gain further insight of the diffusion of proteins in the planar, native cell membranes.

(30) FRAP measurements were carried out by focusing a beam of an argon ion laser (Innova 70, Coherent, Santa Clara, CA) onto the sample (spot diameter 9.3 μm) through a microscope oil immersion objective (Fluar 100×, n.a. 1.3, Carl Zeiss, Göttingen, Germany). The dye molecules were bleached by a short laser pulse (200 ms), and recovery of the fluorescence intensity according to the diffusion of unbleached dyes was monitored by a photomultiplier (Hamamatsu Photonics, Herrsching, Germany). The lateral diffusion constant D and mobile fraction were calculated from the measured fluorescence recovery profiles, yielding the sensitivity limit of about $D = 0.01\ \mu m^2\ s^{-1}$. However, even the measurement in a long period (40 min) suggests no clear sign of protein diffusion out of the drift of the background signals.

(31) Byers, T. J.; Branton, D. *Proc. Natl. Acad. Sci. U.S.A.* **1985**, *82*, 6153−6157.

Conclusions

In this article, position and orientation selective spreading of native cell membranes (human erythrocyte membranes) on solid substrates has been demonstrated by the use of biocompatible microtemplates of regenerated cellulose films. In contrast to the previously reported techniques for the micropatterning of artificial lipid bilayers on bare solid substrates, the relatively simple microstructuring of biocompatible ultrathin films enables three-dimensional native cells to be transformed into two-dimensional films within confined geometry. Since the orientation and lateral density of proteins can be kept as in their native state, quantitative evaluation of the proteins' function on solid substrates is possible. These microtemplates can be further applied to immobilize microsomes from rabbit muscles (SR vesicles). Both types of membrane micropatterns retain their structure for more than a week, verifying their thermodynamic and mechanical stability. Thus, the processing methods established here allow for further manipulation by the addition of other native cell membranes to design heterobiofunctional surfaces to study the function of membrane proteins under more native environments.

Acknowledgment. We thank E. Sackmann and S. Boxer for inspiring discussions and K. Fütterer for experimental assistance. A.P.W. is thankful to J. Groves, A. R. Sapuri, and J. Hovis for helpful suggestions. This work was supported by the Deutsche Forschungs Gemeinschaft (Emmy Noether Program Ta259/1, SFB563) and the Fonds der Chemischen Industrie.

JA038981D

A.4 Lipids

The chemical structures of the used lipid and fluorescence dye tracers are presented in Figure A.6.

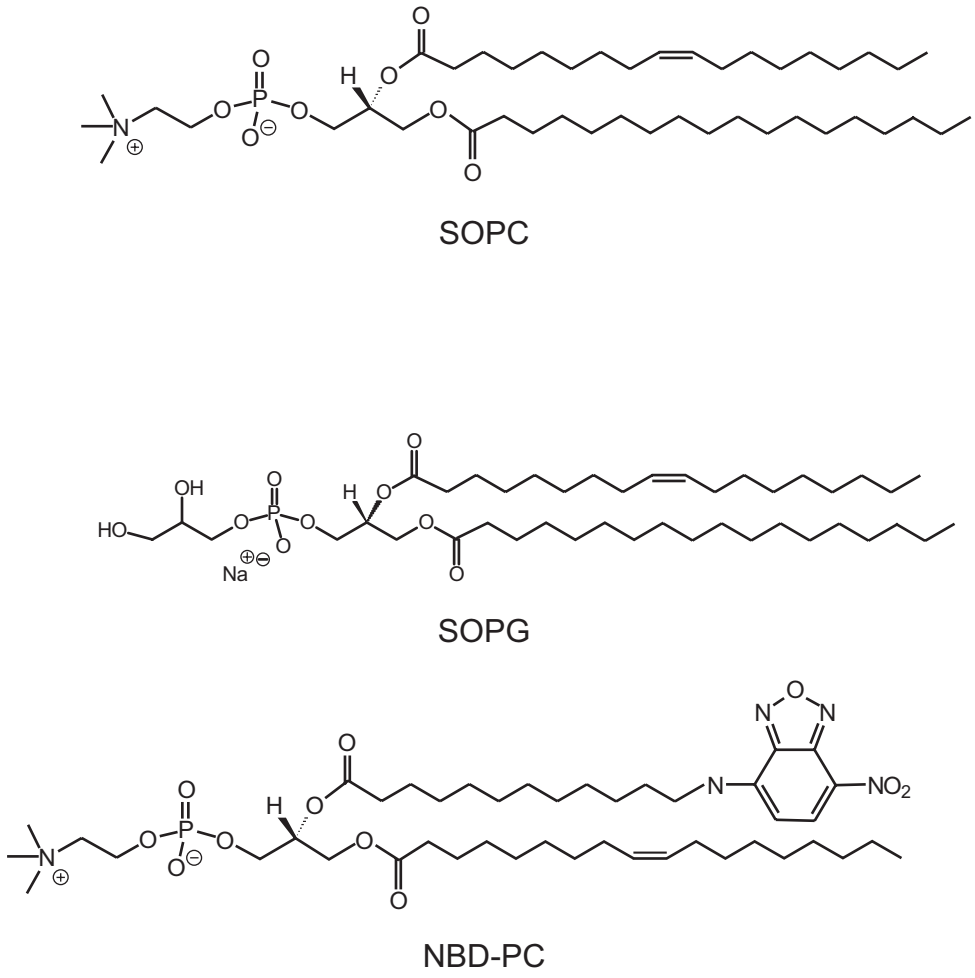

Figure A.6: Chemical structures of the used lipids (SOPC, SOPG) and the fluorescence dye tracer (NBD-PC).

A.5 X-Ray Reflectivity Script

Here, the script used to measure the x-ray reflectivity at the diffractometer at the HMI (Berlin, Germany) is presented.

Run	θ_{min}	θ_{max}	steps	time [s]	$\Delta\theta$	t_{run} [min]	t_{total} [h]
1	0.1	0.3	21	5	0.01	2	0.03
2	0.3	0.7	41	10	0.01	7	0.14
3	0.7	1.5	41	100	0.02	68	1.28
4	1.5	3.1	41	200	0.04	137	3.56
5	3.1	4.1	21	200	0.05	70	4.73

Table A.1: X-ray reflectivity script

A.6 Neutron Reflectivity Scripts

The following scripts were used at V6 (HMI, Berlin, Germany) to measure the specular neutron reflectivity. Script 1 was used for the measurement of the silicon block against air and script 2 and 3 were used for the flow cell measurements.

Run	θ_{min}	θ_{max}	steps	slits	time [s]	$\Delta\theta$	t_{run} [min]	t_{total} [h]
1	0.1	0.4	31	0.5 0.5	15	0.01	20	0.34
2	0.4	0.7	11	0.5 0.5	60	0.03	15	0.59
3	0.7	1.1	11	0.5 0.5	240	0.04	48	1.40
4	1.1	1.6	11	1.0 1.0	300	0.05	59	2.39
5	1.6	2.5	19	1.0 1.0	600	0.05	198	5.68
6	2.6	3.05	7	1.0 1.0	600	0.075	73	6.90

Table A.2: Script 1

Run	θ_{min}	θ_{max}	steps	slits	time [s]	$\Delta\theta$	t_{run} [min]	t_{total} [h]
1	0.1	0.4	31	0.5 0.5	30	0.01	28	0.47
2	0.4	0.7	11	0.5 0.5	200	0.03	41	1.15
3	0.7	1.1	11	0.5 0.5	400	0.04	78	2.45
4	1.1	1.6	11	1.0 1.0	400	0.05	78	3.74
5	1.6	2.5	19	1.0 1.0	600	0.05	198	7.03
6	2.5	3.1	9	1.0 1.0	900	0.075	139	9.34

Table A.3: Script 2

Run	θ_{min}	θ_{max}	steps	slits	time [s]	$\Delta\theta$	t_{run} [min]	t_{total} [h]
1	0.1	0.4	31	0.5 0.5	30	0.01	25	0.41
2	0.4	0.7	11	0.5 0.5	200	0.03	40	1.08
3	0.7	1.1	11	0.5 0.5	400	0.04	77	2.36
4	1.1	1.6	11	1.0 1.0	400	0.05	77	3.63
5	1.6	2.5	19	1.0 1.0	600	0.05	196	6.90
6	2.5	3.1	9	1.0 1.0	900	0.075	138	9.19

Table A.4: Script 3

A.7 Abbreviations

(v/v)	volume per volume
d.i.	degree of ionization
DMAEMA	(dimethylamino)ethyl methacrylate
Gent	gentiobiose lipid
Lac 1	lactose 1 lipid
LB	Langmuir-Blodgett
LS	Langmuir-Schaefer
MMA	methyl methacrylate
NBD	7-nitro-2-1,3-benzoxadiazol-4-yl
NR	neutron reflectometry
ODTMS	octadecyl trimethoxy silane
PCSA	polarizer-compensator-sample-analyzer
rA	rotating analyzer
r.m.s.	root mean square
SANS	small angle neutron scattering
SAXS	small angle x-ray scattering
SOPC	1-stearoyl-2-oleoyl-*sn*-glycero-3-phosphocholine
SOPG	1-stearoyl-2-oleoyl-*sn*-gycero-3-[phospho-rac-(1-glycerol)]
TMSC	trimethyl silyl cellulose
VdW	van der Waals
WAXS	wide angle x-ray scattering
XR	x-ray
XRR	x-ray reflectometry

A.8 Symbols

Δ	ellipsometric angle delta
Ψ	ellipsometric angle psi
X	relative humidity
A_{tot}	total area
A_{mol}	area per molecule
π	lateral pressure
T	temperature
N	monomer number
$\mathbf{n}$	complex refractive index
n	refractive index
k	extinction coefficient
i	imaginary unit
π	lateral pressure
R	reflectivity
R_f	Fresnel reflectivty
R_p, R_s	parallel and perpendicular Fresnel reflectivty

Bibliography

[1] B.V. Derjaguin and N.V. Churaev. *Surface Forces*. Consultants Bureau, New York, 1987.

[2] J. N. Israelachvili. *Intermolecular and Surface Forces with Applications to Colloidal and Biological Systems*. Academic Press Inc., London, 1985.

[3] W.D. Comper. *Extracellular Matrix*. Harwood Academic Publishers, Amsterdam, 1996.

[4] H.J. Gabius and S. Gabius. *Glycoscience*. Chapmann & Hall, Weinheim, 1997.

[5] E. Sackmann. Supported membranes: Scientific and practical applications. *Science*, 271(5245):43–48, 1996.

[6] E. Sackmann and M. Tanaka. Supported membranes on soft polymer cushions: Fabrication, characterization and applications. *Trends Biotechnol.*, 18(2):58–64, 2000.

[7] M. Tanaka, F. Rehfeldt, M. F. Schneider, G. Mathe, A. Albersdörfer, K.R. Neumaier, O. Purrucker, and E. Sackmann. Wetting and dewetting of extracellular matrix and glycocalix models. *Journal of Physics D: Condensed Matter*, 16:1–14, 2004.

[8] R. Bruinsma and E. Sackmann. Bioadhesion and the dewetting transition. *Comptes Rendus De L Academie Des Sciences Serie Iv Physique Astrophysique*, 2(6):803–815, 2001.

[9] G. I. Bell, M. Dembo, and P. Bongrand. Cell-adhesion - competition between nonspecific repulsion and specific bonding. *Biophysical Journal*, 45(6):1051–1064, 1984.

[10] P. Fromherz, A. Offenhausser, T. Vetter, and J. Weis. A neuron-silicon junction - a retzius cell of the leech on an insulated-gate field-effect transistor. *Science*, 252(5010):1290–1293, 1991.

[11] P. Fromherz. Electrical interfacing of nerve cells and semiconductor chips. *Chem. Phys. Chem.*, 3(3):276–284, 2002.

[12] S. Gönnenwein, M. Tanaka, B. Hu, L. Moroder, and E. Sackmann. Functional incorporation of integrins into solid supported membranes on ultrathin films of cellulose: Impact on adhesion. *Biophysical Journal*, 85:846–855, 2003.

[13] O. Purrucker, A. Förtig, R. Jordan, and M. Tanaka. Supported membranes with well-defined polymer tethers - incorporation of cell receptors. *Chemical Physics and Physical Chemistry*, 5:327–335, 2004.

[14] S. Löfas and B. Johnson. A novel hydrogel matrix on gold surfaces in surface plasmon resonance sensors for fast and efficient covalent immobilization of ligands. *J. Chem. Soc., Chem. Commun.*, 21:1526–1528, 1990.

[15] J.M. Harris. *Poly(ethyleneglycol) Chemistry.* Plenum Press, New York, 1992.

[16] G. Elender, M. Khner, and E. Sackmann. Functionalisation of Si/SiO2 and glass surfaces with ultrathin dextran films and deposition of lipid bilayers. *Biosensors & Bioelectronics*, 11(6-7):565–577, 1996.

[17] G. Decher. Fuzzy nanoassemblies: Toward layered polymeric multicomposites. *Science*, 277(5330):1232–1237, 1997.

[18] H. Möhwald. From Langmuir monolayers to nanocapsules. *Colloids Surf. A*, 171(1-3):25–31, 2000.

[19] M. Tanaka, S. Kaufmann, J. Nissen, and M. Hochrein. Orientation selective immobilization of human erythrocyte membranes on ultrathin cellulose films. *Physical Chemistry Chemical Physics*, 3(18):4091–4095, 2001.

[20] H. Hillebrandt, G. Wiegand, M. Tanaka, and E. Sackmann. High electric resistance polymer/lipid composite films on indium-tin-oxide electrodes. *Langmuir*, 15(24):8451–8459, 1999.

[21] M. Tanaka, A. P. Wong, F. Rehfeldt, M. Tutus, and S. Kaufmann. Selective deposition of native cell membranes on biocompatible micropatterns. *Journal of the American Chemical Society*, 126(10):3257–3260, 2004.

[22] F. Rehfeldt and M. Tanaka. Hydration forces in ultrathin films of cellulose. *Langmuir*, 19(5):1467–1473, 2003.

[23] S. W. An, R. K. Thomas, F. L. Baines, N. C. Billingham, S. P. Armes, and J. Penfold. Neutron reflectivity of adsorbed water-soluble block copolymers at the air/water interface: The effects of composition and molecular weight. *Macromolecules*, 31(22):7877–7885, 1998.

[24] S. W. An, R. K. Thomas, F. L. Baines, N. C. Billingham, S. P. Armes, and J. Penfold. Neutron reflectivity of an adsorbed water-soluble block copolymer at the air/water interface: The effects of pH and ionic strength. *Journal of Physical Chemistry B*, 102(26):5120–5126, 1998.

[25] S. W. An, T. J. Su, R. K. Thomas, F. L. Baines, N. C. Billingham, S. P. Armes, and J. Penfold. Neutron reflectivity of an adsorbed water-soluble block copolymer: A surface transition to micelle-like aggregates at the air/water interface. *Journal of Physical Chemistry B*, 102(2):387–393, 1998.

[26] S. W. An, P. N. Thirtle, R. K. Thomas, F. L. Baines, N. C. Billingham, S. P. Armes, and J. Penfold. Structure of a diblock copolymer adsorbed at the hydrophobic solid/aqueous interface: Effects of charge density on a weak polyelectrolyte brush. *Macromolecules*, 32(8):2731–2738, 1999.

[27] P. F. Green, T. M. Christensen, and T. P. Russell. Ordering at diblock copolymer surfaces. *Macromolecules*, 24(1):252–255, 1991.

[28] D.A. Tomalia and G.R. Killat. *Encyclopedia of Polymer Science and Engineering*. Wiley, New York, 1985.

[29] F. L. Baines, N. C. Billingham, and S. P. Armes. Synthesis and solution properties of water-soluble hydrophilic-hydrophobic block copolymers. *Macromolecules*, 29(10):3416–3420, 1996.

[30] S. W. An and R. K. Thomas. Determination of surface pK(a) by the combination of neutron reflection and surface tension measurements. *Langmuir*, 13(26):6881–6883, 1997.

[31] W. Kern and Puotinen. Cleaning solutions based on hydrogen peroxide for use in silicon semiconductor technology. *RCA Rev.*, 31:187–206, 1970.

[32] W. Kern. Radiochemical study of semiconductor surface contamination: II. deposition of trace impurities on silicon and silica. *RCA Review*, 31:235–164, 1970.

[33] J.F. Mooney, A.J. Hunt, J.R. McIntosh, C.A. Liberko, D.M. Walba, and C.T. Rogers. Patterning of functional antibodies and other proteins by photolithography of silane monolayers. *Proc. Natl. Acad. Sci. USA*, 93:12287–12291, 1996.

[34] M. Tutus and M. Tanaka. *submitted*, 2004.

[35] G. L. Gaines. *Insoluble Monolayers at Liquid-Gas Interfaces*. Wiley - Interscience, New York, 1966.

[36] I. Langmuir and V.J. Schaefer. *J. Am. Chem. Soc.*, 60:1351, 1938.

[37] M. Keller, J. Schilling, and E. Sackmann. Oscillatory magnetic bead rheometer for complex fluid microrheometry. *Review in Scientific Instruments*, 72:3626–3634, 2001.

[38] J. Schilling. *Entwicklung einer schnellen digitalen Bildverarbeitungstechnik und einer interferometrischen 2λ - Mikroskopietechnik: Anwendung in der Zell-Biophysik*. PhD Thesis, Technische Universität München, Germany, 2004.

[39] S. K. Satija, C. F. Majkrzak, T. P. Russell, S. K. Sinha, E. B. Sirota, and G. J. Hughes. Neutron reflectivity study of block copolymers adsorbed from solution. *Macromolecules*, 23(16):3860–3864, 1990.

[40] F. Mezei, R. Golub, F. Klose, and H. Toews. Focused beam reflectometer for solid and liquid surfaces. *Physica B*, 213:898–900, 1995.

[41] Rothen, A. Ellipsometric studies of thin films. *Prog. Surf. Membr. Sci.*, 8:81–118, 1974.

[42] Drude, P. *Ann. Phys. Chem.*, 36:865, 1889.

[43] R.M.A. Azzam and N.M. Bashara. *Ellipsometry and polarized light.* North-Holland Personal Library, Amsterdam, 1977.

[44] T.P. Russell. X-ray and neutron refletivity for the investigation of polymers. *Mat. Sci. Rep.*, 5:171–271, 1990.

[45] Gibaud A. (Eds.) Daillant J. *Lecture Notes in Physics.* X-Ray and Neutron Reflectivity: Principles and Application. Springer-Verlag, Heidelberg, 1999.

[46] R. K. Thomas. Neutron reflection from liquid interfaces. *Annual Review of Physical Chemistry*, 55:391–426, 2004.

[47] G. Porod. Die Röntgenkleinwinkelstreuung von dichtgepackten kolloiden Systemen. *Kolloid-Zeitschrift and Zeitschrift für Polymere*, 124(2):83–114, 1951.

[48] S. K. Sinha, E. B. Sirota, S. Garoff, and H. B. Stanley. X-ray and neutron-scattering from rough surfaces. *Physical Review B*, 38(4):2297–2311, 1988.

[49] L. G. Parratt. Surface studies of solids by total reflection of x-rays. *Physical Review*, 95(2):359–369, 1954.

[50] R.P. Rand and V.A. Parsegian. Hydration forces between phospholipid bilayers. *Biochem. Biophys. Acta*, (988):351–376, 1989.

[51] V.A. Parsegian, N. Fuller, and R.P. Rand. Measured work of deformation and repulsion of lecithin bilayers. *Proc. Natl. Acad. Sci. USA*, 76(6):2750–2754, 1979.

[52] A.W. Adamson and A.P. Gast. *Physical Chemistry of Surfaces.* Wiley-Interscience, New York, 1997.

[53] G. Gouy. *J. Phys.*, 9(4):457, 1910.

[54] D.L. Chapman. *Phil. Mag.*, 25(6):475, 1913.

[55] P. Debye and E. Hückel. *Phys. Z.*, 24:185, 1923.

[56] T. Young. *Micellaneous Works*, volume 1, page 418. Murray, 1855.

[57] E. Sackmann and R. F. Bruinsma. Cell adhesion as wetting transition? *Chemical Physics and Physical Chemistry*, 3(3):262–269, 2002.

[58] L. Leger and J. F. Joanny. Liquid spreading. *Reports on Progress in Physics*, 55(4):431–486, 1992.

[59] F. Brochard-Wyart and P. G. de Gennes. Dynamics of partial wetting. *Advances in Colloid and Interface Science*, 39:1–11, 1992.

[60] R. R. Netz and D. Andelman. Neutral and charged polymers at interfaces. *Physics Reports-Review Section of Physics Letters*, 380(1-2):1–95, 2003.

[61] G.J. Fleer, M.A. Cohen Stuart, J.M.H.M. Scheutjens, Cosgrove T., and B. Vincent. *Polymers at Interfaces*. Chapman & Hall, London, 1993.

[62] W. Kuhn. *Kolloid Z.*, 68:2, 1934.

[63] P.J. Flory. *Principles of Polymer Chemistry*. Cornell Univ. Press, Ithaca NY, 1953.

[64] P.J. Flory. *Statistical Mechanics of Chain Molecules*. Interscience, New York, 1969.

[65] M. Huggins. *J. Am. Chem. Soc.*, 64:1712, 1942.

[66] P.G. de Gennes. *Scaling concepts in polymer physics*. Cornell Univ. Press, Ithaca, NY, 1979.

[67] P. G. de Gennes. Conformations of polymers attached to an interface. *Macromolecules*, 13:1069–1075, 1980.

[68] P. G. de Gennes. Polymers at an interface; a simplified view. *Advances in Colloid and Interface Science*, 27:189–209, 1987.

[69] Th. Odijk and M. Mandel. *Physica*, 93A:298, 1978.

[70] G.S. Manning. *J. Chem. Phys.*, 51:924, 1969.

[71] H. Ahrens, S. Forster, and C. A. Helm. Charged polymer brushes: Counterion incorporation and scaling relations. *Physical Review Letters*, 81(19):4172–4175, 1998.

[72] P. Pincus. Colloid stabilization with grafted polyelectrolytes. *Macromolecules*, 24(10):2912–2919, 1991.

[73] J. R. Silvius. *'Thermotropic Phase Transitions of Pure Lipids in Model Membranes and their Modification by Membrane Proteins' in 'Lipid-Protein Interactions'*, volume 2, pages 239–281. Wiley - Interscience, New York, 1982.

[74] G. Cevc and D. Marsh. *Phospholipid Bilayers - Physical Principles and Models*. Wiley - Interscience, New York, 1987.

[75] G. Cevc. *Phospholipid Handbook*. Marcel Dekker Inc., New York, 1993.

[76] T. M. Bayerl, R. K. Thomas, J. Penfold, A. Rennie, and E. Sackmann. Specular reflection of neutrons at phospholipid monolayers - changes of monolayer structure and headgroup hydration at the transition from the expanded to the condensed phase state. *Biophysical Journal*, 57(5):1095–1098, 1990.

[77] T. Charitat, E. Bellet-Amalric, G. Fragneto, and F. Graner. Adsorbed and free lipid bilayers at the solid-liquid interface. *European Physical Journal B*, 8(4):583–593, 1999.

[78] C. H. Li, D. Constantin, and T. Salditt. Biomimetic membranes of lipid-peptide model systems prepared on solid support. *Journal of Physics-Condensed Matter*, 16(26):S2439–S2453, 2004.

[79] G. Fragneto, F. Graner, T. Charitat, P. Dubos, and E. Bellet-Amalric. Interaction of the third helix of antennapedia homeodomain with a deposited phospholipid bilayer: A neutron reflectivity structural study. *Langmuir*, 16(10):4581–4588, 2000.

[80] G. Fragneto-Cusani. Neutron reflectivity at the solid/liquid interface: examples of applications in biophysics. *Journal of Physics-Condensed Matter*, 13(21):4973–4989, 2001.

[81] J. Penfold. Neutron reflectivity and soft condensed matter. *Current Opinion in Colloid & Interface Science*, 7(1-2):139–147, 2002.

[82] T. Salditt, C. Munster, U. Mennicke, C. Ollinger, and G. Fragneto. Thermal fluctuations of oriented lipid membranes by nonspecular neutron reflectometry. *Langmuir*, 19(19):7703–7711, 2003.

[83] G. Fragneto, T. Charitat, F. Graner, K. Mecke, L. Perino-Gallice, and E. Bellet-Amalric. A fluid floating bilayer. *Europhysics Letters*, 53(1):100–106, 2001.

[84] R. Dalgliesh. Application of off-specular scattering of x-rays and neutrons to the study of soft matter. *Current Opinion in Colloid & Interface Science*, 7(3-4):244–248, 2002.

[85] B. Keimer, E. Sackmann, and P. J. Withers. Neutron scattering - the case for neutron sources. *Science*, 298(5593):543–543, 2002.

[86] R. Kampmann, V. Deriglazov, M. Haese-Seiller, M. Marmotti, M. Tristl, and E. Sackmann. REFSANS: a novel reflectometer for analyses of liquid and soft surfaces at the new research reactor FRM-II in Munich, Germany. *Physica B*, 276:212–213, 2000.

[87] R. Kampmann, M. Haese-Seiller, M. Marmotti, J. Burmester, V. Deriglazov, V. Syromiatnikov, A. Okorokov, F. Frisius, M. Tristl, and E. Sackmann. The novel reflectometer REFSANS for analyses of liquid and soft surfaces at the new research reactor FRM-II in Munich, Germany. *Applied Physics A - Materials Science & Processing*, 74:S249–S251, 2002.

[88] M. Tanaka, S. Schiefer, C. Gege, R. R. Schmidt, and G. G. Fuller. Influence of subphase conditions on interfacial viscoelastic properties of synthetic lipids with gentiobiose head groups. *Journal of Physical Chemistry B*, 108(10):3211–3214, 2004.

[89] M. F. Schneider, G. Mathe, M. Tanaka, C. Gege, and R. R. Schmidt. Thermodynamic properties and swelling behavior of glycolipid monolayers at interfaces. *Journal of Physical Chemistry B*, 105(22):5178–5185, 2001.

[90] M. F. Schneider, R. Zantl, C. Gege, R. R. Schmidt, M. Rappolt, and M. Tanaka. Hydrophilic/hydrophobic balance determines morphology of glycolipids with oligolactose headgroups. *Biophysical Journal*, 84(1):306–313, 2003.

Publications

F. Rehfeldt, R. Steitz, S.P. Armes, A.P. Gast and M. Tanaka, "Chemical Switching of Diblock Copolymer Monolayers at the Interface (1): Control of Lateral Chain Density and Conformation", *Macromolecules*, submitted.

F. Rehfeldt, R. Steitz, S.P. Armes, A.P. Gast, R. v. Klitzing and M. Tanaka, "Chemical Switching of Diblock Copolymer Monolayers at the Interface (2): Membrane Interactions at the Solid/Liquid Interface", *Macromolecules*, submitted.

M. Tanaka, F. Rehfeldt, M.F. Schneider, C.G. Gege, R.R. Schmidt and S.S. Funari, "Oligomer to polymer transition in short ethylene glycol chains connected to mobile hydrophobic anchors", *ChemPhysChem*, in print.

M. Tanaka, F. Rehfeldt, M. F. Schneider, G. Mathe, A. Albersdörfer, K.R. Neumaier, O. Purrucker, and E. Sackmann, "Wetting and dewetting of extracellular matrix and glycocalix models", *Journal of Physics: Condensed Matter*, accepted

J.E. Wong, F. Rehfeldt, P. Hänni, M. Tanaka, R.v. Klitzing "Swelling Behavior of Polyelectrolyte Multilayers in Saturated Water Vapor", *Macromolecules* **37** (2004), 7285 –7289.

M. Tanaka, A.P. Wong, F. Rehfeldt, M. Tutus and S. Kaufmann "Selective deposition of native cell membranes on biocompatible micropatterns", *J. Am. Chem. Soc.* **126** (2004), 3257–3260.

F. Rehfeldt and M. Tanaka, "Hydration forces in ultrathin films of cellulose", *Langmuir* **19** (2003), 1467–1473.

F. Rehfeldt, L. Pagnoni, R. Jordan, and M. Tanaka, "Static and dynamic swelling of grafted poly (2-alkyl-2-oxazoline)s", *Langmuir* **18** (2002), 4908–4914.

Vielen Dank...

... an alle, die zum Gelingen dieser Arbeit beigetragen haben. Ganz besonders möchte ich mich bedanken bei

Prof. Dr. Erich Sackmann, der immer ein offenes Ohr für physikalische Fragen und jederzeit brillante Ideen hatte und hervorragende Denkanstöße gab. **Motomu Tanaka**, der durch seine besondere Begeisterung für wissenschaftliche Fragen immer verstand, diese auf mich und andere zu bertragen, zu jeder Tages und Nachtzeit eine offene Tür hatte und viele gute und durchführbare Ideen lieferte. **Prof. Alice Gast**, für die Gastfreundschaft in Stanford und die interessanten wissenschaftlichen Diskussionen. **Michael Nikolaides und Oliver Purrucker**, mit denen ich zusammen vom ersten Semester durch das Studium bis zur Promotion gelangte und ohne die diese Zeit sicher nicht so erfolgreich und vergnüglich gewesen wäre. **Roman Zantl, Valentin Kahl, Ulf Rädler und dem Rest von ibidi**, für die besonders gute wissenschaftliche und außerwissenschaftliche Zusammenarbeit. **Murat Tutus, Matthias F. Schneider, Heiko Hillebrandt, Klaus Adlkofer, Kirstin Seidel, Daniel Gassul, Rafael Oliveira, Fatima Al-Ali, Andrea Pascu und Thomas Schubert** dafür, daß sie die Motomu Gruppe zu einem liebenswerten Haufen machten, der sowohl bei der Arbeit, als auch bei der Freizeitgestaltung allezeit hilfreich war. Bei **Christian Daniel** für die gemeinsame Zeit beim Messen und im Neutronenkindergarten in Oxford. Bei meinen lieben Werkstudenten **Emanuel Schneck, Heike Schirmer und Adam Muschielok**, die mir mit viel Engagement beim Experimentieren und Präparieren halfen. Bei **Bruno Demé, Sergio Funari und Roland Steitz**, die ihre Beamlines perfekt beherrschten und beim Messen sowie Interpretieren der Daten sehr behilflich waren. **Rudi Lehrhuber** für die mechanische Feinstarbeit. Natürlich bei allen anderen **E22'ern**, insbesondere bei allen Kaffeeecklern und den ehemaligen sowie gegenwärtigen Insassen des Diplomandenzimmers. Sowie allen Freunden (Kaffeetscherl, SC-Worldwide) die mich unterstützten sowie die für die notwendige Ablenkung von der Physik sorgten.

Der letzte und ganz besondere Dank gilt **Andrea, ihrer und meiner Familie**.